

Save Kristiansen

# Dissolution Rate and Wettability of $\text{SiO}_2\text{-CaO-Al}_2\text{O}_3$ Slags on Quartz

Master's thesis in Chemical Engineering and Biotechnology

Supervisor: Merete Tangstad

Co-supervisor: Marit Buhaug Folstad

June 2023



Save Kristiansen

# **Dissolution Rate and Wettability of SiO<sub>2</sub>-CaO-Al<sub>2</sub>O<sub>3</sub> Slags on Quartz**

Master's thesis in Chemical Engineering and Biotechnology  
Supervisor: Merete Tangstad  
Co-supervisor: Marit Buhaug Folstad  
June 2023

Norwegian University of Science and Technology  
Faculty of Natural Sciences  
Department of Materials Science and Engineering





# Preface

This thesis investigates the dissolution rate and wetting properties of  $\text{SiO}_2\text{--CaO--Al}_2\text{O}_3$  slags on industrial quartz in silicon and ferrosilicon production. The master's thesis is an evaluation of the course TMT4900 - Materials Chemistry and Energy Technology at the Norwegian University of Technology and Science (NTNU).

I would like to thank my supervisor, Merete Tangstad, for allowing me to investigate this topic and for all the invaluable theoretical insights shared during our office meetings. Secondly, I would like to express my gratitude to my co-supervisor, Marit Buhaug Folstad, who has consistently provided valuable insights and ideas for my project. Their contributions have been instrumental in helping me overcome the challenges associated with this topic, and I greatly appreciate their support and guidance.

Additionally, I would like to thank Ingrid Hansen at SINTEF for her valuable knowledge of the sessile drop furnace and her helping hand during training. Lastly, I am grateful for the assistance and guidance from Morten Peder Raanes at NTNU when analyzing my samples with EPMA.

Trondheim, June 2023

Save Kristiansen

# Abstract

This study aims to investigate the dissolution rate and wettability of  $\text{SiO}_2\text{--CaO--Al}_2\text{O}_3$  slag on industrial quartz to understand the interactions between industrial slag and quartz during silicon and ferrosilicon production. The study is important to develop more knowledge on how to increase the mass flow of charge materials and decrease the energy consumption in industrial furnaces.

Three synthetic slags with varying chemical compositions were heated in a sessile drop furnace to  $1500\text{ }^\circ\text{C}$  and held isothermally for 0 min, 15 min and 30 min to investigate the wettability, tested with two different slag sizes of approximately 50 mg and 150 mg. The wet samples were further analyzed with an electron probe microanalyzer (EPMA) to examine their cross-sections.

The wetting experiments demonstrated favorable wetting conditions for slags with 50%  $\text{SiO}_2\text{--}21\% \text{ CaO--}29\% \text{ Al}_2\text{O}_3$  and 62 %  $\text{SiO}_2\text{--}20\% \text{ CaO--}18\% \text{ Al}_2\text{O}_3$ . In contrast, slags with 38%  $\text{SiO}_2\text{--}20\% \text{ CaO--}42\% \text{ Al}_2\text{O}_3$  did not exhibit wetting due to their solid phase. The wetting angle decreased with decreasing silica content and longer isothermal holding time. However, holding the slags for 30 min indicated similar wetting conditions for slags with 50 %  $\text{SiO}_2$  and 62 %  $\text{SiO}_2$ , meaning silicon slags experience good wetting properties on industrial quartz. No significant difference was found between 50 mg and 150 mg slags.

The slags exhibited an increase in  $\text{SiO}_2$  with longer holding time and smaller size. However, the chemical analyses indicated a trend of constant silica content in the slag bulk, meaning the slags were not diffusion-controlled. Slags were present in quartz cracks as a

result of a volume expansion in the substrate, showing an increase in SiO<sub>2</sub> further down in the cracks.

For 50 % SiO<sub>2</sub>, the rate constant was  $2.25 \cdot 10^{-4} \text{g s}^{-1}$  and  $1.21 \cdot 10^{-4} \text{g s}^{-1}$  for 50.9 mg and 149.9 mg. For 62 % SiO<sub>2</sub>, they were  $7.66 \cdot 10^{-5} \text{g s}^{-1}$  and  $3.06 \cdot 10^{-5} \text{g s}^{-1}$ . The dissolution rate of SiO<sub>2</sub> was found to be faster for 50% SiO<sub>2</sub> compared to 62% SiO<sub>2</sub>, particularly for small-sized slags. The results showed a slower reaction rate at lower temperatures compared to earlier research, suggesting the need for further investigations at higher temperatures within the operating range.

# Sammendrag

Denne studien har som mål å undersøke oppløsningshastigheten og fuktighetsgraden av  $\text{SiO}_2\text{-CaO-Al}_2\text{O}_3$ -slagge på industriell kvarts for å forstå interaksjonene mellom industrislagge og -kvarts i silisium- og ferrosilisiumproduksjon. Studien er viktig for å utvikle mer kunnskap om hvordan man kan øke massestrømmen av råmaterialer og redusere energiforbruket i industrioivner.

Tre syntetiske slagge med varierende kjemisk sammensetning ble varmet opp i en fuktningsovn til  $1500\text{ }^\circ\text{C}$  og holdt isotermisk for 0 min, 15 min og 30 min for å studere fuktningen, testet med to forskjellige slaggestørrelser på ca. 50 mg og 150 mg. Prøvene ble videre analysert med en elektronprobe-mikroanalyser (EPMA) for å undersøke tverrsnittene deres.

Fuktningseksperimentene viste gode fuktighetsforhold for slagge med 50%  $\text{SiO}_2$ -21%  $\text{CaO}$ -29%  $\text{Al}_2\text{O}_3$  og 62%  $\text{SiO}_2$ -20%  $\text{CaO}$ -18%  $\text{Al}_2\text{O}_3$ , mens slagge med 38%  $\text{SiO}_2$ -20%  $\text{CaO}$ -42%  $\text{Al}_2\text{O}_3$  opplevde ingen fuktning da slaggen var i fast fase. Fuktningvinkelen ble redusert med minkende  $\text{SiO}_2$  og lengre isotermisk holdetid. Derimot, å holde slaggen i 30 min indikerte lignende fuktighetsforhold for slagge med 50%  $\text{SiO}_2$  og 62%  $\text{SiO}_2$ , noe som tyder at silisiumslagge opplever gode fuktningsegenskaper på industriell kvarts. Det ble ikke funnet noen signifikant forskjell mellom 50 mg og 150 mg slagge.

Slaggene viste en økning i  $\text{SiO}_2$  med lengre holdetid og en mindre størrelse. De kjemiske analysene indikerte imidlertid en trend med konstant innhold av  $\text{SiO}_2$  i slaggebulken, noe som indikerer at slaggen ikke var diffusjonsbegrenset. Slagge var også tilstede i kvarts-

sprekker som følge av en volumekspansjon i substratet, som viste en økning i SiO<sub>2</sub> lenger ned i sprekkene.

For 50% SiO<sub>2</sub> var hastighetskonstanten  $2.25 \cdot 10^{-4} \text{g s}^{-1}$  og  $1.21 \cdot 10^{-4} \text{g s}^{-1}$ , for 50.9 mg og 149.9 mg. For 62 % SiO<sub>2</sub> var de  $7.66 \cdot 10^{-5} \text{g s}^{-1}$  and  $3.06 \cdot 10^{-5} \text{g s}^{-1}$ . Oppløsningshastigheten til SiO<sub>2</sub> viste seg å være raskere for 50% SiO<sub>2</sub> sammenlignet med 62% SiO<sub>2</sub>, spesielt for slagger av liten størrelse. Resultatene viste en langsommere reaksjonshastighet ved lavere temperaturer enn tidligere forskning, noe som tyder på behovet for ytterligere undersøkelser ved høyere temperaturer innenfor driftstemperaturer ved industrien.

# Contents

<b>1</b>	<b>Introduction</b>	<b>1</b>
1.1	The silicon and ferrosilicon production . . . . .	2
1.2	Scope of work . . . . .	6
<b>2</b>	<b>Theory</b>	<b>7</b>
2.1	Slag in Si/FeSi production . . . . .	7
2.1.1	Trace elements in raw materials . . . . .	9
2.2	The SiO <sub>2</sub> –CaO–Al <sub>2</sub> O <sub>3</sub> slag system . . . . .	10
2.2.1	Ellingham diagram . . . . .	13
2.2.2	SiO <sub>2</sub> –CaO–Al <sub>2</sub> O <sub>3</sub> ternary system . . . . .	15
2.2.3	Viscosity . . . . .	16
2.2.4	Density . . . . .	18
2.3	Thermal heating of SiO <sub>2</sub> . . . . .	19
2.4	Wettability . . . . .	21
2.4.1	Reactive Wetting . . . . .	24
2.5	Dissolution rate . . . . .	26
2.5.1	Diffusion . . . . .	28
<b>3</b>	<b>Experimental</b>	<b>35</b>
3.1	Materials . . . . .	36
3.1.1	Quartz . . . . .	36
3.1.2	Slag . . . . .	36
3.2	Instruments . . . . .	37

3.2.1	Sessile drop furnace . . . . .	37
3.2.2	Electron probe microanalyzer . . . . .	38
3.3	Methods . . . . .	39
3.3.1	Wetting analysis . . . . .	39
3.3.2	Sample polishing before EPMA . . . . .	43
3.3.3	Electron probe micro analyzer . . . . .	44
<b>4</b>	<b>Results</b>	<b>45</b>
4.1	Wettability . . . . .	45
4.1.1	Sample 38 % SiO <sub>2</sub> –20 % CaO–42 % Al <sub>2</sub> O <sub>3</sub> . . . . .	47
4.1.2	Sample 50 % SiO <sub>2</sub> –21 % CaO–29 % Al <sub>2</sub> O <sub>3</sub> . . . . .	49
4.1.3	Sample 62 % SiO <sub>2</sub> –20 % CaO–18 % Al <sub>2</sub> O <sub>3</sub> . . . . .	53
4.2	Chemical analysis of slag droplets . . . . .	57
4.2.1	Sample 38 % SiO <sub>2</sub> –20 % CaO–42 % Al <sub>2</sub> O <sub>3</sub> . . . . .	57
4.2.2	Sample 50 % SiO <sub>2</sub> –21 % CaO–29 % Al <sub>2</sub> O <sub>3</sub> . . . . .	65
4.2.3	Sample 62 % SiO <sub>2</sub> –20 % CaO–18 % Al <sub>2</sub> O <sub>3</sub> . . . . .	73
4.3	Chemical analysis of cracks . . . . .	81
<b>5</b>	<b>Discussion</b>	<b>90</b>
5.1	Wetting of slag . . . . .	90
5.1.1	The effect of temperature . . . . .	93
5.1.2	The effect of slag size . . . . .	94
5.1.3	Experimental conditions affecting the wettability . . . . .	95
5.2	SiO <sub>2</sub> in slag droplet . . . . .	96
5.2.1	Internal convection . . . . .	100
5.2.2	Basicity . . . . .	101
5.3	Modeling of dissolution rate . . . . .	102
5.3.1	The effect of temperature . . . . .	105
5.4	Slag in cracks . . . . .	110

<i>CONTENTS</i>	viii
<b>6 Conclusion</b>	<b>115</b>
6.1 Further work . . . . .	117
<b>Bibliography</b>	<b>118</b>
<b>A Modeling of dissolution rate</b>	<b>125</b>

# List of Figures

1.1	Silicon furnace . . . . .	3
2.1	Excavations from Tangstad and Folstad (2021)[4] . . . . .	9
2.2	Reaction mechanism of silicate network . . . . .	12
2.3	Ellingham diagram . . . . .	14
2.4	Ternary phase diagram . . . . .	15
2.5	Viscosity diagram . . . . .	17
2.6	Density diagram . . . . .	19
2.7	Wetting angles . . . . .	22
2.8	Wetting hysteresis . . . . .	23
2.9	Effect of wetting, from Kristiansen (2022) . . . . .	26
2.10	Saturation path for different slags . . . . .	27
2.11	Schematic illustration of surface transport . . . . .	29
2.12	Diffusion with boundary conditions . . . . .	30
2.13	Dissolution rate, from Kristiansen (2022) . . . . .	33
2.14	Dissolution rate, from Kristiansen (2022) . . . . .	34
3.1	Sessile drop furnace . . . . .	38
3.2	Quartz block . . . . .	40
3.3	Experimental temperature curves . . . . .	42
4.1	Small samples from sessile drop furnace . . . . .	46
4.2	Large samples from sessile drop furnace . . . . .	46
4.3	Wetting of small sized Sample 38-20-42 . . . . .	47

4.4	Wetting of large sized Sample 38-20-42 . . . . .	48
4.5	Wetting of small sized Sample 50-21-29 . . . . .	50
4.6	Wetting of large sized Sample 50-21-29 . . . . .	51
4.7	Wetting angles of Sample 50-21-29 . . . . .	52
4.8	Wetting of small sized Sample 62-20-18 . . . . .	54
4.9	Wetting of large sized Sample 62-20-18 . . . . .	55
4.10	Wetting angles of Sample 62-20-18 . . . . .	56
4.11	BSE images of Sample 38-20-42 (61.2 mg): 0 min . . . . .	58
4.12	BSE images of Sample 38-20-42 (58.7 mg): 15 min . . . . .	59
4.13	BSE images of Sample 38-20-42 (52.9 mg): 30 min . . . . .	60
4.14	BSE images of Sample 38-20-42 (171.9 mg): 0 min . . . . .	61
4.15	BSE images of Sample 38-20-42 (147.1 mg): 15 min . . . . .	62
4.16	BSE images of Sample 38-20-42 (162.9 mg): 30 min . . . . .	63
4.17	BSE images of Sample 50-21-29 (58.5 mg): 0 min . . . . .	66
4.18	BSE images of Sample 50-21-29 (48.0 mg): 15 min . . . . .	67
4.19	BSE image of Sample 50-21-29 (50.9 mg): 30 min . . . . .	68
4.20	BSE images of Sample 50-21-29 (142.7 mg): 0 min . . . . .	69
4.21	BSE images of Sample 50-21-29 (161.8 mg): 15 min . . . . .	70
4.22	BSE images of Sample 50-21-29 (149.9 mg): 30 min . . . . .	71
4.23	BSE image of Sample 62-20-18 (55.6 mg): 0 min . . . . .	74
4.24	BSE image of Sample 62-20-18 (53.5 mg): 15 min . . . . .	75
4.25	BSE images of Sample 62-20-18 (57.6 mg): 30 min . . . . .	76
4.26	BSE images of Sample 62-20-18 (146.1 mg): 0 min . . . . .	77
4.27	BSE images of Sample 62-20-18 (144.4 mg): 15 min . . . . .	79
4.28	BSE images of Sample 62-20-18 (163.5 mg): 30 min . . . . .	80
4.29	BSE images of a crack in Sample 50-21-29 (50.9 mg): 30 min . . . . .	82
4.30	BSE images of a crack in Sample 50-21-29 (149.9 mg): 30 min . . . . .	83
4.31	BSE image of a crack in Sample 62-20-18 (55.6 mg): 0 min . . . . .	84
4.32	BSE image of a crack in Sample 62-20-18 (53.5 mg): 15 min . . . . .	85

4.33	BSE images of a crack in Sample 62-20-18 (57.6 mg): 30 min . . . . .	86
4.34	BSE image of a crack in Sample 62-20-18 (144.4 mg): 15 min . . . . .	87
4.35	BSE images of a crack in Sample 62-20-18 (163.5 mg): 30 min . . . . .	88
5.1	Wetting angles of slag samples at 1500 °C . . . . .	92
5.2	Wetting angles of slag samples at 1500 °C and 1550 °C . . . . .	94
5.3	Chemical composition of Sample 38-20-42 in drop . . . . .	97
5.4	Chemical composition of Sample 50-21-29 in drop . . . . .	98
5.5	Chemical composition of Sample 62-20-18 in drop . . . . .	99
5.6	Liquidus temperate at different silica contents . . . . .	100
5.7	Marangoni convection . . . . .	101
5.8	Average basicity ratio for each sample . . . . .	102
5.9	Dissolution rate of Sample 50-21-29 . . . . .	104
5.10	Dissolution rate of Sample 62-20-18 . . . . .	105
5.11	Dissolution rate of Sample 50-21-29 at 1500 °C and 1550 °C . . . . .	106
5.12	Dissolution rate of Sample 62-20-18 at 1500 °C and 1550 °C . . . . .	107
5.13	Estimated rate constant from an Arrhenius plot . . . . .	108
5.14	Cross-sectional view of the silica content in samples . . . . .	111
5.15	Linear fit of silica content in cracks . . . . .	113

# List of Tables

2.1	Trace elements in raw materials . . . . .	10
2.2	Properties of silica structures . . . . .	21
3.1	Chemical analyses of raw materials . . . . .	36
3.2	Chemical compositions of slag samples . . . . .	37
3.3	Experimental parameters in the sessile drop furnace . . . . .	42
3.4	Working parameters in EPMA . . . . .	44
4.1	Softening and melting temperature for Sample 38-20-42 . . . . .	49
4.2	Softening and melting temperature for Sample 50-21-29 . . . . .	53
4.3	Softening and melting temperature for Sample 62-20-18 . . . . .	57
4.4	Corresponding BSE images and chemical analyses for Sample 38-20-42 . . . . .	58
4.5	Chemical compositions for Sample 38-20-42 (61.2 mg): 0 min . . . . .	58
4.6	Chemical compositions for Sample 38-20-42 (58.7 mg): 15 min . . . . .	59
4.7	Chemical compositions for Sample 38-20-42 (52.9 mg): 30 min . . . . .	60
4.8	Chemical compositions for Sample 38-20-42 (171.9 mg): 0 min . . . . .	61
4.9	Chemical compositions for Sample 38-20-42 (147.1 mg): 15 min . . . . .	62
4.10	Chemical compositions for Sample 38-20-42 (162.9 mg): 30 min . . . . .	64
4.11	Corresponding BSE images and chemical analyses for Sample 50-21-29 . . . . .	66
4.12	Chemical compositions for Sample 50-21-29 (58.5 mg): 0 min . . . . .	67
4.13	Chemical compositions for Sample 50-21-29 (48.0 mg): 15 min . . . . .	68
4.14	Chemical compositions for Sample 50-21-29 (50.9 mg): 30 min . . . . .	69
4.15	Chemical compositions for Sample 50-21-29 (142.7 mg): 0 min . . . . .	70

4.16	Chemical compositions for Sample 50-21-29 (161.8 mg): 15 min . . . . .	71
4.17	Chemical compositions for Sample 50-21-29 (149.9 mg): 30 min . . . . .	72
4.18	Corresponding BSE images and chemical analyses for Sample 62-20-42 . . . . .	73
4.19	Chemical compositions for Sample 62-20-18 (55.6 mg): 0 min . . . . .	74
4.20	Chemical compositions for Sample 62-20-18 (53.5 mg): 15 min . . . . .	75
4.21	Chemical compositions for Sample 62-20-18 (57.6 mg): 30 min . . . . .	76
4.22	Chemical compositions for Sample 62-20-18 (146.1 mg): 0 min . . . . .	78
4.23	Chemical compositions for Sample 62-20-18 (144.4 mg): 15 min . . . . .	79
4.24	Chemical compositions for Sample 62-20-18 (163.5 mg): 30 min . . . . .	80
4.25	Corresponding BSE images and chemical analyses for parallels with cracks . . . . .	82
4.26	Chemical analysis of crack in Sample 50-21-29 (50.9 mg): 30 min . . . . .	83
4.27	Chemical analysis of crack in Sample 50-21-29 (149.9 mg): 30 min . . . . .	84
4.28	Chemical analysis of crack in Sample 62-20-18 (55.6 mg): 0 min . . . . .	85
4.29	Chemical analysis of crack in Sample 62-20-18 (53.5 mg): 15 min . . . . .	85
4.30	Chemical analysis of crack in Sample 62-20-18 (57.6 mg): 30 min . . . . .	86
4.31	Chemical analysis of crack in Sample 62-20-18 (144.4 mg): 30 min . . . . .	87
4.32	Chemical analysis of crack in Sample 62-20-18 (163.5 mg): 30 min . . . . .	88
5.1	Softening, melting, solidus and liquidus temperatures . . . . .	91
5.2	Contact area of slags during wetting . . . . .	95
5.3	Average silica content in modeled samples . . . . .	103
5.4	Estimated rate constant . . . . .	105
5.5	Estimated activation energy . . . . .	108
5.6	Contact area of cracks during wetting . . . . .	112
A.1	Change in SiO <sub>2</sub> for S50-30 after 30 min . . . . .	126
A.2	Change in SiO <sub>2</sub> for L50-30 after 30 min . . . . .	127
A.3	Change in SiO <sub>2</sub> for S62-30 after 30 min . . . . .	128
A.4	Change in SiO <sub>2</sub> for L62-30 after 30 min . . . . .	129

# Chapter 1

## Introduction

Today, the world is experiencing a green shift towards a more sustainable future and so is the industry. Companies have aimed their goals to more efficient production and less greenhouse gas emissions from the processes. The production of silicon (Si) and ferrosilicon (FeSi) has recently seen some changes and priorities. Thus, it is necessary to set focus on how they can be improved for the future.

Silicon is a widely utilized semiconductor that is predominantly sourced from quartz, the most abundant mineral on earth, comprising 28% of the earth's crust. Quartz primarily contains silica or silicates, from which silicon can be extracted[1]. In recent years, the demand for silicon has risen due to its extensive application in cutting-edge technological fields, including solar cells and smartphones. The shift towards sustainable energy sources has further amplified the demand for silicon in the production of solar cells. The use of silicon in solar cell technology is favored due to its abundance and well-established production processes, making it more cost-effective than alternative materials. To meet the growing demand, the production of silicon must be increased accordingly.

Ferrosilicon, an alloy with silicon, is a valuable product that significantly enhances the performance of various industrial products. In the steel manufacturing industry, ferrosilicon is widely used as a de-oxidizing agent to ensure efficient and high-quality steel produc-

tion[2]. The increasing demand for ferrosilicon in this market underscores its critical role in modern industrial processes.

## 1.1 The silicon and ferrosilicon production

Silicon (Si) and ferrosilicon (FeSi) are two materials that play a significant role in the Norwegian industry market, with Norway having a world market share of 10% Si and 5% FeSi[2]. Thus, this production is a crucial part of the Norwegian economy. Elkem ASA is currently the largest silicon producer in Norway, with five domestic plants that manufacture products such as Si, FeSi, and micro silica. The well-established production process for extracting silicon is also utilized by companies like Wacker Gmbh and Finnfjord AS. Si and FeSi are specifically selected for various applications owing to their unique physical and chemical properties.

They are produced industrially through a carbothermic reduction of silica ( $\text{SiO}_2$ ), i.e., metal oxides are reduced by using a carbon source[1]. The reducing agents can vary, with coke, charcoal, coal, and woodchips commonly used. Woodchips are a particularly interesting choice as they enhance the permeability of the charge during ferrosilicon production, i.e., they may improve the mass flow in the furnace and thus the efficiency. The raw materials consist of quartz ( $\text{SiO}_2$ ), iron oxide ( $\text{Fe}_2\text{O}_3$ ) in FeSi production, and carbon materials, collectively referred to as charge materials. The processes for producing silicon and ferrosilicon are similar, except that the ferrosilicon process involves the addition of an iron source to the melt. In Norway, these two processes are often regarded as one, owing to the high silicon content (>65%) in ferrosilicon production.

The carbothermic reduction of silica in silicon production can be described by Equation (1.1):



However, this equation only represents the basic mechanism of the reaction and does not account for the several side reactions that occur during the process. Figure 1.1 provides a more descriptive illustration of the industrial process, where the furnace is based on a 50 kW pilot oven from earlier research[1]. However, the precise geometry may vary depending on the operation history. The raw materials are fed through the top of the furnace. The furnace can be divided into different zones depending on the temperature in each zone. The low-temperature zone is located in the upper part of the furnace, while the high-temperature zone is the lower part as the temperature decreases downwards. At the high-temperature zone, a reduction in the activity of the molten silicon takes place. The electrode is submerged in the charge materials to improve the overall efficiency of the production.

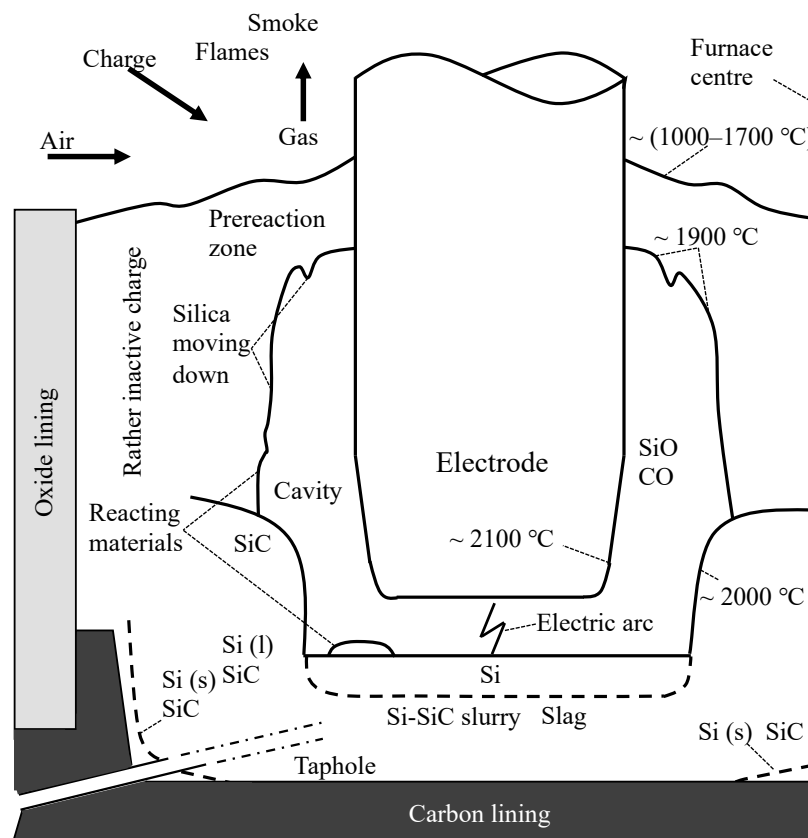
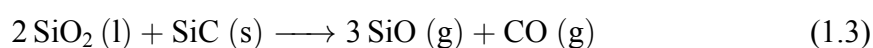
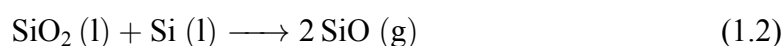
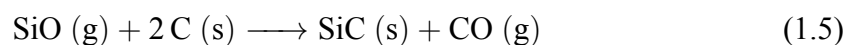
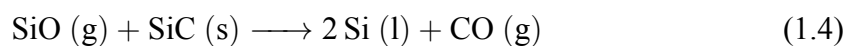


Figure 1.1: A schematic figure of the interior inside a Si furnace, reproduced from Schei et al. (1998)[1]. This figure is based on a 50 kW pilot furnace, but it is assumed that industrial furnaces have the same operations.

When quartz is added, it is directly shock heated as the temperature in the furnace is between 700 °C and 1300 °C on the surface. It reacts with either Si(l) silicon carbide (SiC) to form silicon oxide gas (SiO) and carbon monoxide gas (CO), as seen in Equations (1.2) and (1.3). These reactions mainly take place in the high-temperature zone and around the crater, from 2000 °C and higher. The temperature in this zone is critical because it affects the rate of reaction and the amount of silicon produced. The concentration of SiO gas produced by these reactions increases as the temperature rises, and this gas is used in the subsequent reactions.

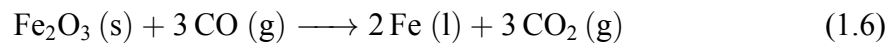


The silicon oxide gas produced in these reactions then reacts with silicon carbide to form pure silicon, as shown in Equation (1.4). The silicon is produced in the high-temperature zone, as the temperatures are quite high in this area. This reaction requires a minimum pressure of 0.7 bar SiO and a temperature above 1811 °C to be thermodynamically possible. In addition, some of the gas may ascend to the low-temperature zone and react with carbon to form silicon carbide, as shown in Equation (1.5). This reaction occurs from around 1300 °C.



During silicon production, any excess silicon oxide gas that does not react with carbon materials exits the system through the exhaust, leading to a low silicon yield and high power consumption due to the significant amount of SiO leaving. Additionally, the gas

that is formed in the low-temperature zone can condensate and cause a reverse reaction of Equations (1.2) and (1.3). The reduction reaction of the iron source takes place further up in the furnace compared to the SiO<sub>2</sub> reaction, as the former reaction does not require high temperatures. In this reaction, iron oxide reacts with carbon monoxide (CO), which reduces it to pure iron (Fe), as shown in Equation (1.6).



It is specifically important to achieve a high silicon yield during operation in order to make the whole process efficient and more cost-effective. Here, the amount of charge materials fed during operation is necessary to control. If a large amount of carbon is added, it will lead to a build-up of SiC in the bottom and edges of the furnace. This is to be prevented as it may result in downtime to remove the build-up.

There are some challenges associated with producing silicon and ferrosilicon, particularly concerning slag formation during the production process. The presence of slag can reduce the reaction volume in the furnace and hinder mass transport in the tap hole, presenting significant obstacles that require further research and development.

Incomplete heating in the furnace during silicon production can result in the formation of complex silicate phases with less noble oxide impurities, leading to the production of slag. The quantity of slag generated during the production process varies significantly among furnaces, with some generating substantially less than others, resulting in minimal accumulation within the furnace. When present, slag tends to accumulate on the furnace walls, in the tap hole, and at the bottom of the furnace. However, the presence of slag can negatively impact furnace operation, leading to problems such as clogging of the tap-hole due to slag accumulation[3].

The slag produced during silicon production may contain several metal oxides present in the raw materials or from additives. However, the main components of the tapped slag are silica (SiO<sub>2</sub>), calcia (CaO), and alumina (Al<sub>2</sub>O<sub>3</sub>).

## 1.2 Scope of work

The primary objective of this study is to propose the effects that are influencing the dissolution of  $\text{SiO}_2$  caused by chemical interactions between industrial quartz and different compositions of  $\text{SiO}_2$ – $\text{CaO}$ – $\text{Al}_2\text{O}_3$  slag, particularly slag compositions that are found in Si/FeSi production. In addition, the analysis of the wetting properties of various slags due to the capillary forces between the slag-quartz interface is of particular interest. This investigation is critical for understanding how the slag behaves when interacting with raw materials inside industrial furnaces. The investigation will supplement the research on how energy consumption in Si/FeSi production can be reduced by increased reaction volume.

The experimental study involves melting slags with varying amounts of  $\text{SiO}_2$ ,  $\text{CaO}$ , and  $\text{Al}_2\text{O}_3$  placed on a quartz substrate disk in a sessile drop furnace, using an inert Ar-gas environment at a constant temperature of 1500 °C. The isothermal holding time will be varied. The wettability of the slag and the dissolution of  $\text{SiO}_2$  will be investigated and analyzed using EPMA equipped with a wavelength-dispersive spectrometer (WDS). Finally, modeling of the change in  $\text{SiO}_2$  of slags will be performed to determine dissolution rates and the estimated time it takes to reach equilibrium state at 1500 °C.

# Chapter 2

## Theory

This chapter aims to provide an overview of the relevant literature on key concepts. Here, the theoretical framework of the  $\text{SiO}_2\text{--CaO--Al}_2\text{O}_3$  slag system will be discussed. The primary source for information on silicon production is the study by Schei et al. (1998)[1]. In addition, other studies from various researchers will be used to follow up on the excavations done in Si/FeSi furnaces and to supplement the understanding of the chemical interactions that take place between the slag and quartz, key concepts such as wettability and dissolution of  $\text{SiO}_2$ .

### 2.1 Slag in Si/FeSi production

Compared to other metal production processes, silicon and ferrosilicon production are considered "slag-free" processes due to the relatively low amount of slag present. However, slag formation is still expected to occur in the furnaces, which has been investigated in several studies that have identified operational challenges[3, 4, 5, 6]. One of the challenges is the accumulation of slag, which can cause the tap hole to clog. Nonetheless, the slag leaves the melt along with the final silicon and ferrosilicon and is separated post-tapping.

Recent excavations by Tangstad and Folstad (2021)[4] revealed that the slag is typically

present along the walls of the furnace, but the amount of slag varies between different furnaces. When a large amount of slag accumulates, it can begin to solidify as it is pushed up in the lower temperature zones higher up in the furnace. This causes the reaction route to become slower as the route narrows, leading to decreased production efficiency. To address this issue, calcia can be added to the melt in the form of limestone, to decrease the viscosity of the slag[7]. The addition of calcia promotes the slag's descent into the furnace, enabling the accumulated slag to exit through the tap hole. Other components, such as CaF<sub>2</sub> and MgO, have also been used to reduce the slag's viscosity[1].

In the same study, Tangstad and Folstad (2021) revealed that variations in the silica content of slag in different regions of the furnace were found, as seen in Figure 2.1[4]. Samples taken from higher regions of the furnace contained higher levels of silica, whereas those near the tapping canal had lower levels. In the tapping canal, the silica content was lower below the canal than above it. These findings are expected, as the furnace's upper part will have a higher silica content due to lower temperatures and raw material input from the top. Conversely, higher temperatures at the furnace's bottom lead to a higher reduction rate of silica, resulting in low-silica slag. The study found that the slag was symmetrically distributed horizontally, but different compositions were present vertically, reflecting the furnace's varying temperature zones.

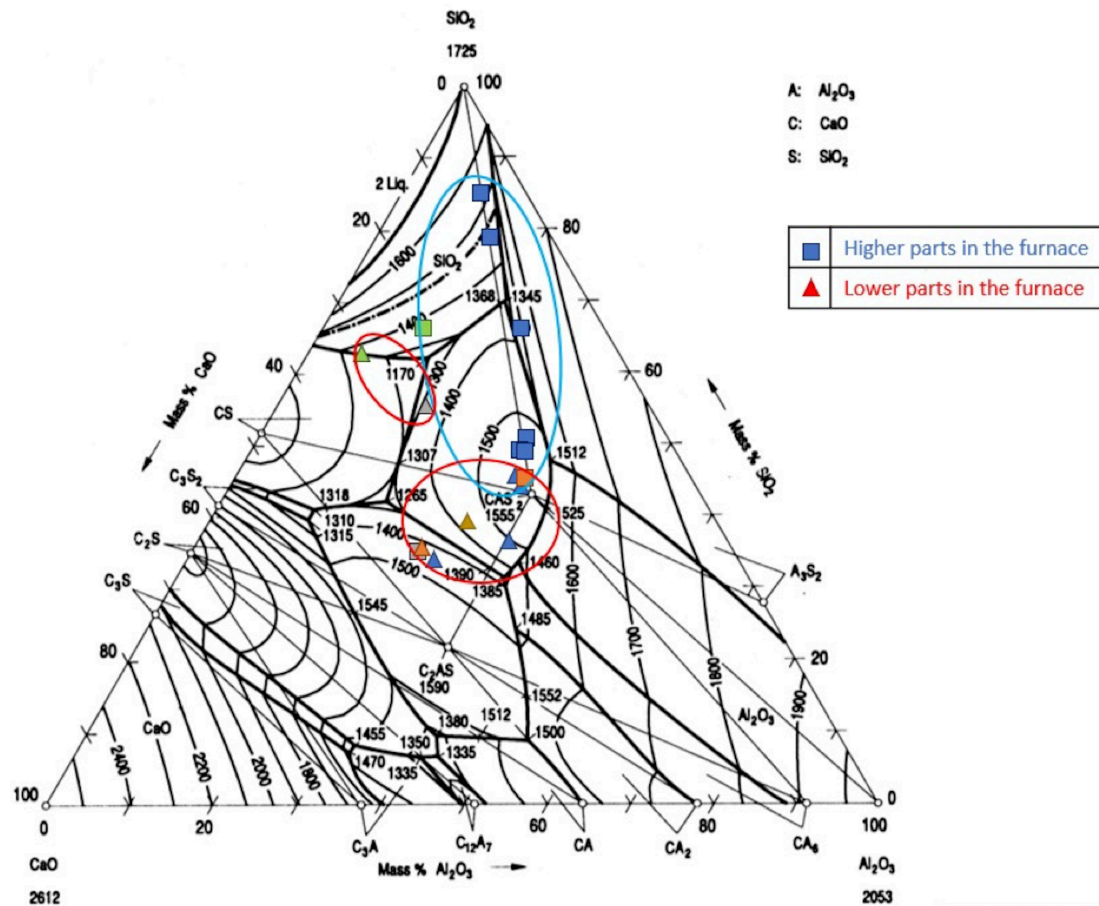


Figure 2.1: Excavations of slag samples collected from different industrial furnaces, reprinted from the work of Tangstad and Folstad (2021)[4]. The excavated samples are represented in the  $\text{SiO}_2$ - $\text{CaO}$ - $\text{Al}_2\text{O}_3$  ternary phase diagram. Slags collected above the tap hole are marked with a square and slags from the lower part of the furnace are marked with a triangle.

### 2.1.1 Trace elements in raw materials

Myrhaug (2003) conducted a study on the presence of trace elements in raw materials used in the production of silicon and ferrosilicon[8]. These trace elements enter the production process through electrodes and raw materials and exit through the tapped metal or cleaned gas. Their behavior is influenced by factors such as temperature, stability, volatility, and solubility. Myrhaug's study concluded that trace elements in Si/FeSi production are present in minor quantities measured in parts per million by weight (ppmw). The most common trace elements found in quartz are Al, S, K, Fe, and W while reducing agents

contain Al, Ti, Ca, Fe, K, Mg, S, and Na. The amount of trace elements in carbon sources varies depending on the source, such as coal, coke, charcoal, and woodchips. The trace elements and their respective quantities are listed in Table 2.1.

Table 2.1: List of trace elements that are typically present in raw materials from industrial Si/FeSi furnaces[8].

Element	Quartz [ppmw]	Carbon sources [ppmw]
Al	300-3200	100-10000
Ti	20-200	10-4000
Ca	75-160	150-4000
Fe	100-1500	100-9000
K	75-1700	75-1800
Mg	20-140	80-1400
S	5-1400	100-11000
Na	50-170	50-2100
W	0.5-640	0.5-3

Metal oxides of trace elements are mostly present in the accumulated slag, including Al, Ti, Ca, Fe, and Mg. Tapped metal contains Fe and W, while K and S are detected in the off-gas[9].

## 2.2 The $\text{SiO}_2$ – $\text{CaO}$ – $\text{Al}_2\text{O}_3$ slag system

In Si and FeSi production, slag is a by-product formed from the metals that have either not undergone reduction during the reduction process or have undergone oxidation in the refining process[10]. The slag present in Si and FeSi furnaces contains several metal oxides, including silicon oxide ( $\text{SiO}_2$ ), calcium oxide ( $\text{CaO}$ ), and aluminum oxide ( $\text{Al}_2\text{O}_3$ ), as determined from excavations[4]. Although other metal oxides may be present in the melt, this study is restricted to these three components. This combination of oxides is referred to as the  $\text{SiO}_2$ – $\text{CaO}$ – $\text{Al}_2\text{O}_3$  slag system, which will be discussed more in-depth. Despite these being the main components of the slag, other elements can be added to the melt to enhance its properties. For example,  $\text{CaF}_2$  or  $\text{MgO}$  may be added to reduce the

viscosity of the melt[1].

Molten  $\text{SiO}_2\text{-CaO-AL}_2\text{O}_3$  slag is a very complex concept in silicon production. It consists of ions rather than molecules from the materials, and the crystalline phase of silicon oxide is absent. The  $\text{SiO}_4^{4-}$ -ion is formed in the melt of the  $\text{SiO}_2\text{-CaO-AL}_2\text{O}_3$  slag system through the acidic oxide,  $\text{SiO}_2$ . This ion is composed of a central  $\text{Si}^{4+}$ -ion surrounded by four bridging  $\text{O}^{2-}$ -ions arranged in a tetrahedral structure. The  $\text{O}^{2-}$  ions from  $\text{SiO}_2$  in the slag connect two  $\text{Si}^{4+}$  tetrahedra, resulting in the formation of a polymerized network structure. Hence,  $\text{SiO}_2$  is classified as a network former[11]. The formation of silicate ions is presented in Equation (2.1):



The high viscosity of pure silica is attributed to its extensive network structure, which is connected to multiple tetrahedra. A higher quantity of silica in the melt leads to an increase in the size of the network structure, thereby resulting in a higher degree of polymerization[12]. Further, reducing the silica content and adding calcia to the slag will decrease the size of the network structure, leading to a lower degree of polymerization as fewer silicate ions are present. This phenomenon explains the observed relationship between higher silica content and higher viscosity.

In the context of several slag systems, univalent or divalent cations can act as network breakers, which have weaker attractive forces with oxygen compared to network formers[13]. When network breakers such as  $\text{CaO}$  are introduced to the silicate network, they donate oxygen to the network formers, resulting in the breakdown of the bridging  $\text{Si-O}$  bonds and the weakening of the network structure. Consequently,  $\text{CaO}$  is classified as a network breaker in this slag system. The reaction of calcia is shown in Equation (2.2).



Figure 2.2 shows the mechanism of how a network breaker can split the polymerized networking structure containing silicates.

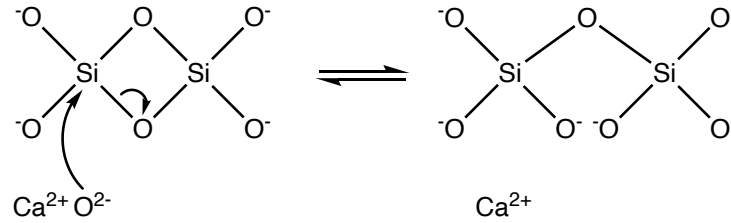
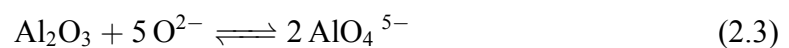


Figure 2.2: Mechanism of calcia as a network breaker splitting the networking structure of silicates.

The role of  $\text{Al}_2\text{O}_3$  in the  $\text{SiO}_2\text{-CaO-AL}_2\text{O}_3$  slag system depends on the quantity added. Generally, when added in smaller amounts,  $\text{Al}_2\text{O}_3$  acts as a network former as the  $\text{Al}^{3+}$ -ions are incorporated into the silicate network and display fourfold coordination. However, when larger amounts of  $\text{Al}_2\text{O}_3$  are added, the  $\text{Al}^{3+}$ -ions exhibit a five- or sixfold coordination, and  $\text{Al}_2\text{O}_3$  functions as a network breaker[14]. The behavior of  $\text{Al}_2\text{O}_3$  is influenced by the amounts of  $\text{SiO}_2$  and  $\text{CaO}$  present in the system. According to investigations by Kozakevitch,  $\text{Al}_2\text{O}_3$  acts as a network former when  $\text{CaO}/\text{Al}_2\text{O}_3 < 1$  and as a network breaker when  $\text{CaO}/\text{Al}_2\text{O}_3 > 1$ [15]. Interestingly, the combination of  $\text{Al}_2\text{O}_3$  as both a network former and breaker is referred to as an amphoteric. His results indicate a sharp rise in the activation energy of the viscous flow with increasing  $\text{Al}_2\text{O}_3$  content until  $\text{CaO}/\text{Al}_2\text{O}_3$  ratio reaches 1. Equations (2.3) and (2.4) present the acidic and basic reactions of alumina, respectively.



Higher content of alumina has proven to show the same phenomena as silica in molten slag. It will increase the viscosity and is related to the polymerization of the networking structure which has been previously mentioned[16, 17].

The coulomb interaction between the cation and oxygen anion in metal oxides can be described by Equation (2.5)[13]:

$$I = \frac{2z}{(r_c + r_o)^2} \quad (2.5)$$

Here,  $I$  is the ion-oxygen parameter, 2 is the oxygen valence,  $z$  is the valence of the respective cation, while  $r_c$  and  $r_o$  are the ionic radii for the cation and oxygen ion, respectively.  $I$  is relatively large when the cation and oxygen show strong interactions with each other, while smaller  $I$  suggests weaker interactions. Normally, when  $I > 1.7$ , the metal oxide is a network former, whilst  $I < 0.7$  is the value for network breakers. Amphoteric oxides normally lie somewhere between  $0.7 < I < 1.7$ .

### 2.2.1 Ellingham diagram

The standard Gibbs free energy equation is presented in Equation (2.6), where  $\Delta H^0$  is the enthalpy change,  $T$  is the temperature and  $\Delta S^0$  is the entropy change. This relation explains the thermodynamics of a system.

$$\Delta G^0 = \Delta H^0 - T\Delta S^0 \quad (2.6)$$

As the temperature decreases and  $\Delta H^0$  increases,  $\Delta G^0$  will be increased accordingly. The reaction will be at equilibrium when  $\Delta G^0 = 0$ . Lastly, when  $\Delta G^0 \leq 0$ , the reaction becomes spontaneous.

By implementing the standard Gibbs free energy for a system, it is possible to construct an Ellingham diagram. The Ellingham diagram can be used to interpret how the different

metal oxides in Si/FeSi furnaces behave under a carbothermic reduction. Figure 2.3 shows how silica, calcia, and alumina are reduced in a carbon reduction, retrieved from HSC Chemistry 9. It presents the standard Gibbs free energy,  $\Delta G^0$ , as a function of temperature. The diagram follows an assumption that the materials are in a reference state without impurities. In reality, this is not the typical scenario in operational use. By definition, a material will be reduced when  $\Delta G^0 \leq 0$ .

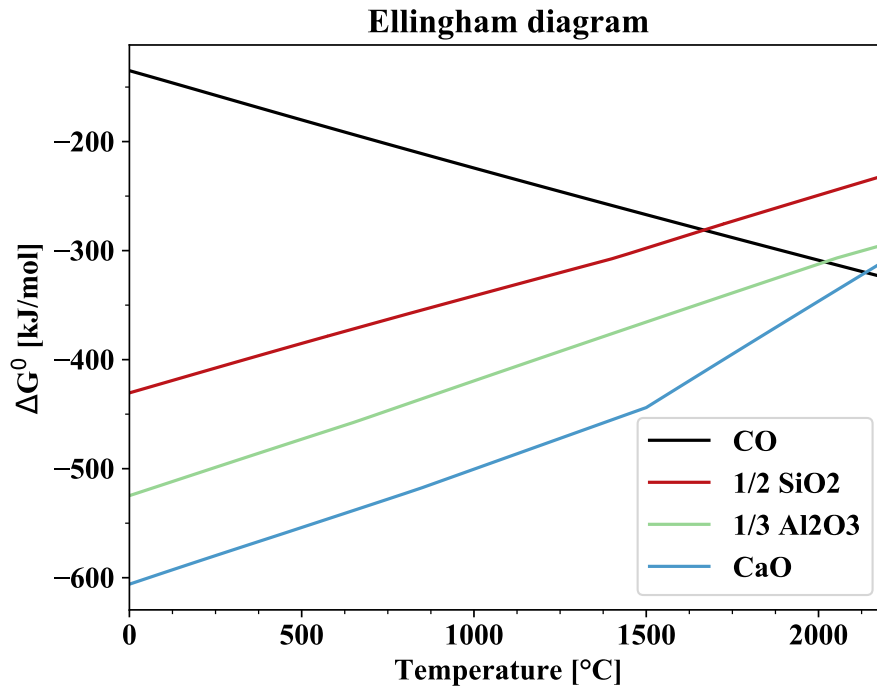


Figure 2.3: Ellingham diagram showing the reduction of  $\text{SiO}_2$ ,  $\text{CaO}$ , and  $\text{Al}_2\text{O}_3$  in a carbon reduction. Here,  $\Delta G^0$  is calculated by a reaction with  $\frac{1}{2}$  mol  $\text{O}_2$ . Thermodynamic data are retrieved from HSC Chemistry 9.

By interpreting the  $\Delta G^0$  for each metal oxide, it is seen that alumina and calcia are both below the silica, meaning they will be more stable in a carbothermic reduction. As they are more stable, more energy and a higher temperature are required to reduce them, resulting in a high temperature becoming spontaneous. For silica, calcia, and alumina, they become spontaneous when intersecting the CO-curve at 1650 °C, 2030 °C and 2100 °C, respectively. Thus, silica is reduced first, followed by alumina and calcia. This thermodynamic phenomenon gives rise to the science behind why metal oxides from charge materials and additives might be present in silicon slag. At 1500 °C, the slope of calcia

is suddenly increased, referring to the change in entropy resulting in the vaporization of calcia.

### 2.2.2 $\text{SiO}_2\text{-CaO-AL}_2\text{O}_3$ ternary system

The ternary phase diagram for the  $\text{SiO}_2\text{-CaO-AL}_2\text{O}_3$  slag system is presented in Figure 2.4. Here, each phase is separated with the thick, black boundary lines and the thin lines represent the liquid isotherms[18]. The straight lines within the diagram are the Alkemade lines.

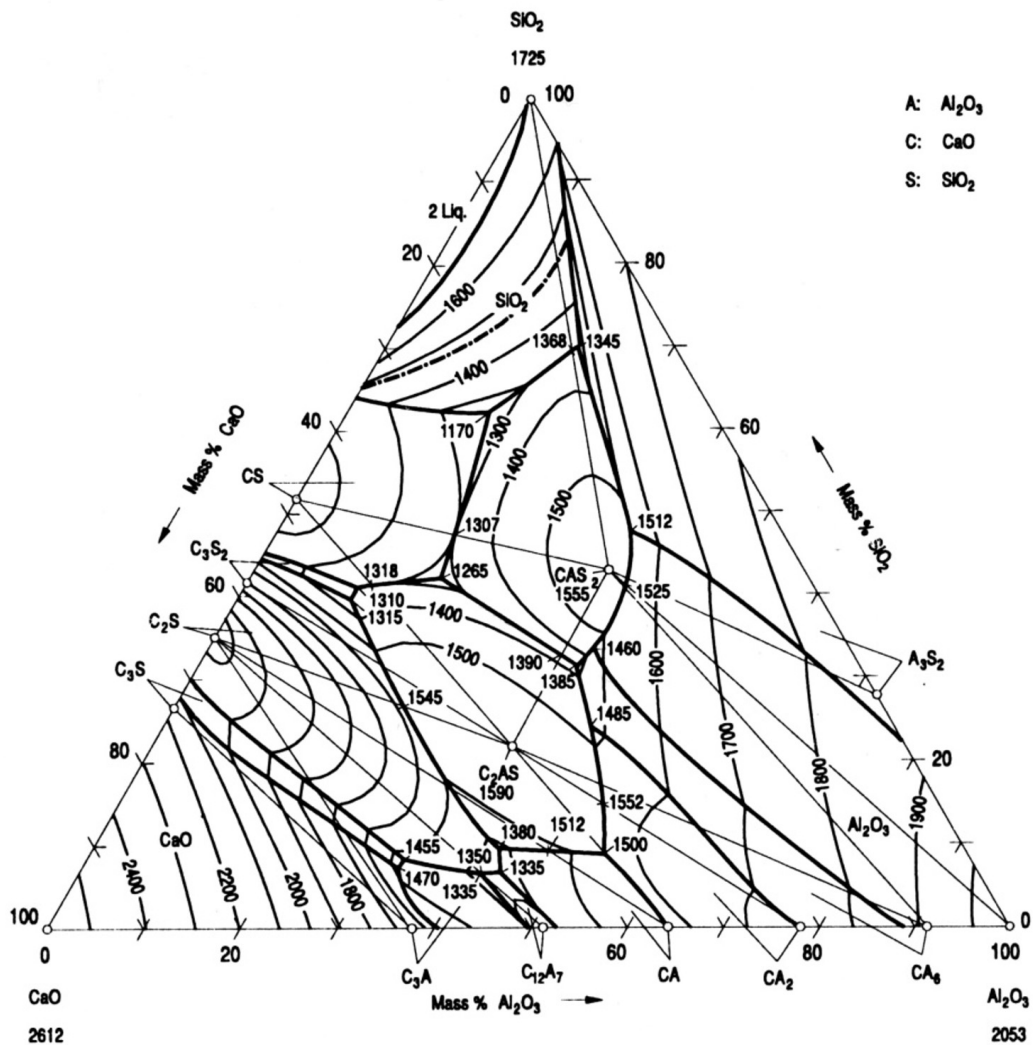


Figure 2.4: The ternary phase diagram for the  $\text{SiO}_2\text{-CaO-AL}_2\text{O}_3$  slag system[19].

In slags, one normally does not refer to the melting temperature when it is liquefied as slag systems are a more complex concept. When a slag has been completely melted it is highly dependent on the chemical composition and the temperature span is wide. Thus, liquidus temperature is used to define when the slag is completely in a liquid phase. Subsequently, solidus temperature is used to determine when the slag first start to liquefy, or the highest temperature it still can exist as a solid. The liquidus and solidus temperatures of a given slag in this system can easily be determined by interpreting the phase diagram, where these temperatures are dependent on several factors.

### 2.2.3 Viscosity

The basicity ratio of molten slag is an important factor in determining its characteristics, such as viscosity. It is defined by the unique properties of its acidic and basic oxides. The ratio is expressed in Equation (2.7) as the sum of basic oxides, such as  $\text{CaO}$ , in the numerator, and the sum of acidic oxides, such as  $\text{SiO}_2$  and  $\text{Al}_2\text{O}_3$ , in the denominator. They can be expressed in weight, mole, or volume percent. This ratio is often referred to as the basicity of the slag, and its value can be used to describe the behavior of the molten slag.

$$B = \frac{\% \text{CaO}}{\% \text{SiO}_2 + \% \text{Al}_2\text{O}_3} \quad (2.7)$$

The viscosity of the slag is heavily influenced by the acid vs. basic ratio, such as the ratio between  $\text{CaO}/\text{Al}_2\text{O}_3$ , and varies with changes in the chemical composition of the slag system[20, 21, 22]. This is seen in Figure 2.5. The viscosity lines in the figure show the viscosity at 1500 °C, although the normal tapping temperature for the slag system is between 1714 °C and 1830 °C [23]. The viscosity of the slag is one of the most important properties for high-temperature industrial processes since it determines the flow of draining the slag from the furnace and the amount of slag accumulated inside[11].

The acidic or basic behavior of alumina can be described based on the behavior of the iso-viscosity lines in Figure 2.5. The behavior of the lines is related to changes in the basicity of the slag, which ultimately affects its properties and behavior in various industrial processes. It shows that the iso-viscosity contours lie parallel to constant  $\text{CaO}/(\text{SiO}_2 + \text{Al}_2\text{O}_3)$  ratio and they are rapidly increased when  $B < 0.15$ [1]. Additionally, the contours are perpendicular with CaO reduction when the  $\text{Al}_2\text{O}_3/\text{SiO}_2$  ratio is constant, showing that viscosity increases with decreasing amount of calcia. Thus, alumina is considered acidic in the low-viscosity contours and basic in the high-viscosity contours.

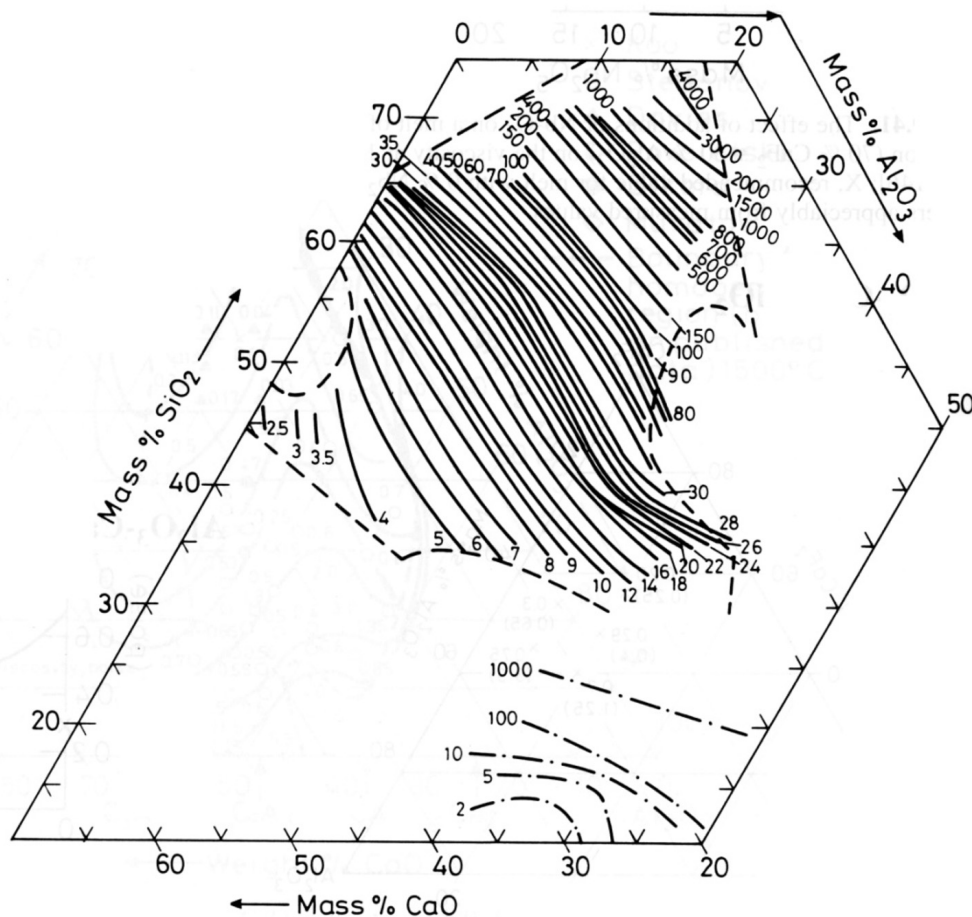


Figure 2.5: Viscosity lines for the  $\text{SiO}_2\text{-CaO-AL}_2\text{O}_3$  slag system at  $1500\text{ }^\circ\text{C}$ [19]. Recent data suggests that the values are estimated to be 20% lower[19].

In Schei et al. (1998), investigations on the viscosity of the  $\text{SiO}_2\text{-CaO-AL}_2\text{O}_3$  slag system

have been recorded. It is seen that the viscosity is dependent on the temperature and an increase in viscosity is expected when decreasing the temperature[1]. Silicon slags have earlier proved to follow this relation[24]. This is further described by the Arrhenius equation for the viscosity. The equation is presented in Equation (2.8).

$$\eta = \eta_0 \exp\left(\frac{E_\eta}{RT}\right). \quad (2.8)$$

Here,  $\eta_0$  is an Arrhenius coefficient,  $E_\eta$  is the activation energy barrier for the viscous flow,  $R$  is the universal gas constant of  $8.3145 \text{ J K}^{-1} \text{ mol}^{-1}$  and  $T$  is the temperature. The equation portrays a viscosity decrease with increasing temperature.

Several studies have recorded the change in viscosity by numerous factors. Schei et al. (1998) found that a basicity ratio lower than 0.15 leads to a rapid increase in viscosity[1]. Mills et al. (2013) showed that the viscosity of slag increases with higher concentrations of network formers like  $\text{SiO}_2$  and  $\text{Al}_2\text{O}_3$ , and lower concentrations of network breakers such as  $\text{CaO}$ [11]. Tangstad et al. (2020) also reported that higher amounts of  $\text{SiO}_2$  lead to more viscous slag [7]. On the other hand, Siafakas et al. (2018) found that increasing the  $\text{CaO}/\text{Al}_2\text{O}_3$  ratio while keeping the silica content constant resulted in a decrease in the viscosity of the slag, which was related to the depolarization of the aluminosilicate network[25]. This finding is also supported by Haghdani et al. (2021)[26].

#### 2.2.4 Density

Density plays an important role in the properties of molten slag. McGrath et al. (2014) investigated the density of the  $\text{SiO}_2\text{-CaO-Al}_2\text{O}_3$  slag system using the Archimedean single bob technique at temperatures ranging from  $1400^\circ\text{C}$  to  $1750^\circ\text{C}$ [27]. The study found that higher silica content results in lower-density slags, which is consistent with the findings in the Slag Atlas[19]. Additionally, increasing the number of basic modifiers, such as  $\text{CaO}$ , results in a higher density. The density was also found to increase with

temperature slightly. The measured densities at 1500 °C for the  $\text{SiO}_2$ – $\text{CaO}$ – $\text{Al}_2\text{O}_3$  slag system are presented in Figure 2.6. According to Schei et al. (1998), this slag typically floats on top of ferrosilicon due to its lower density, but may sink on silicon [1].

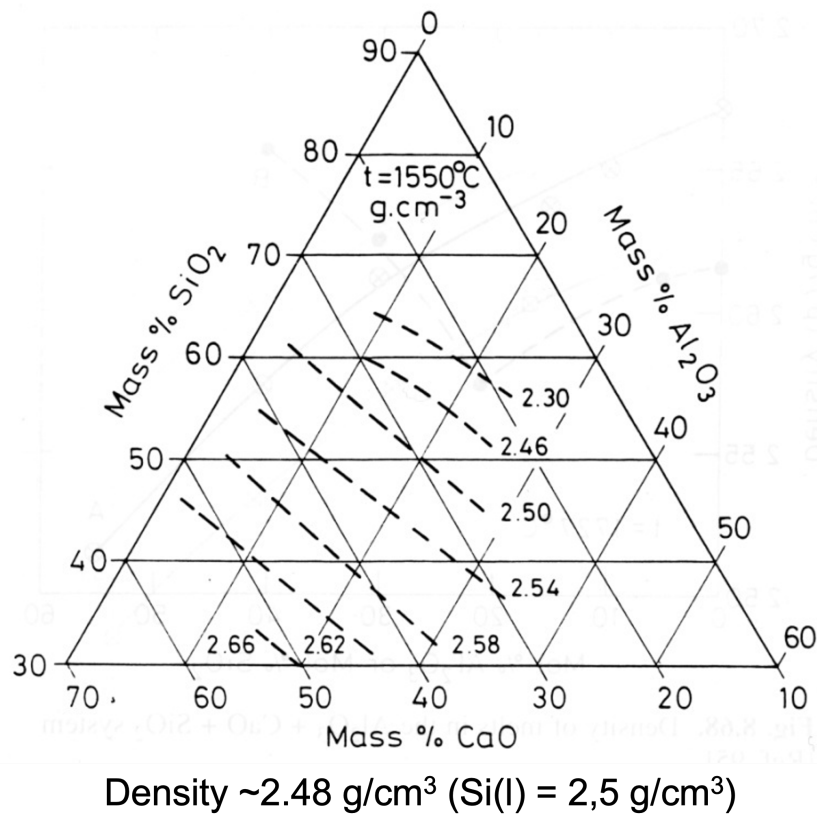


Figure 2.6: Recorded density for the  $\text{SiO}_2$ – $\text{CaO}$ – $\text{Al}_2\text{O}_3$  slag system at 1550 °C in  $\text{g cm}^{-3}$ [19].

## 2.3 Thermal heating of $\text{SiO}_2$

In materials, two different reference points are often used to describe the temperature behavior of a material when it is heated, which are known as softening temperature and melting temperature. The softening temperature is the temperature at which the material begins to liquefy and lose its sharp edges. It is typically occurring before the melting temperature, which is the temperature at which the material transitions from a solid to a liquid state[28].

Recent investigations have revealed that the melting behavior of different quartz sources has significant differences[6, 29, 30]. The studies have also shown that the softening and melting temperatures of quartz are dependent on the heating rate. Specifically, it has been found that the softening and melting temperature is increased with increasing heating rate. The main findings indicate that the quartz sources only begin to soften from 1700 °C and above when heated with relevant heating rates for industrial furnaces (5-20 °C/min). Additionally, they were not fully melted until the temperature was around 1800-1900 °C.

When a material is heated from room temperature to its melting temperature, it may exhibit a volume expansion. This is defined as an increase in volume as a result of thermal change. Solid silica has various polymorphs at different temperatures and pressures, with  $\alpha$ -quartz being the most common polymorph at room temperature and atmospheric pressure[28]. Table 2.2 presents the most important polymorphs of silica when considering industrial temperatures and pressures, with their respective density, transformation temperature, and crystal structure. Heating  $\alpha$ -quartz causes it to transform into  $\beta$ -cristobalite at 573 °C before it is transformed into either tridymite or  $\beta$ -cristobalite. According to the phase diagram of silica, tridymite is the expected transformation at 970 °C. However, earlier research has not found tridymite in industrial production and some even claim that it is not a pure silica phase[31, 32, 33]. The next phase transformation is thus to  $\beta$ -cristobalite at 1470 °C, which has been recorded to go through an amorphous phase[34]. This transformation goes through the rearranging and breaking of bonds in the crystal structure, meaning it is irreversible. This volume expansion can thus result in several cracks in the structure.

Table 2.2: Properties of different silica structures, including density, transformation temperature, and crystal structure.

Silica structure	Density[35] [kg dm <sup>-3</sup> ]	Transformation temperature[35] [°C]	Crystal structure[12]
$\alpha$ -quartz	2.6495	573	Trigonal
$\beta$ -quartz	2.5334		Hexagonal
Tridymite	2.183	970	Monoclinic
$\alpha$ -cristobalite	2.333	272	Tetragonal
$\beta$ -cristobalite	2.205	1470	Cubic
Amorphous	2.0-2.2	1300[36]	-

It is commonly believed that quartz has a theoretical increase of 22 % in volume when heated from room temperature to liquid silica at 1726 °C. However, investigations by Ringdalen et al. (2016) have shown that different industrial quartz sources exhibit differences in volume expansion and heating properties in the relevant industrial temperature zones[28]. The volume of quartz can increase up to 40%, with the transition to  $\beta$ -cristobalite during heating favoring a volume expansion. The quartz source Qz 35 exhibited a maximum volume expansion of 43 % at 1650 °C. This is due to the difference in density of the sources, as seen in Table 2.2[35].

In addition to the volume expansion caused by the phase transformation of silica, it is recorded that the cracking in industrial quartz may be caused by the grain boundaries[37]. According to Aasly (2008), cracks propagate in the mechanically weakest parts of the structure, which will be along the grain boundaries[38]. Martello (2012) found that the impurities are namely located on the grain boundaries of the silica, such that the silica will contain mineral inclusions[37]. The mineral inclusions cause the silica to crack in the grain boundaries as they usually have a lower melting temperature than silica.

## 2.4 Wettability

The wetting angle,  $\theta$ , is a key factor in determining the wettability of a material on a substrate. This phenomenon gives a representation of how well a material spreads on a

surface. The wetting is primarily driven by the surface tensions between the liquid, the gas, and the substrate[39]. Young's equation, proposed in 1805, is typically used to define the behavior of a liquid on a solid surface. The equation is presented in Equation (2.9).

$$\gamma_{sv} = \gamma_{sl} + \gamma_{lv} \cos \theta. \quad (2.9)$$

Here,  $\gamma_{sv}$  and  $\gamma_{sl}$  represent the surface tensions of the solid and liquid, respectively.  $\gamma_{lv}$  is the interfacial tension between the surface and the liquid. The wettability of a liquid on a substrate can be classified into three categories, which are no wetting condition ( $\theta = 180^\circ$ ), partial wetting condition ( $0 < \theta < 180$ ), and complete wetting condition ( $\theta = 0^\circ$ ). The three phenomena are illustrated in Figure 2.7.

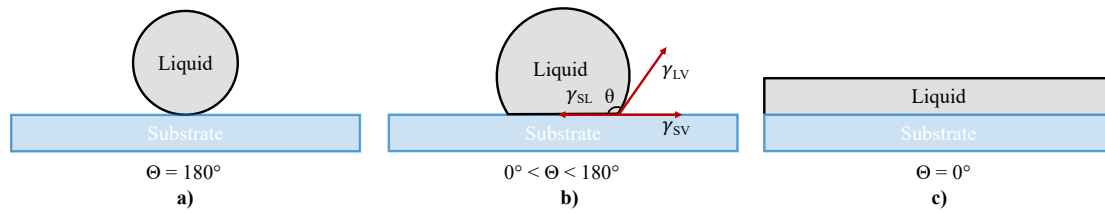


Figure 2.7: Schematic illustration of possible wetting conditions of a liquid on a solid substrate, where **a)** no wetting condition, **b)** partial wetting condition and **c)** complete wetting condition. The interfacial tensions,  $\gamma_{SV}$ ,  $\gamma_{SL}$  and  $\gamma_{LV}$  are shown for a given angle,  $\theta$ .

Several parameters can affect wettability. A higher amount of  $\text{SiO}_2$  in the slag leads to a lower surface tension, resulting in a larger wetting angle and reduced wettability [19]. In general, an increase in temperature decreases the surface tension of the liquid slag, as described by Equation (2.10). Here,  $\sigma$  is the surface tension,  $T$  is the temperature, and  $\sigma_0$  and  $\frac{d\sigma}{dT}$  are experimental constants[1]. The interfacial properties of the slag system are highly dependent on the substrate it contacts.

$$\sigma = \sigma_0 + \left( \frac{d\sigma}{dT} \right) T \quad (2.10)$$

The model shown in Figure 2.7 assumes a perfectly clean and flat surface on the substrate. In reality, the surface may not be entirely flat, and surface roughness can influence wettability. Roughness increases surface area and affects wetting conditions [40]. Wenzel proposed a roughness factor,  $R$ , that contributes to the wetting angle. The equation is shown in Equation (2.11), where  $\theta'$  is the wetting angle on a rough surface and  $\theta$  is the wetting angle on a flat surface [41].

$$R = \frac{\cos \theta'}{\cos \theta} \quad (2.11)$$

A slight tilting in the orientation has also been recorded to affect the wettability as this is considered a non-equilibrium state[42]. It is defined as a change in the wetting angle in the contact point between the solid, liquid, and gas phases caused by hysteresis. This will result in two different wetting angles in the droplet as the volume drop will shift towards the receding pathway. Figure 2.8 illustrates how the liquid can be influenced by hysteresis, as the receding angle,  $\theta_1$ , will become smaller than the ascending angle,  $\theta_2$ . Hysteresis in a sample is thus a possible deviation from the perfect equilibrium state and can give incorrect wetting properties. In addition, hysteresis has also been found to be present as a consequence of surface roughness.

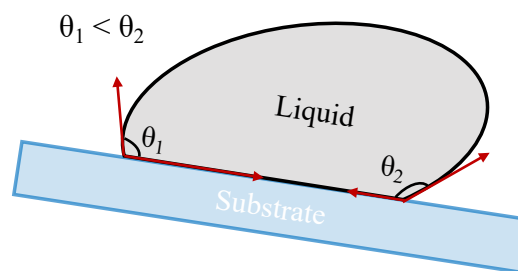


Figure 2.8: Schematic illustration of a liquid drop experiencing wetting hysteresis, where  $\theta_1 < \theta_2$ .

### 2.4.1 Reactive Wetting

Chemical interactions between the liquid and solid can occur during wetting, which influences the wettability as the system will not be in an equilibrium state[43]. The wetting angle will change continuously until it reaches equilibrium[44]. In cases where chemical reactions occur at the interface between the liquid and solid surfaces, the wetting of the liquid is defined to be reactive. An example of this is the wetting of slag on quartz, where the chemical reaction between the two materials results in a mass transfer across the interface area[45]. This reaction reduces the interfacial energy between the materials, leading to an increased wettability. The mechanism behind this is a decrease in interfacial tension due to mass transfer resulting from chemical reactions[1]. In situations where the slag contains low amounts of silica, the transfer rate is higher, resulting in a more significant decrease in interfacial tension, and thus an increased wettability. In this study, it is expected that the liquid slag will interact with the solid quartz, resulting in a greater effect on wettability. Additionally, low-silica slag is expected to be more affected by the driving force, leading to a smaller wetting angle and greater wettability.

#### **Previous work with $\text{SiO}_2 - \text{CaO} - \text{Al}_2\text{O}_3$ slag on quartz**

The wetting behavior of  $\text{SiO}_2 - \text{CaO} - \text{Al}_2\text{O}_3$  slag system on quartz has not been previously investigated by other researchers. However, Seo et al. (2001) conducted a study on the wetting of a pressed and sintered  $\text{SiO}_2$  refractory by 55.2% $\text{SiO}_2$ -29.8% $\text{CaO}$ -15% $\text{Al}_2\text{O}_3$  slag at various temperatures[46]. They found that the wetting angle decreased as the temperature increased, with wetting angles of 82°, 76°, and 31° at 1350 °C, 1400 °C, and 1470 °C, respectively. These results suggest that the wettability of the  $\text{SiO}_2$  refractory was diffusion-driven.

In another study by Yoo et al. (2021), experiments were performed on  $\beta$ -quartz single crystals with  $\text{SiO}_2 - \text{CaO}$  slag at 1600 °C[47]. The wetting angles were 55° and 20° for 67.5% $\text{SiO}_2$ -32.5% $\text{CaO}$  and 46% $\text{SiO}_2$ -54% $\text{CaO}$ , respectively, indicating that the wetta-

bility was greater for the low-silica slag. Moreover, the low-silica slag was driven by a dissolution reaction of silica, in which  $\text{SiO}_2$  was diffused into the slag, resulting in an increase in the silica content in the slag to 46.0-50.3% during wetting.

Kristiansen (2022)[48] investigated the wettability and dissolution rate of  $\text{SiO}_2$ – $\text{CaO}$ – $\text{Al}_2\text{O}_3$  slag on quartz. He conducted several wetting experiments in a sessile drop furnace by using different master slags produced in a blue furnace. The wetting experiment consisted of three different parallels with 0 min, 15 min, and 30 min holding times at 1550 °C. Three master slags were used, 38% $\text{SiO}_2$ -20% $\text{CaO}$ -42% $\text{Al}_2\text{O}_3$ , 50% $\text{SiO}_2$ -21% $\text{CaO}$ -29% $\text{Al}_2\text{O}_3$  and 62% $\text{SiO}_2$ -20% $\text{CaO}$ -18% $\text{Al}_2\text{O}_3$ , to determine possible driving forces for wetting and dissolution of silica.

The effect of wetting found is shown in Figure 2.9[48]. The results show that there is a slight increase in wetting with increasing silica content in the slag, where Sample 38-20-42 spread on the quartz rapidly when liquefied. However, Sample 62-20-42 had a lower wetting angle than Sample 50-21-29, despite it being high-silica slag with higher viscosity. He reasoned that the sample was affected by the volume expansion of quartz, causing the slag to descend in the quartz cracks, such that the drop volume was significantly reduced. Several experiments with the same slag resulted in minimal differences. It was found that the driving force for the wetting of different slags was highly influenced by the distance from the equilibrium state, such that the low-silica slag had the greatest driving force.

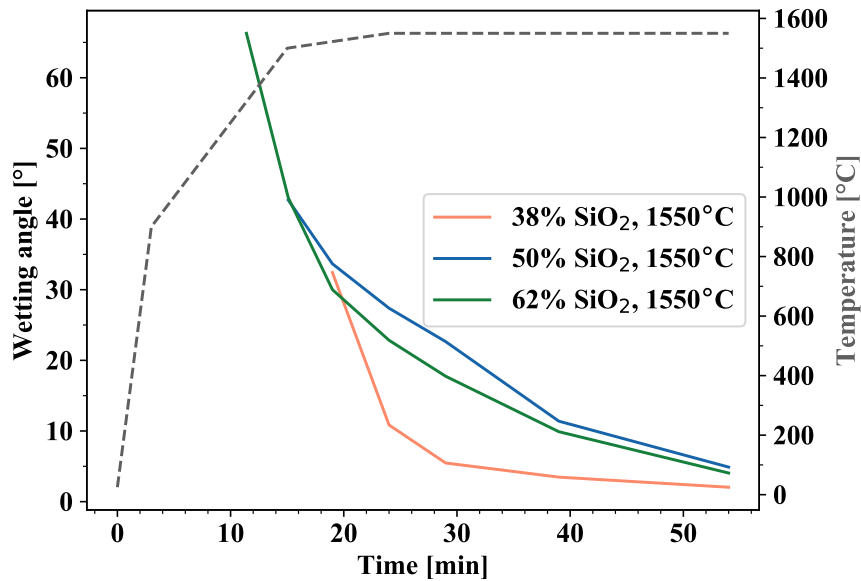


Figure 2.9: Effect of wetting in different slags from the  $\text{SiO}_2\text{-CaO-Al}_2\text{O}_3$  slag system during 30 min holding time at  $1550^\circ\text{C}$ . The results are taken from Kristiansen (2022)[48].

## 2.5 Dissolution rate

When the slag is heated at a specific temperature and liquefied on quartz, there will be a chemical reaction between the two materials. Mass transfer and dissolution of  $\text{SiO}_2$  will occur from the pure quartz into the slag, if the slag contains less  $\text{SiO}_2$  than the quartz, causing the slag to be saturated with  $\text{SiO}_2$ [10]. How fast and how much  $\text{SiO}_2$  the slag is saturated depends on several factors, namely the driving force towards the equilibrium state. The slag will have a strong driving force towards 100%  $\text{SiO}_2$  and if the slag is far from the equilibrium state, it will be saturated more rapidly.

Figure 2.10 illustrates how different slags may be saturated when in contact with quartz,  $\text{SiO}_2$ . The figure includes the saturation path for three different slag compositions, 38%  $\text{SiO}_2$ -20% $\text{CaO}$ -42% $\text{Al}_2\text{O}_3$  in red, 50% $\text{SiO}_2$ -21% $\text{CaO}$ -29% $\text{Al}_2\text{O}_3$  in blue and 62% $\text{SiO}_2$ -20% $\text{CaO}$ -18% $\text{Al}_2\text{O}_3$  in green, heated to  $1500^\circ\text{C}$ . Here, the distance from saturation concentration of  $\text{SiO}_2$  at equilibrium state ( $1500^\circ\text{C}$ ) is longer for the low-silica slag, meaning

it will experience a stronger driving force towards equilibrium, and vice-versa for the high-silica slag. As the slags come closer to the saturation concentration, the rate of dissolution decreases since the driving force becomes less significant.

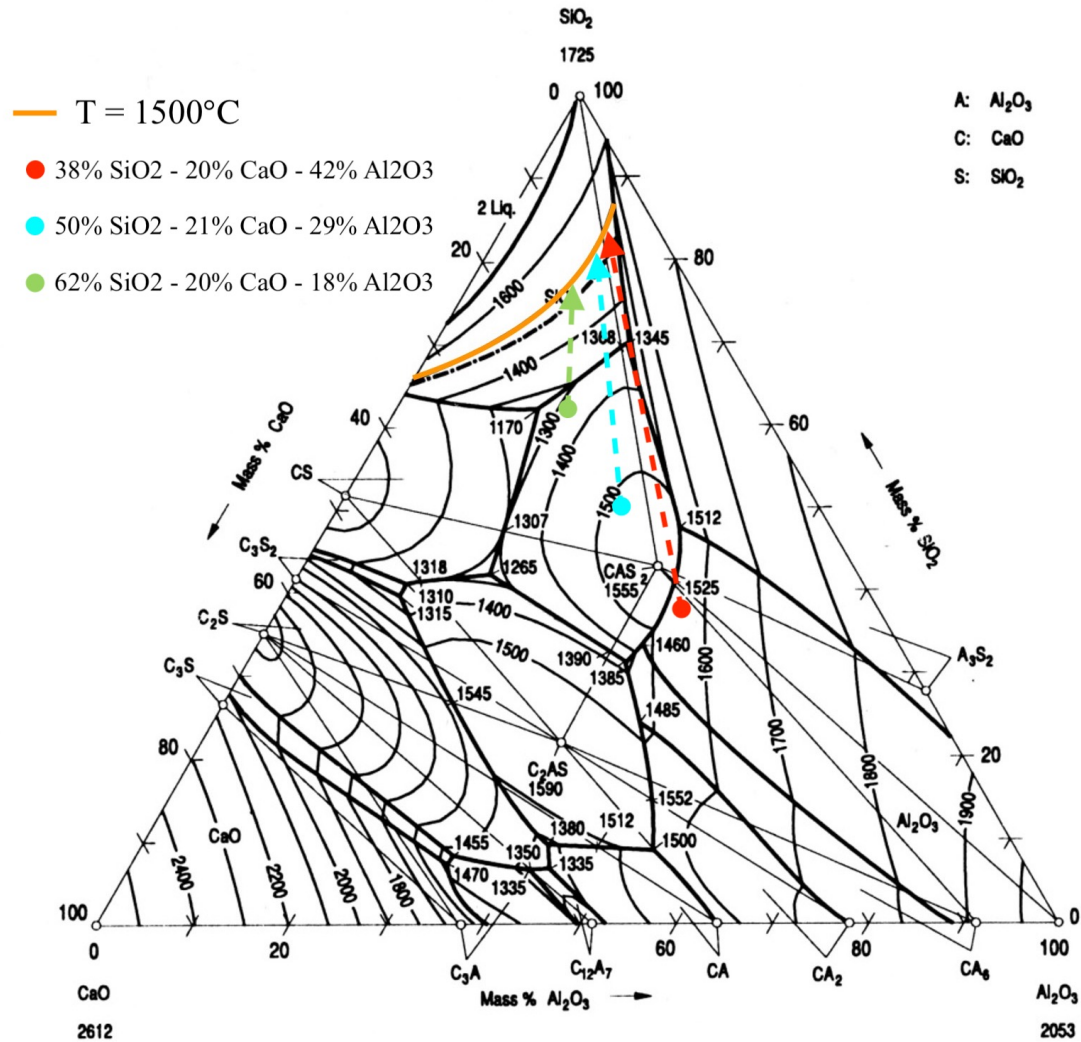


Figure 2.10: Saturation path of three different slag compositions at 1500°C in the SiO<sub>2</sub>–CaO–Al<sub>2</sub>O<sub>3</sub> phase diagram, showing the driving force to equilibrium state.

The driving force of the chemical reaction determines the rate of how fast the reaction occurs. The rate of a chemical reaction is dependent on the composition, as seen in Figure 2.10. Subsequently, the rate is influenced by the temperature. If the slags in Figure 2.10 were heated to 1600°C, the driving force would be increased as the thermodynamic properties are increased, causing the reaction rate to occur faster[10]. This relation is described in an Arrhenius equation seen in Equation (2.12), where the rate constant,  $k$ ,

is increased exponentially with an increasing temperature in the system.

$$k = k_0 \exp\left(-\frac{E_a}{RT}\right) \quad (2.12)$$

Here,  $k_0$  is the Arrhenius pre-exponential factor,  $E_a$  is the activation energy for the reaction,  $R$  is the universal gas constant, and  $T$  is the temperature.

In addition to the influence of reaction rate and temperature, it will further be dependent on the overall reaction interface between the slag and the quartz, namely the interface area. A rate equation describing this scenario has been proposed in earlier research, seen in Equation (2.13)[49, 50]. This kinetic equation shows how the reaction rate of silica,  $\frac{d(\%SiO_2)}{dt}$ , is changed during a chemical reaction between slag and quartz.

$$\frac{d(\%SiO_2)}{dt} = kA(\%SiO_2(eq) - \%SiO_2) \quad (2.13)$$

Here,  $A$  is the interface area,  $\%SiO_2(eq)$  is the silica content in equilibrium state and  $\%SiO_2$  is the silica content at a specific time during the reaction.

### 2.5.1 Diffusion

As the mass from the substrate is transferred to the material in contact with it, it will go through a surface transport[51]. Typically, the transport through the surface occurs due to a difference in concentration levels between materials, namely the concentration gradient, where the mass moves from an area of high concentration to an area of low concentration, as shown in Figure 2.11. This whole process is known as diffusion.

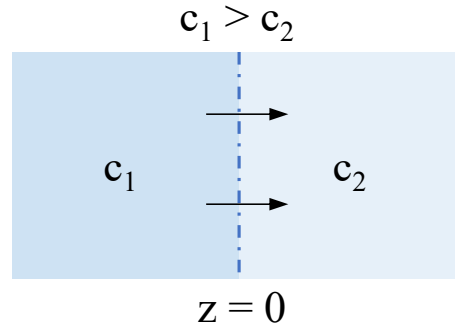


Figure 2.11: Schematic illustration of surface transport between two species. Here,  $c_1 > c_2$ .

The overall diffusion in a system between two materials can be described using Fick's second law, presented in Equation (2.14).

$$\frac{\partial c}{\partial t} = D \frac{\partial^2 c}{\partial z^2} \quad (2.14)$$

In the given equation,  $\frac{\partial c}{\partial t}$  represents the rate at which component  $c$  accumulates within a unit volume of a liquid in motion along a surface. The diffusion coefficient,  $D$ , is a quantity that expresses how fast a specie is diffused through a medium and is often driven by the physical and chemical properties of the specie. In addition, what medium it is transported through may influence the diffusivity. The rate of diffusion in Equation (2.14) is proportional to the concentration gradient.

There are specific conditions at which the unit volume in the bulk melt is approaching the surface area of the substrate. At  $t = 0$ , the concentration will be equal to the concentration of the bulk,  $c_b$ . At the surface,  $z = 0$ , the concentration is equal to the surface concentration. The conditions far from the surface,  $z \rightarrow \infty$ , follow a concentration equal to  $c_b$ .

These specific conditions give rise to the boundary conditions in Fick's second law. The boundary conditions are expressed in Equation (2.15), where  $\text{erf}\left(\frac{z}{2\sqrt{Dt}}\right)$  is an error function that can be solved numerically.

$$\frac{c - c_s}{c_b - c_s} = \operatorname{erf}\left(\frac{z}{2\sqrt{Dt}}\right) \quad (2.15)$$

The visual representation of diffusion by using boundary conditions is shown in Figure 2.12. The graph shows how the concentration profile for a given specie will behave in different time intervals.

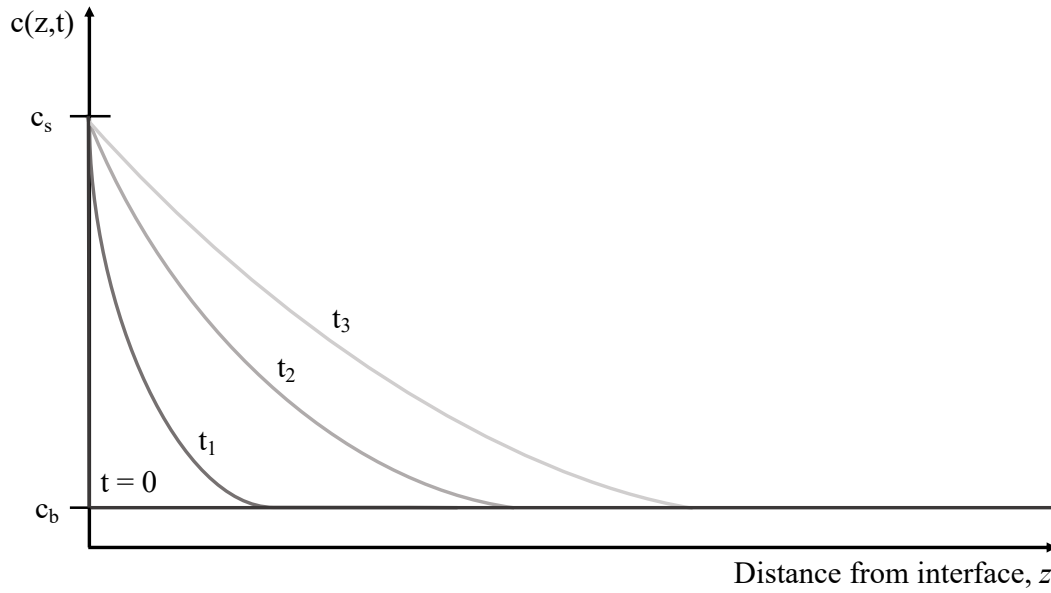


Figure 2.12: Illustration of a diffusion mechanism with boundary conditions influencing the concentration profile of the specie.

For conditions with small  $z$  and  $t$ , it can be further simplified to Equation (2.16).

$$\frac{c - c_s}{c_b - c_s} \approx \frac{z}{\sqrt{\pi Dt}} \quad (2.16)$$

By combining Equations (2.14) and (2.16), the net mass transfer rate of a reaction can be expressed. The overall equation is shown in Equation (2.17).

$$\dot{n}(t, z = 0) = -D \frac{dc}{dz} = -\frac{D(c_b - c_s)}{\sqrt{\pi Dt}} \quad (2.17)$$

Additionally, a relation between the rate constant,  $k$ , and diffusion coefficient,  $D$ , can be

proposed by integrating Equation (2.17). The equation is shown in Equation (2.18), which is the equation for mass transfer at a surface. Note that this equation assumes a perfectly clean free surface.

$$k = \left( \frac{4D}{\pi t} \right)^{\frac{1}{2}} \quad (2.18)$$

### **Previous work with SiO<sub>2</sub>–CaO–Al<sub>2</sub>O<sub>3</sub> slag on quartz**

Limited research has been conducted on the kinetics of the interaction between silicate slag systems and quartz. Nevertheless, Maroufi et al. (2015) investigated the impact of adding calcia and alumina to a silicon manganese slag on quartz at various temperatures[52]. They employed the rotating rod technique to determine the rates of dissolution and diffusivity of silica. The results indicated a significant increase in the dissolution rate as the temperature rose. Specifically, between 1400 °C and 1550 °C, the dissolution rate increased nearly tenfold, from  $3.2 \cdot 10^{-6}$  g/cm/s to  $2.5 \cdot 10^{-5}$  g/cm/s. Furthermore, it was observed that the addition of 10 wt. % calcia to the primary slag increased the dissolution rate, while the addition of silica and alumina decreased it.

Their study also revealed an increase in the diffusivity of silica with a higher degree of polymerization, which aligned well with the addition of calcia to the primary slag.

In another investigation by Feichtinger et al. (2014), the dissolution behavior of spherical SiO<sub>2</sub> particles was examined on calcia aluminosilicate slag at 1450 °C[53]. The dissolution curves varied depending on the composition of the slag. Slags with higher viscosity exhibited slower dissolution rates. These findings support the conclusions of Maroufi et al. (2015), indicating that the dissolution rate may depend on the composition and viscosity of the slag. Therefore, a higher silica content in the primary slag is expected to lead to a slower dissolution of quartz.

Kristiansen (2022)[48] investigated the dissolution rate of SiO<sub>2</sub>, where he heated differ-

ent slags on an industrial quartz source in a sessile drop furnace at 1550 °C. The three slag compositions used were 38 % SiO<sub>2</sub>–20 % CaO–42 % Al<sub>2</sub>O<sub>3</sub>, 50 % SiO<sub>2</sub>–21 % CaO–29 % Al<sub>2</sub>O<sub>3</sub> and 62 % SiO<sub>2</sub>–20 % CaO–18 % Al<sub>2</sub>O<sub>3</sub>, where he held the samples isothermally for 0 min, 15 min or 30 min. The silica content in the slag increased with increasing holding time and the rate of increase was significantly larger for low-silica slag, as a result of the deviation from equilibrium being larger for Sample 38-20-42 compared to Sample 62-20-18. The CaO/Al<sub>2</sub>O<sub>3</sub> ratio was constant in all experiments, indicating no chemical reaction occurring with alumina. The dissolution rate constants were estimated to be  $1.84 \cdot 10^{-4} \text{ g s}^{-1}$ ,  $1.65 \cdot 10^{-4} \text{ g s}^{-1}$  and  $1.27 \cdot 10^{-5} \text{ g s}^{-1}$  for Sample 38-20-42, 50-21-29 and 62-20-18, respectively. His findings matched the results from Maroufi et al. (2015) and Feichtinger et al. (2014), where a higher amount of silica in the master slag decreased the dissolution rate of SiO<sub>2</sub>.

He estimated the dissolution rate of SiO<sub>2</sub> by modeling the change of SiO<sub>2</sub> in the slag in the wet samples. He found that Sample 38-20-42 and 50-21-29 were controlled by chemical reactions and Sample 62-20-18 was diffusion controlled. According to Kristiansen (2022), the estimations indicated that the dissolution of SiO<sub>2</sub> in slag is expected to be higher for low-silica slag and vice-versa for high-silica slag, as a result of a stronger driving force toward the equilibrium state.

Figure 2.13 presents the modeled dissolution rate of SiO<sub>2</sub> for Sample 38-20-42 and 50-21-29[48]. The figure shows the average silica content modeled from 0 min to 15 min by using experimental values and the expected trend of dissolution rate over a longer period. Interpreting the curve indicates that it might take approximately 5 h before the slags reach the equilibrium state at 1550 °C, where Sample 38-20-42 has a higher dissolution rate.

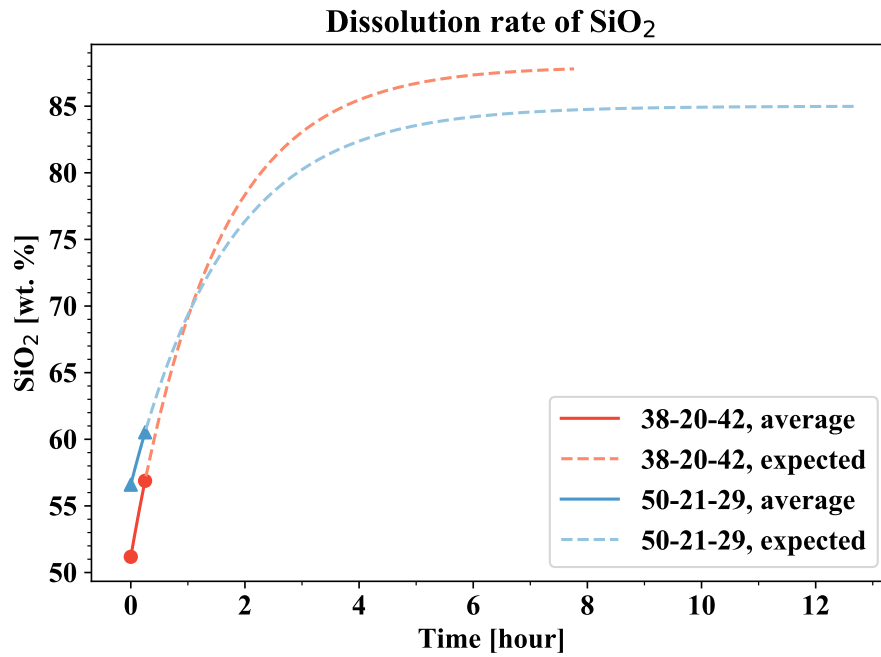


Figure 2.13: Modeled dissolution rate for Sample 38-20-42 and 50-21-29. The results are taken from Kristiansen (2022)[48].

The estimated trend for Sample 62-20-42 is presented in Figure 2.14[48]. The model is based on a diffusion-controlled mechanism. It shows that the rate is significantly slower as the slag has not yet reached an equilibrium state after 16 hours at 1550 °C. The experimental values scattered in the plot indicate that the dissolution rate might be higher than estimated. However, it shows that the dissolution of SiO<sub>2</sub> increases with increasing holding time.

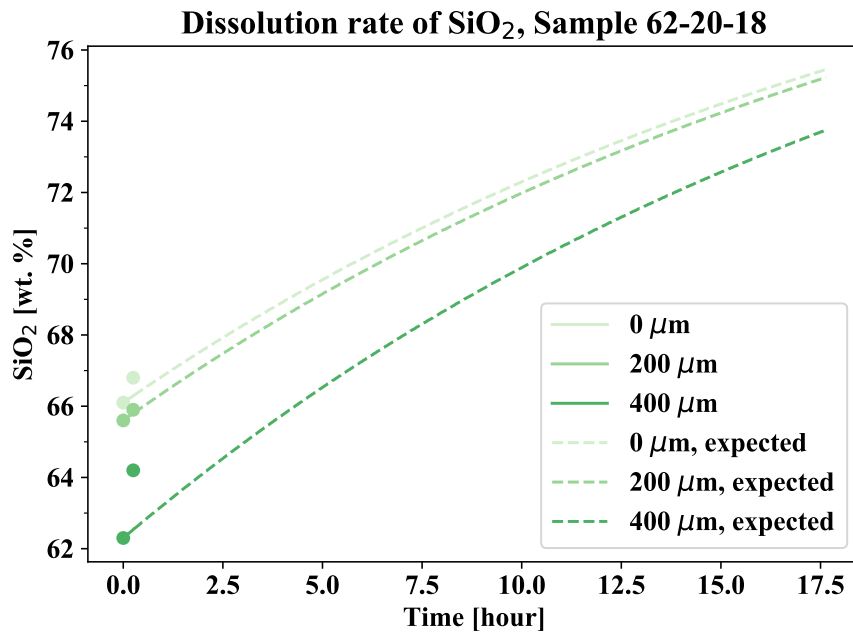


Figure 2.14: Modeled dissolution rate for Sample 62-20-18 at 0 μm, 200 μm and 400 μm from the interface. The results are taken from Kristiansen (2022)[48].

# Chapter 3

## Experimental

This chapter aims to provide the experimental work conducted in this study. Firstly, master slags and quartz substrates produced by Kristiansen (2022) were used in the wetting experiments. Each sample was then cut, molded in epoxy, and polished before they were analyzed and characterized using EPMA. Here, the chemical composition was determined. This chapter also presents the important experimental parameters used to understand the final results.

As Kristiansen (2022) investigated the wettability and dissolution rate of slags on quartz at 1550 °C, new experiments with a lower isothermal temperature were performed. The reason behind this was to investigate how the wettability and dissolution rate would be influenced by a lower temperature and how the driving force would be affected by this. In addition, the liquidus temperature for one of the samples is 1530 °C, meaning this slag would be solid during experiments with temperatures below the liquidus. This was particularly interesting to study to see how the chemical interactions between solid slag and quartz would behave. In conclusion, the experimental temperature in this study was set to 1500 °C.

## 3.1 Materials

### 3.1.1 Quartz

In this study, an industrial quartz source was chosen as the substrate disk in sessile drop experiments. Table 3.1 presents a list of trace elements that are found in the quartz. The intensity of each trace element is determined from the elemental analysis performed by the producer. This quartz was particularly chosen since the number of impurities is considerably low compared to other industrial quartz sources, meaning less chance of mineral inclusions in the substrate[6, 54].

Table 3.1: Elemental analysis of trace elements in the quartz source used in this study. The analyses were performed by the producers. Impurity levels marked with < are below the detection limit of the analysis.

Quartz	Impurity level [%]
Fe <sub>2</sub> O <sub>3</sub>	0.01500
Al <sub>2</sub> O <sub>3</sub>	0.07100
Na <sub>2</sub> O	0.01690
MgO	< 0.00090
P <sub>2</sub> O <sub>5</sub>	< 0.00090
K <sub>2</sub> O	0.02000
CaO	0.05810
TiO <sub>2</sub>	0.00200
MnO	0.00180

### 3.1.2 Slag

Master slags used in this study were produced in Kristiansen (2022)[48], where the quartz source, limestone, and alumina powder were mixed mechanically in a ring mill. They were then heated in a blue furnace at 1750 °C and held isothermally for 30 min. The chemical composition, CaO/Al<sub>2</sub>O<sub>3</sub> ratio, and the viscosity at 1600 °C and 1800 °C for each slag is presented in Table 3.2

Table 3.2: List of chemical compositions of slags from Kristiansen (2022)[48], retrieved from an elemental analysis using EPMA. The viscosity is calculated by FactSage 8.1.

Abbreviation (SiO <sub>2</sub> –CaO–Al <sub>2</sub> O <sub>3</sub> )	SiO <sub>2</sub>	CaO	Al <sub>2</sub> O <sub>3</sub>	Viscosity [poise]	
				1500 °C	1550 °C
	[wt. %]				
38-20-42	38.3 ± 0.2	20.0 ± 0.1	42.4 ± 0.2	81.9	47.8
50-21-29	49.9 ± 0.1	21.4 ± 0.2	28.5 ± 0.2	145.8	85.9
62-20-18	62.4 ± 0.2	19.8 ± 0.2	18.4 ± 0.1	257.4	155.5

## 3.2 Instruments

### 3.2.1 Sessile drop furnace

A sessile drop furnace was used to investigate the wetting abilities between the quartz and slag, the reactivity between the materials, and to observe the liquefaction of the slag in this study. This type of furnace is widely used as it can withstand very high temperatures and record the interactions between the different materials simultaneously.

A schematic figure of a sessile drop furnace is shown in Figure 3.1. Inside the furnace chamber, the sample stage is surrounded by graphite elements and radiation shields that can maintain a high temperature during operation. The in-situ temperatures inside the chamber are recorded by a C-type thermocouple and a pyrometer. The thermocouple is located right below the sample, while the pyrometer projects the internal temperature from outside the chamber. The experiment can be recorded by a high-resolution camera that is projected through a silica glass window.

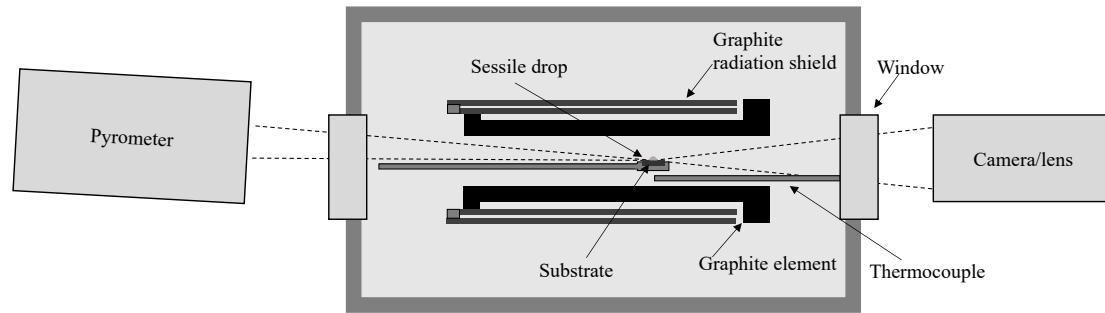


Figure 3.1: Schematic figure of a SINTEF-manufactured sessile drop furnace used in the wetting analysis. The figure is reproduced from Bao et al. (2021)[55].

This sessile drop furnace can be operated in a vacuum condition down to  $10^{-1}$  mbar. However, in reality, it usually operates at  $3 \cdot 10^{-1}$  mbar due to possible leakage in the chamber. In addition, it can be operated in an inert atmosphere with Ar-gas and in a reductive atmosphere with CO-gas. In this study, experiments were run in an inert Ar-gas environment. This furnace can operate with temperatures up to 2400 °C. The sample stage can fit samples with diameters less than 10 mm.

During operation, the thermocouple will project a more accurate internal temperature compared to the pyrometer as the thermocouple is located right next to the sample. However, the thermocouple can perform worse over time. Using the same thermocouple in several experiments results in small wear. This wear will thus cause the thermocouple to project the wrong internal temperature. To accommodate, calibrations of the furnace are important to perform regularly to determine the actual temperatures.

### 3.2.2 Electron probe microanalyzer

An electron probe microanalyzer (EPMA) is widely used to analyze samples at a microscopic scale. Here, the instrument can investigate the topography and the elements present in a sample. In this study, it was mainly used to determine the chemical composition of the slag in the samples from the sessile drop experiments.

A secondary electron microscope (SEM) can also provide a chemical analysis of a sample. However, the EPMA was chosen for the characterization as it has a higher accuracy when determining the chemical composition. In addition, the accessibility is greater and the sample stage is capable of analyzing 9 samples at the same time. In this study, the instrument JEOL JXA-8500F was used to analyze the samples. It can analyze particles larger than 1  $\mu\text{m}$ . This instrument has many similarities to a conventional SEM instrument. However, the JEOL JXA-8500F is equipped with 5 dispersive x-ray spectrometers (WDS) in addition to the EDS[56].

Inside the EPMA, the electrons from the field emission gun generate X-rays when hitting the sample surface. When reflected from the sample, the X-rays hit a crystal inside the chamber. They are further reflected to a detector. This phenomenon fulfills Bragg's law. The x-rays from the detector are further used to determine the wavelength,  $\lambda$ , for the corresponding element that is present in the sample. Here, each element has a unique set of X-rays. Since the instrument is equipped with 5 WDS detectors, it can thus map the whole element range. The instrument uses sets of standards for each element to determine which elements that are present.

## 3.3 Methods

### 3.3.1 Wetting analysis

Before the experiments, quartz disks were produced by employees in the glass-blowing workshop at NTNU. Figure 3.2 shows the drilled quartz block where the disks were extracted from the drilling holes. For each disk, the diameter was approximately 1 cm in diameter and 3 mm thick.



Figure 3.2: Image of the quartz block used to extract and produce quartz substrate disk for wetting experiments.

The slag pieces used in the wetting experiments were taken from the master slags made in the blue furnace. Here, small pieces were carefully made by crushing each slag. In this study, two different slag sizes were used to investigate a possible difference in wetting characteristics with different drop volumes. Thus, slag pieces of approximately 50 mg and 150 mg were made.

To operate the sessile drop furnace, the cooling water valves in the system were opened. The chamber door was then opened by removing the nuts and washers. A silica substrate disk was placed on the sample stage, which was connected to the chamber door. On top of the substrate, a piece of slag was placed. The sample stage and chamber door were then pushed into the furnace and secured. The stage depth inside the furnace was adjusted until it was in focus on the mounted camera. Finally, the nuts and washers were screwed back into the chamber door to secure it.

A vacuum pump was used to lower the pressure to vacuum condition in the furnace, below  $3 \cdot 10^{-1}$  mbar pressure. Following this, Ar-gas was introduced into the system at a flow rate of 1 L/min until atmospheric pressure of approximately 1 bar was achieved. Further, the Ar-gas flow rate was reduced to 0.1 L/min for the duration of the experiments.

In preparation for the experiments, a temperature calibration was conducted using iron on

an alumina substrate to calibrate the thermocouple. The iron was heated until liquefaction, and the softening and melting temperatures were recorded. The measured melting temperatures were compared to the established reference melting temperature for iron, which is 1538 °C. Any deviation between the measured and reference values indicated a necessary adjustment to the temperature to achieve the desired experimental conditions. The calibration results were utilized to determine the real internal temperature by correcting for any observed differences.

A temperature profile was designed to ensure a stable heating curve, as presented in Figure 3.3. It shows three different profiles with the same heating curve, followed by an isothermal holding time at 1500 °C that varied between each parallel. Each sample was heated for 3 minutes up to 900 °C. In the case of shock heating resulting in material dripping onto the graphite tube, causing electric shock with sparking, the heating rate was reduced after 900 °C. It was heated to 1500 °C at 50 °C/min, for approximately 12 minutes and held isothermally for 0 min, 15 min, or 30 min. The experiments performed are presented in Table 3.3, describing the slag sample used, the temperature after calibration adjusting, slag size, holding time, and sample name. The sample names correspond to the slag sample used, the slag size, and the holding time used. After cooling the samples, the Ar-gas flow was set to 0 L/min.

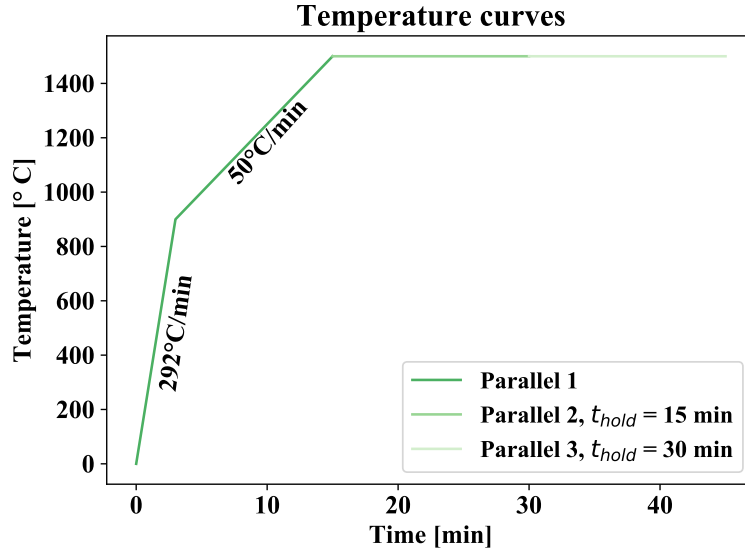


Figure 3.3: Temperature curves used in the wetting experiment experiments, showing three different parallels. Parallel 1 was heated to 1500 °C with 0 min holding time, while parallels 2 and 3 were held isothermally for 15 min and 30 min, respectively.

Table 3.3: Different parallels were used in the wetting experiments with different slag sizes and holding times. The temperature shows the set temperature after thermocouple calibration. The sample name denotes the slag used and the corresponding size and holding time, where S = small sample, L = large sample, 38, 50, and 62 denote the silica content in weight percent in each sample and 0, 15, and 30 is the holding time.

Sample (SiO <sub>2</sub> –CaO–Al <sub>2</sub> O <sub>3</sub> )	Temperature [°C]	Slag size [mg]	Holding time [min]	Sample name
38-20-42	1500 + 24	61.2	0	S38-0
	1500 + 24	58.7	15	S38-15
	1500 + 38	52.9	30	S38-30
	1500 + 24	171.9	0	L38-0
	1500 + 24	147.1	15	L38-15
	1500 + 38	162.9	30	L38-30
50-21-29	1500 + 24	58.5	0	S50-0
	1500 + 24	48.0	15	S50-15
	1500 + 38	50.9	30	S50-30
	1500 + 24	142.7	0	L50-0
	1500 + 24	161.8	15	L50-15
	1500 + 38	149.9	30	L50-30
62-20-18	1500 + 24	55.6	0	S62-0
	1500 + 24	53.5	15	S62-15
	1500 + 38	57.6	30	S62-30
	1500 + 24	146.1	0	L62-0
	1500 + 24	144.4	15	L62-15
	1500 + 38	163.5	30	L62-30

The chamber door was opened when the furnace was cooled down to below 200 °C and the samples were collected. This limitation was necessary due to the possibility of oxidation of the graphite walls when opening the chamber at higher temperatures. The final step in the procedure was to close the cooling water valves.

The wetting angles of the samples were analyzed and calculated using a post-processing software program developed by SINTEF. This software program utilized video recordings captured during operation and was based on the open-source software, ImageJ.

### **3.3.2 Sample polishing before EPMA**

After wetting experiments, each sample was molded in epoxy resin containing epoxy hardener and left overnight to harden. When hardened, a cross-section of the sample was cut by using the automatic cutting machine, Accutom-5. Finally, each cross-section was molded in epoxy once more and left overnight.

A semi-automatic polishing machine called Tegramin-30 was used to polish the samples for characterization. This instrument polishes the sample completely flat with very fine abrasives to remove the surface topography. It will also remove potential surface contamination. Here, a polishing program was made specifically for the samples in this study as the hardness of the samples is important when choosing abrasive types. The program starts with a coarse abrasive before using finer abrasives for each step. The samples were washed and cleaned in an ultrasonic bath in between the steps. The six polishing steps used were as follows:

1. MD-Piano 220 with water, run for 4 minutes.
2. MD-Plan with a DiaPro Plan 9  $\mu\text{m}$  abrasive type, run for 4 minutes.
3. MD-Dac with a DiaPro Dac 3  $\mu\text{m}$  abrasive type, run for 4 minutes.
4. MD-Nap with a DiaPro Nap B 1  $\mu\text{m}$  abrasive type, run for 3 minutes.

5. MD-Chem with an OP-S non-dry abrasive type, run for 30 seconds.

After polishing, each sample was coated with carbon to make the surface electrically conductive and further wrapped in aluminum foil. The carbon coating prevents charging, i.e., the phenomenon which makes the working conditions in SEM extremely tough and is to be prevented, as the charging will bend the electron beam such that the image quality becomes poor[57]. Before investigating the samples with an analyzer, the samples were put in a degassing oven overnight.

### 3.3.3 Electron probe micro analyzer

The wet samples from sessile drop experiments were cut into two pieces vertically. Hence, the cross-section of each sample could be analyzed. These cut samples were polished, see Section 3.3.2 for the polishing procedure. Lastly, they were carbon coated.

Each sample was studied in an EPMA to examine the chemical composition of the slag and the quartz. The EPMA analyses were performed with assistance from Senior Engineer Morten P. Raanes. He is the main operator of the instrument, JEOL JXA-8500F, located in the EM-lab at NTNU Gløshaugen. As the change in composition through the slag was the main objective, the slag composition in the droplet was analyzed vertically. Images of each sample were captured by using backscattered electron imaging (BSE). The working parameters are presented in Table 3.4.

Table 3.4: Working parameters used while analyzing the samples in the EPMA.

Acceleration voltage [kV]	Working distance [mm]	Magnification [X]
15	12	40, 400

Here, a line analysis was performed that analyzed the slag from the top of the droplet to the bottom, where the slag-quartz interface was located. The step distance was set to 100  $\mu\text{m}$ . Each analysis point in the line analysis covers an area with 30  $\mu\text{m}$  diameter. Slags located in quartz cracks were analyzed if present.

# Chapter 4

## Results

This chapter provides the results retrieved from the experimental study. Three different slag samples were used to investigate the dissolution rate of  $\text{SiO}_2$  and wettability on a quartz substrate. Moreover, the results from wettability and dissolution experiments are presented in this section. From the wetting experiments, in-situ recordings of the slags, calculated wetting angles, and experimental temperatures are presented. Further, the results of the chemical analysis of each slag sample from sessile drop experiments. The chemical compositions were determined by using an EPMA.

Each slag sample is color-coded in different plots. From this point on, Sample 38-20-42 is coded with red shades, Sample 50-21-29 with blue shades, and Sample 62-20-18 with green shades.

### 4.1 Wettability

The samples collected from each experiment are presented in Figures 4.1 and 4.2 for small-sized and large-sized samples, respectively. The sample names correspond to each experimental parallel presented in Table 3.3. Here, each substrate is approximately 1 cm wide.

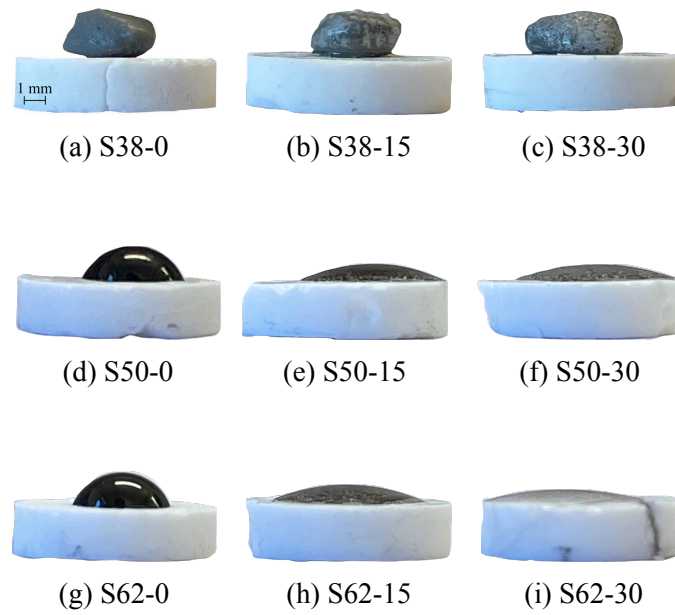


Figure 4.1: Images of the small-sized samples collected from the sessile drop furnace after each experiment. Sample names correspond to each experimental parallel in Table 3.3. The scale bar is 1 mm.

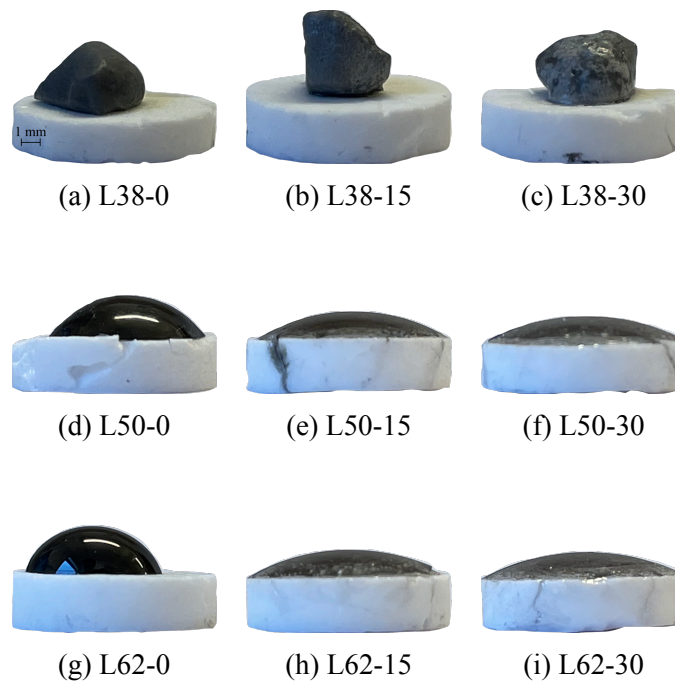


Figure 4.2: Images of the large-sized samples collected from the sessile drop furnace after each experiment. Sample names correspond to each experimental parallel in Table 3.3. The scale bar is 1 mm.

### 4.1.1 Sample 38 % SiO<sub>2</sub>–20 % CaO–42 % Al<sub>2</sub>O<sub>3</sub>

Temperature intervals of the 52.9 mg Sample 38-20-42, S38-30, are shown in Figure 4.3. The figure presents the most important time intervals during the experiment, 1000 °C, softening temperature, and the isothermal temperature 1500 °C during the holding period. The quartz substrate is the circular disk and the slag is the piece on top. The slag piece did not fully liquefy as the liquidus temperature is above the experimental temperature during heating. There was little to no change in the slag volume during the isothermal holding time. However, liquid slag was seen at the slag-quartz interface, shown in Figure 4.3j. Volume expansion in the quartz can be seen when comparing Figures 4.3a and 4.3j, from 1000 °C to 30 min holding time at 1500 °C. By analyzing the images, no significant cracks were observed.

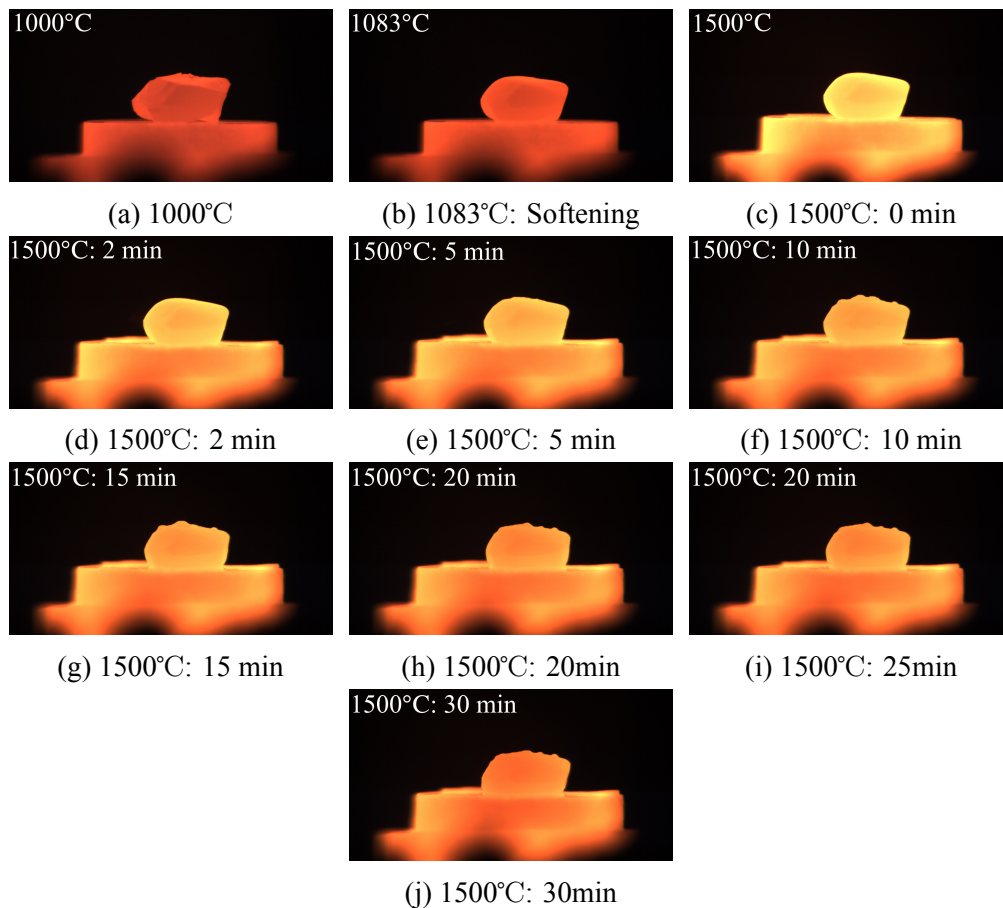


Figure 4.3: Wetting of small sized Sample 38-20-42 (52.9 mg) at different time intervals during the experiment. The substrate disk is quartz with a piece of slag on top.

Temperature intervals of the larger slag sample of Sample 38-20-42 containing 162.9 mg, L38-30, are shown in Figure 4.4. The figure presents the most important time intervals during the experiment, 1000 °C, softening temperature, and the isothermal temperature 1500 °C during the holding time. Similarly to sample S38-30, the slag bulk was solid during the experiment, as the liquidus temperature is above the experimental temperature. The slag volume during the isothermal holding time was close to constant. However, liquid slag was observed at the slag-quartz interface in Figure 4.4j. Cracks can be seen when comparing Figures 4.4a and 4.4j. From 1000 °C to 30 min holding time at 1500 °C, there has been a volume expansion in the quartz causing a cracking of the substrate. The substrate appears to be larger at the end of the experiment.

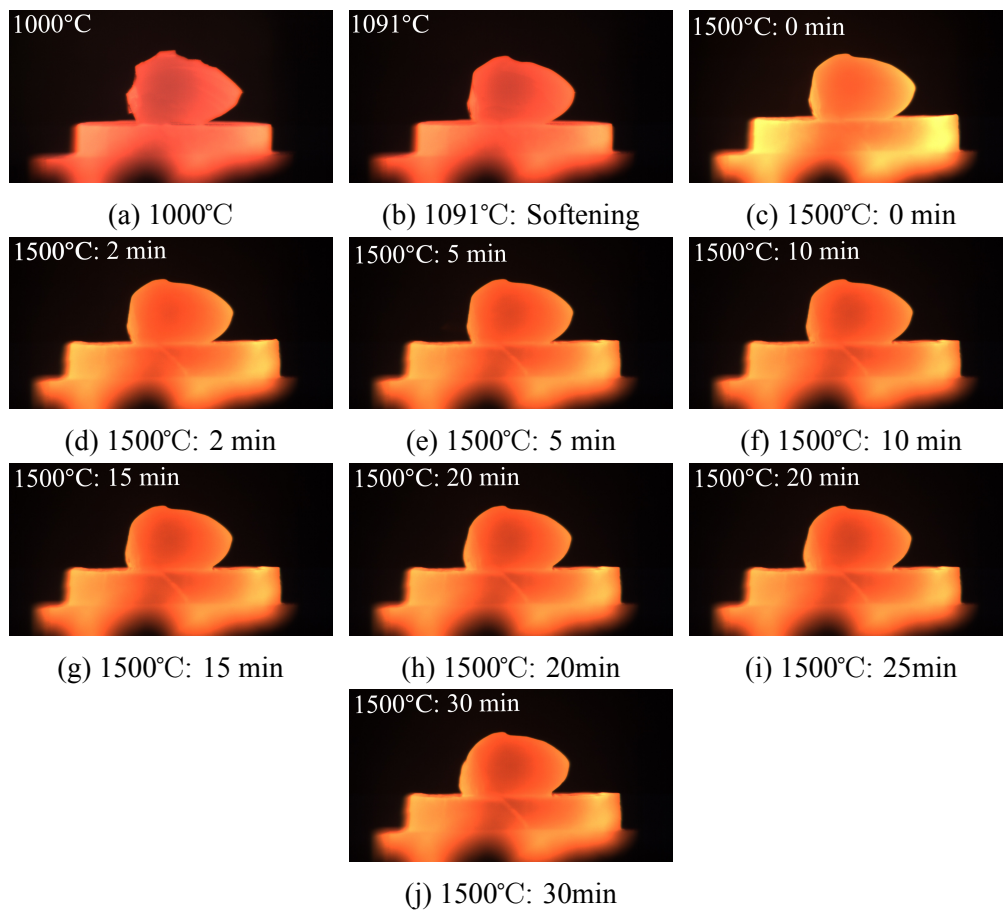


Figure 4.4: Wetting of large sized Sample 38-20-42 (162.9 mg) at different time intervals during the experiment. The substrate disk is quartz with a piece of slag on top.

The experimental softening temperature for each slag in the experiments is presented in Table 4.1. The recorded softening temperatures were similar for each slag. In addition, the

small slag samples experienced softening at the same temperature interval as the large slag samples. Since the experiments were running below the liquidus temperature, no melting temperatures were recorded.

Table 4.1: Recorded softening and melting temperatures for each experiment with Sample 38-20-42.

Sample	Softening temperature [°C]	Melting temperature [°C]
S38-0	1086	-
S38-15	1072	-
S38-30	1083	-
L38-0	1077	-
L38-15	1072	-
L38-30	1091	-

#### 4.1.2 Sample 50 % SiO<sub>2</sub> – 21 % CaO – 29 % Al<sub>2</sub>O<sub>3</sub>

Temperature intervals of the 50.9 mg Sample 50-21-29, S50-30, are shown in Figure 4.5. The figure presents the most important time intervals during the experiment, 1000 °C, softening temperature, and the isothermal temperature 1500 °C during the holding time. The slag liquefied around the isothermal temperature. From the images, it is seen that the slag was wetting the quartz surface rapidly after liquefaction and a good wetting condition was met after 30 min holding time.

Volume expansion in the quartz can be seen when comparing Figures 4.5a and 4.5j, from 1000 °C to 30 min holding time at 1500 °C. By analyzing the images, no significant cracks were observed.

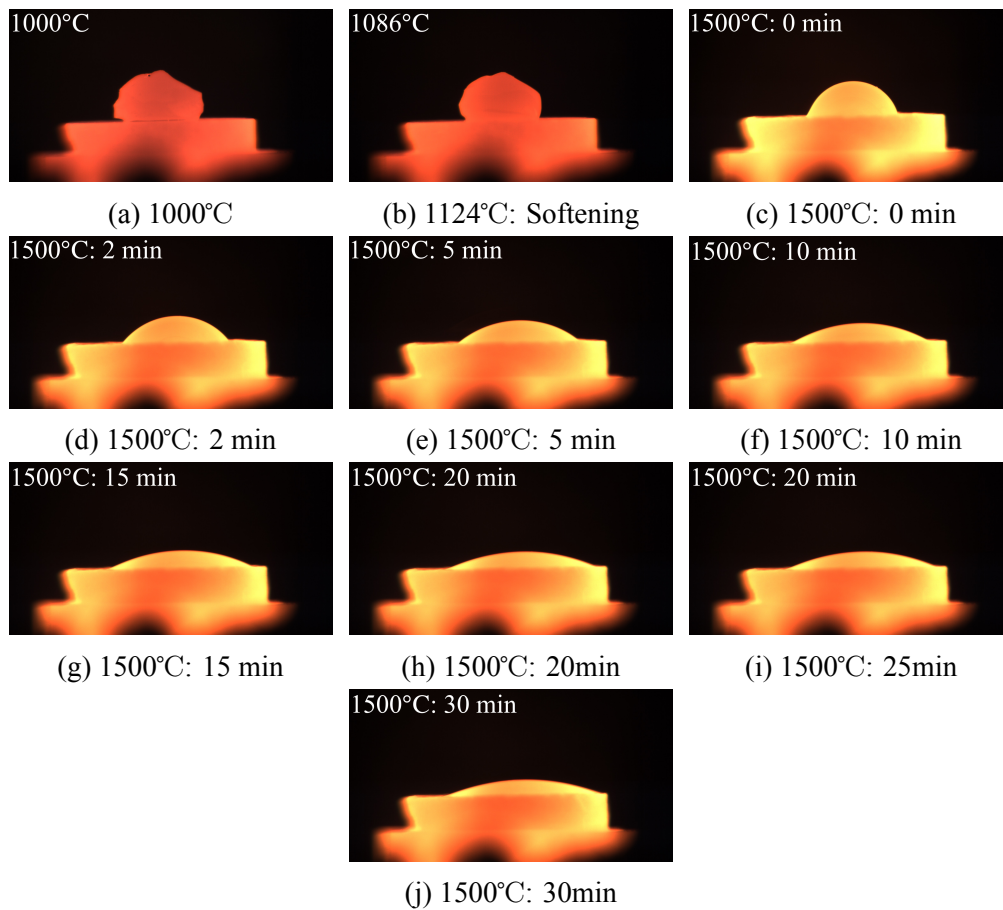


Figure 4.5: Wetting of small sized Sample 50-21-29 (50.9 mg) at different time intervals during the experiment. The substrate disk is quartz with a piece of slag on top.

Temperature intervals of the larger slag sample of Sample 50-21-29 containing 149.9 mg, L50-30, are shown in Figure 4.6. The figure presents the most important time intervals during the experiment, 1000 °C, softening temperature, and the isothermal temperature 1500 °C during the holding time. The slag liquefied around the isothermal temperature. The slag was wetting the quartz surface rapidly after liquefaction and a good wetting condition was met after 30 min holding time. It is noted that the wetting condition may have been limited by the size of the quartz substrate, as the slag wet the whole surface. Cracks can be seen when comparing Figures 4.6a and 4.6j. From 1000 °C to 30 min holding time at 1500 °C, there has been a volume expansion in the quartz causing a cracking of the substrate. The substrate appears to be larger at the end of the experiment.

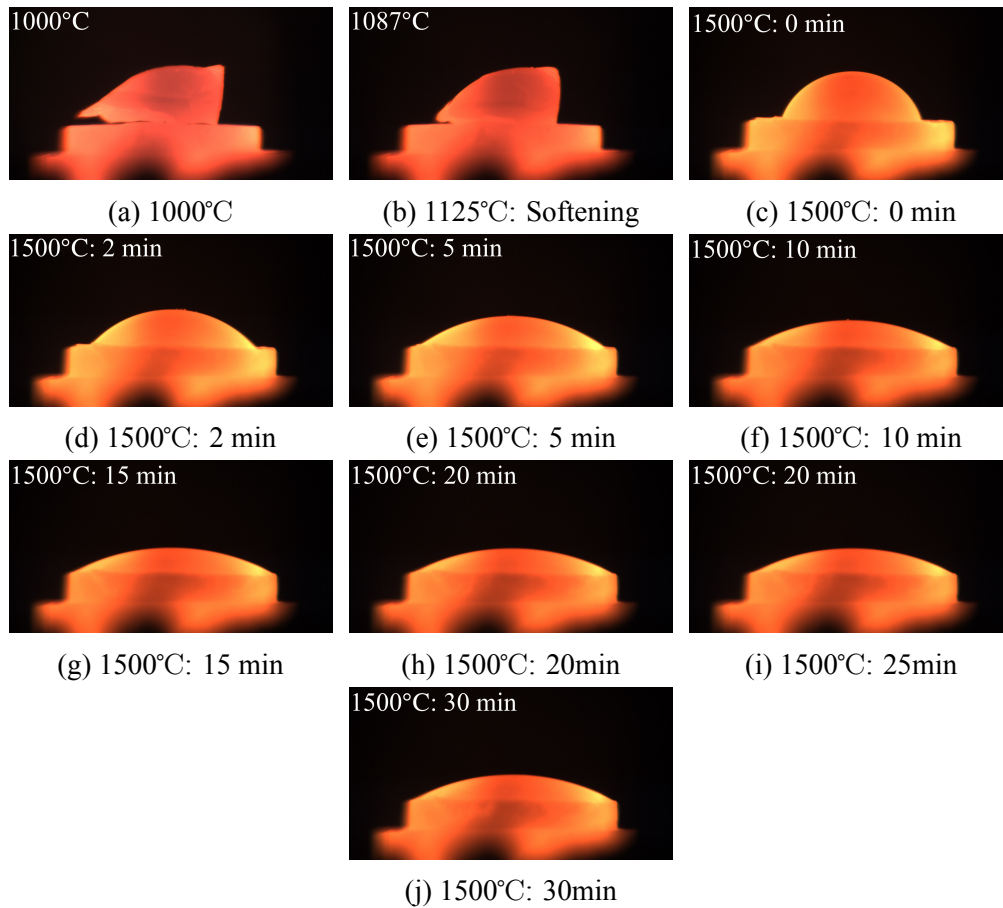


Figure 4.6: Wetting of large sized Sample 50-21-29 (149.9 mg) at different time intervals during the experiment. The substrate disk is quartz with a piece of slag on top.

Wetting angles for each experiment with Sample 50-21-29 are presented in Figure 4.7. The figure displays the wettability of the slags, from liquidus temperature to the end of the experiment, calculated by using ImageJ. The dotted gray line shows the temperature profile during wetting. Recorded wetting angles in all experiments followed the same decrease in wetting rate and showed a high similarity to one another. Both small and large slags were exhibiting the same wetting conditions. The wettability was fast from the liquidus temperature, and they wet the surface slower after 5 min holding time at 1500 °C. It shows that the slags reached good wetting conditions at the end of the experiments.

The wetting angle at liquefaction was recorded to be varying between 63.2° and 83.8°. After 30 min holding time at isothermal temperature of 1500 °C, the wetting angle was 22.0° and 23.0° for samples S50-30 and L50-30, respectively.

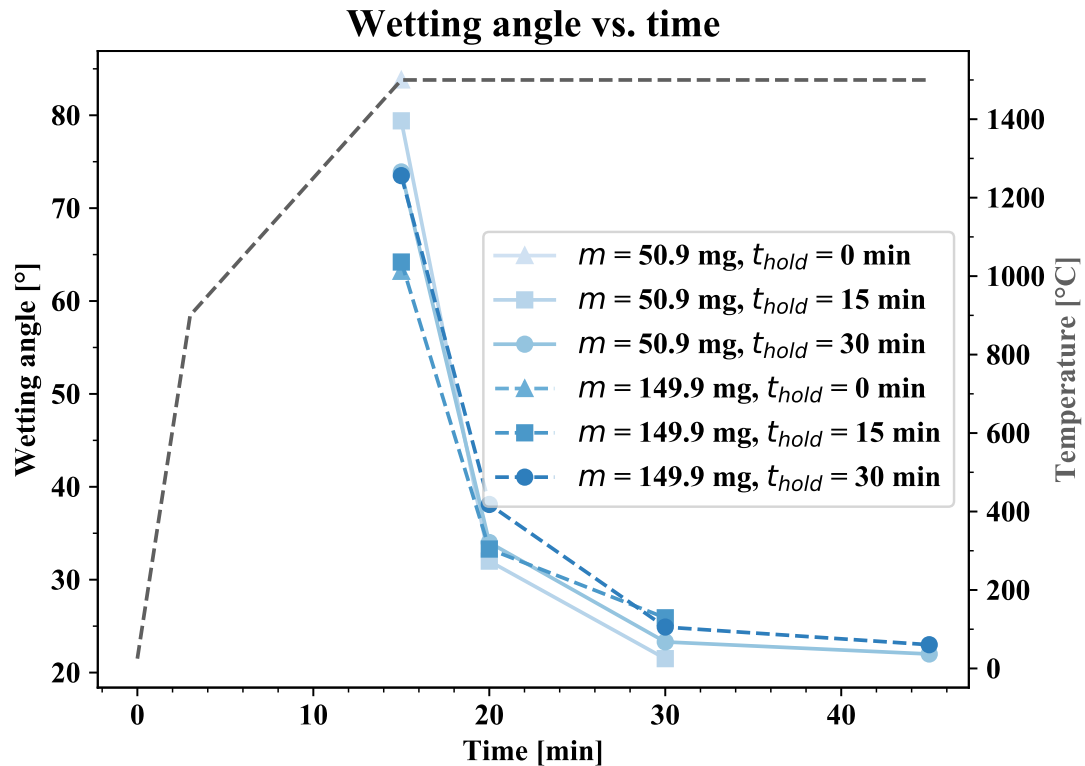


Figure 4.7: Recorded wetting angles of Sample 50-21-29 from wetting experiments.

The experimental softening temperature for each slag in the experiments is presented in Table 4.2. Similar softening temperatures were recorded for each slag, except for sample S50-30 and L50-30 which softened at 1124 °C and 1125 °C. In addition, the small slag samples experienced softening at the same temperature interval as the large slag samples. In most of the slags, melting temperatures were recorded around the isothermal temperature of 1500 °C, with samples S50-30 and L50-30 experiencing the lowest melting temperature of 1489 °C.

Table 4.2: Recorded softening and melting temperatures for each experiment with Sample 50-21-29.

Sample	Softening temperature [°C]	Melting temperature [°C]
S50-0	1085	1499
S50-15	1088	1498
S50-30	1124	1489
L50-0	1091	1500
L50-15	1081	1499
L50-30	1125	1489

### 4.1.3 Sample 62 % SiO<sub>2</sub> – 20 % CaO – 18 % Al<sub>2</sub>O<sub>3</sub>

Temperature intervals of the 57.6 mg Sample 62-20-18, S62-30, are shown in Figure 4.8. The figure presents the most important time intervals during the experiment, 1000 °C, softening temperature, melting temperature, and the isothermal temperature 1500 °C during the holding time. As seen in Figure 4.8c, the slag liquefied at 1280 °C. The slag was wetting the quartz surface at a high rate from liquefaction up to the isothermal temperature. From 5 min holding time, the rate was significantly slower. A good wetting condition was met after 30 min holding time.

Cracks can be seen when comparing Figures 4.8a and 4.8j. From 1000 °C to 30 min holding time at 1500 °C, there has been a volume expansion in the quartz causing a cracking of the substrate. The substrate appears to be larger at the end of the experiment.

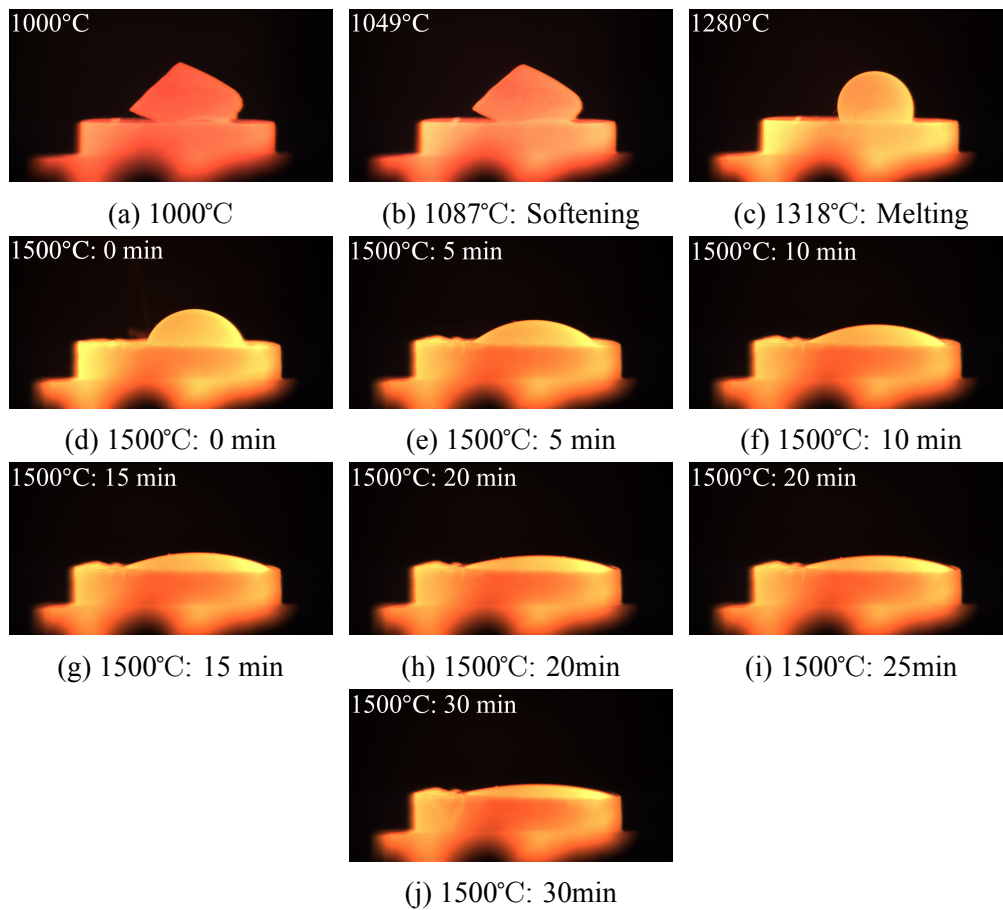


Figure 4.8: Wetting of small sized Sample 62-20-18 (57.6 mg) at different time intervals during the experiment. The substrate disk is quartz with a piece of slag on top.

Temperature intervals of the larger slag sample of Sample 62-20-18 containing 163.5 mg, L62-30, are shown in Figure 4.9. The figure presents the most important time intervals during the experiment, 1000 °C, softening temperature, melting temperature, and the isothermal temperature 1500 °C during the holding time. As seen in Figure 4.9c, the slag liquefied at 1218 °C. The slag was wetting the quartz surface rapidly after liquefaction and a good wetting condition was met after 30 min holding time. It is noted that the wetting condition may have been limited by the size of the quartz substrate, as the slag wet the whole surface.

Cracks can be seen when comparing Figures 4.9a and 4.9j. From 1000 °C to 30 min holding time at 1500 °C, there has been a volume expansion in the quartz causing a cracking of the substrate. The substrate appears to be larger at the end of the experiment.

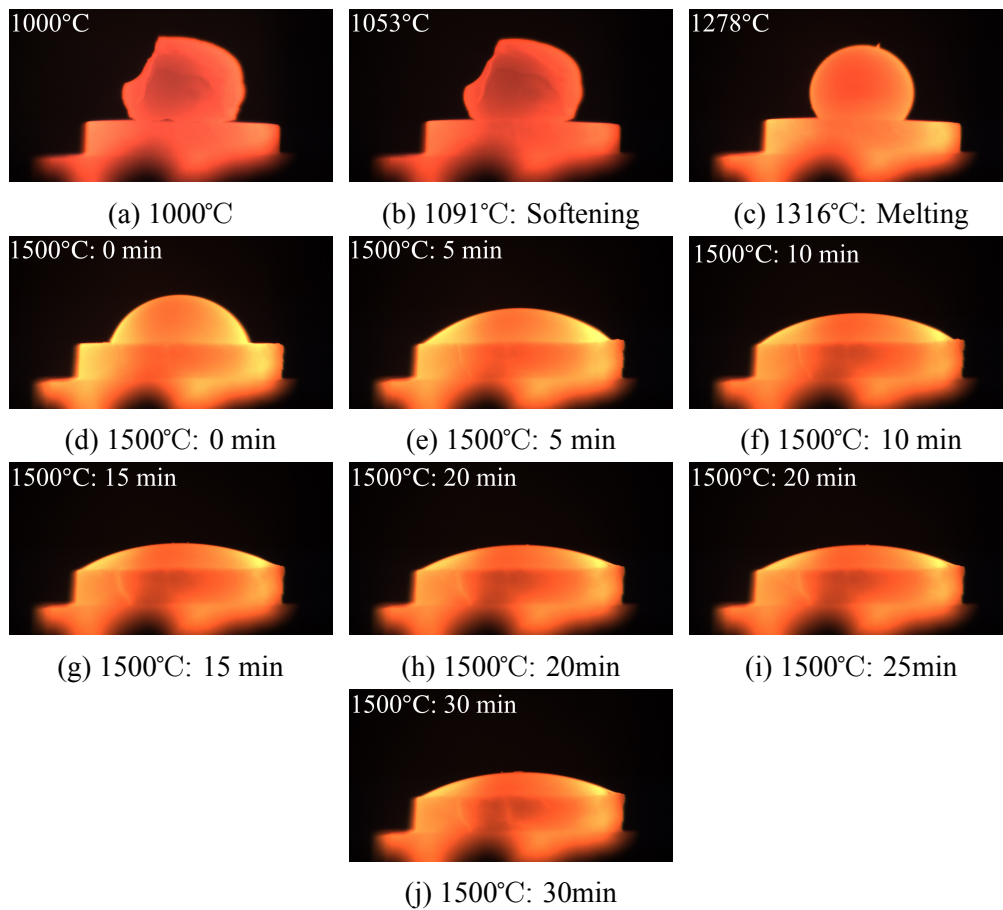


Figure 4.9: Wetting of large sized Sample 62-20-18 (163.5 mg) at different time intervals during the experiment. The substrate disk is quartz with a piece of slag on top.

Wetting angles for each experiment with Sample 62-20-18 are presented in Figure 4.10. The figure displays the wettability of the slags from liquidus temperature to the end of the experiment. The dotted gray line shows the temperature profile during wetting. Recorded wetting angles in all experiments followed the same decrease in wetting rate and showed a high similarity to one another. Both small and large slags were exhibiting the same wetting conditions, with L62-30 having a slightly larger angle at 30 min compared to S62-30. The wettability was fast from the liquidus temperature, and they wet the surface slower after 5 min holding time at 1500 °C. The slags reached good wetting conditions at the end of the experiments.

The wetting angle at liquefaction was recorded to be varying between 113.2° and 132.1°, and 70.0° and 76.9° at 1500 °C. After 30 min holding time at isothermal temperature of 1500 °C, the wetting angle was 19.7° and 26.6° for samples S62-30 and L62-30, respec-

tively.

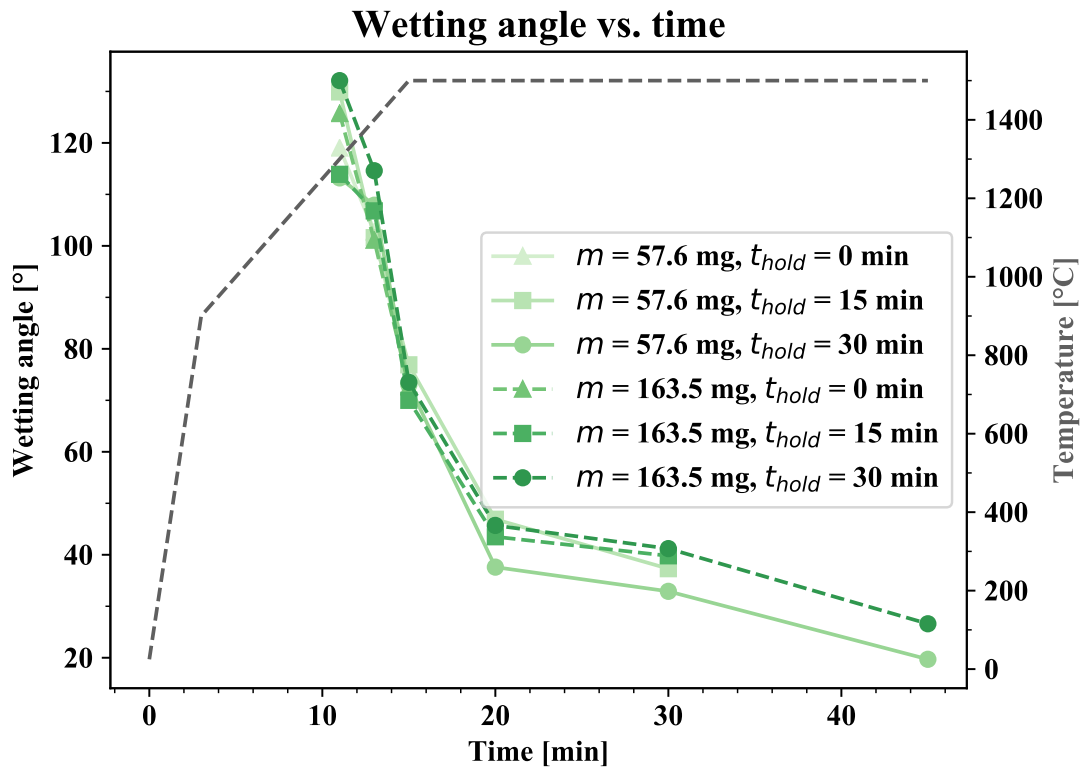


Figure 4.10: Recorded wetting angles of Sample 62-20-18 from wetting experiments.

The experimental softening temperature for each slag in the experiments is presented in Table 4.3. Similar softening temperatures were recorded for each slag, except for samples S63-30 and L63-30 which softened at 1087 °C and 1091 °C. In addition, the small slag samples experienced softening at the same temperature interval as the large slag samples. In most of the slags, melting temperatures were recorded around 1280 °C, with samples S50-30 and L50-30 experiencing the highest melting temperatures of 1318 °C and 1316 °C.

Table 4.3: Recorded softening and melting temperatures for each experiment with Sample 62-20-18.

Sample	Softening temperature [°C]	Melting temperature [°C]
S62-0	1047	1284
S62-15	1059	1282
S62-30	1087	1318
L62-0	1056	1284
L62-15	1053	1279
L62-30	1091	1316

## 4.2 Chemical analysis of slag droplets

BSE images were taken in each experiment, where a chemical analysis was performed to investigate the slag composition. In each image presented in this section, the different materials have a distinctive color shade. Here, the slag is shown with a light grey color, the quartz with dark grey, and the epoxy resin with black. This applies to all images below. The scale bar is 500  $\mu\text{m}$ , if not otherwise stated.

### 4.2.1 Sample 38 % $\text{SiO}_2$ – 20 % $\text{CaO}$ – 42 % $\text{Al}_2\text{O}_3$

The BSE images and their corresponding tables with chemical analysis are presented in Figures 4.11 to 4.13 and Tables 4.5 to 4.7 for parallels at 0 min, 15 min and 30 min holding time, using a small-sized slag. Figures 4.14 to 4.16 and Tables 4.8 to 4.10 present the parallels using large-sized slag. The numbers correspond to the point analysis done in the respective sample. The tables show the chemical composition in each point with their respective  $\text{CaO}/\text{Al}_2\text{O}_3$  ratio. To get an overview, Table 4.4 shows which figure and table belong to the respective sample.

Table 4.4: Overview of the corresponding BSE images and chemical analyses for each parallel performed with Sample 38-20-42.

Sample	Figure	Table
S38-0	4.11	4.5
S38-15	4.12	4.6
S38-30	4.13	4.7
L38-0	4.14	4.8
L38-15	4.15	4.9
L38-30	4.16	4.10

### S38-0: 61.2 mg, 0 min holding time

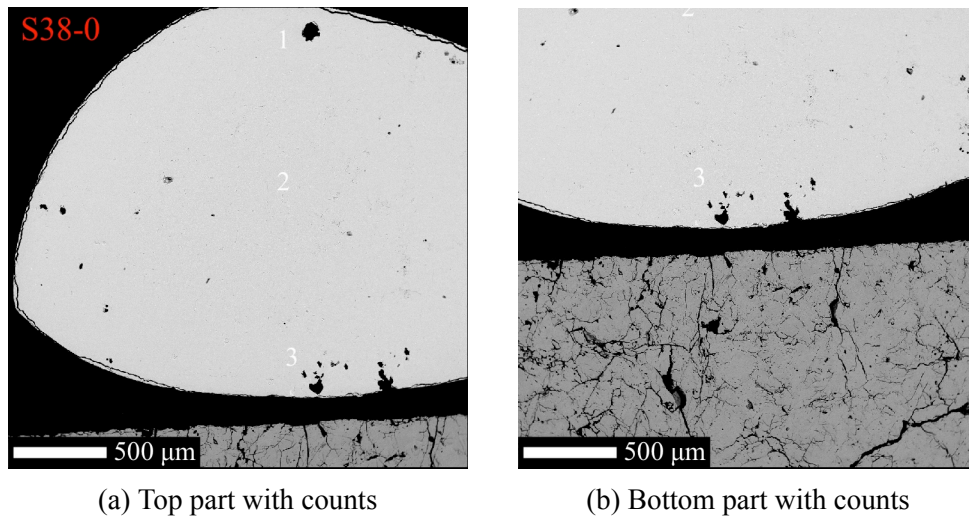


Figure 4.11: Images of Sample 38-20-42 (61.2 mg) after 0 min holding time, retrieved from the EPMA analysis with 40x magnification.

Table 4.5: The chemical compositions for Sample 38-20-42 (61.2 mg) after 0 min, retrieved from the chemical analysis in EPMA. Here, each analysis number refers to the points in Figure 4.11.

Wet sample	Analysis	SiO <sub>2</sub>	CaO	Al <sub>2</sub> O <sub>3</sub>	CaO/Al <sub>2</sub> O <sub>3</sub>
		[wt. %]			
S38-0	1	38.8	41.7	20.0	0.48
	2	38.7	41.5	20.3	0.49
	3	38.9	41.5	20.3	0.49

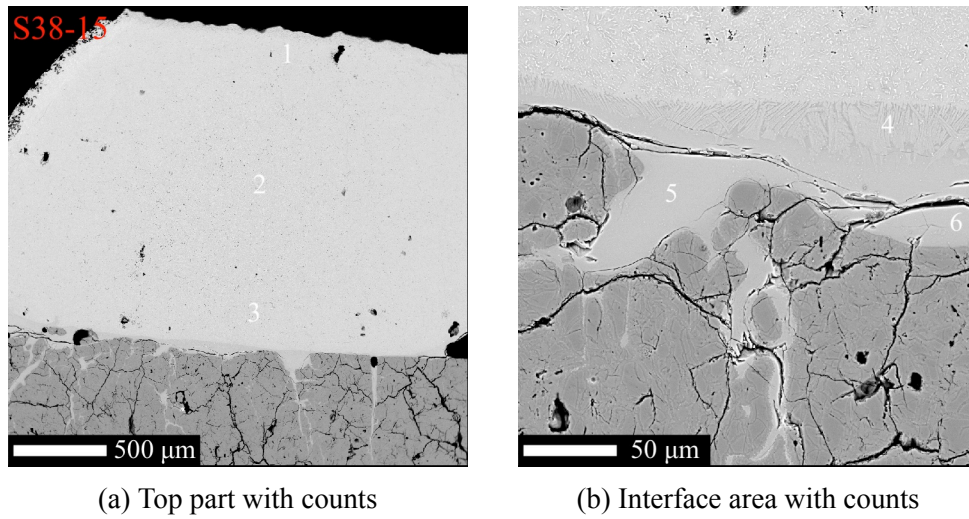
**S38-15: 58.7 mg, 15 min holding time**

Figure 4.12: Images of Sample 38-20-42 (58.7 mg) after 15 min holding time, retrieved from the EPMA analysis with 40x and 400x magnification. The scale bars are 500  $\mu\text{m}$  50  $\mu\text{m}$ .

Table 4.6: The chemical compositions for Sample 38-20-42 (58.7 mg) after 15 min, retrieved from the chemical analysis in EPMA. Here, each analysis number refers to the points in Figure 4.12.

Wet sample	Analysis	SiO <sub>2</sub>	CaO	Al <sub>2</sub> O <sub>3</sub>	CaO/Al <sub>2</sub> O <sub>3</sub>
		[wt. %]			
S38-15	1	39.2	42.3	19.9	0.47
	2	39.2	41.7	20.0	0.48
	3	39.5	41.5	19.8	0.48
	4	57.3	15.1	28.6	0.53
	5	65.1	12.3	23.5	0.52
	6	62.1	13.3	25.8	0.51

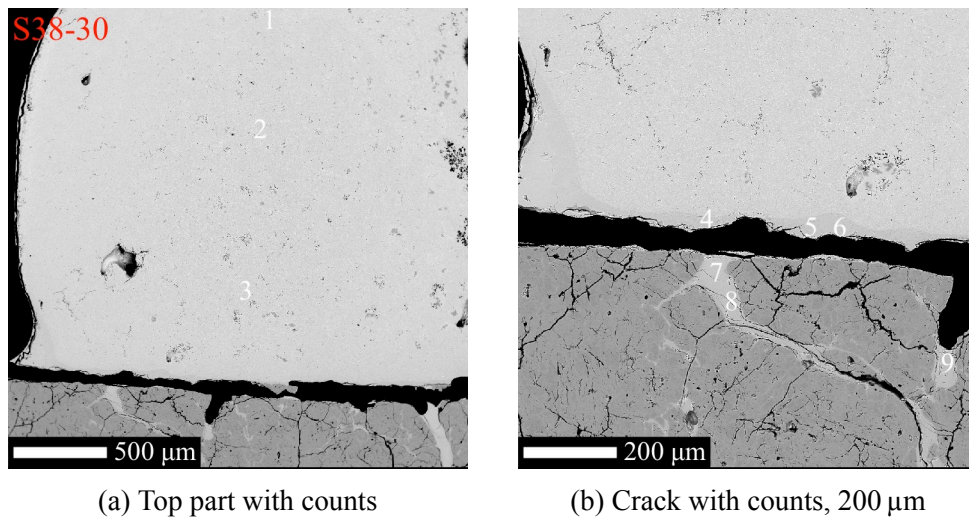
**S38-30: 52.9 mg, 30 min holding time**

Figure 4.13: Images of Sample 38-20-42 (52.9 mg) after 30 min holding time, retrieved from the EPMA analysis with 40x and 100x magnification. The scale bars are 500 μm and 200 μm.

Table 4.7: The chemical compositions for Sample 38-20-42 (52.9 mg) after 30 min, retrieved from the chemical analysis in EPMA. Here, each analysis number refers to the points in Figure 4.13.

Wet sample	Analysis	SiO <sub>2</sub>	CaO	Al <sub>2</sub> O <sub>3</sub>	CaO/Al <sub>2</sub> O <sub>3</sub>
		[wt. %]			
S38-30	1	40.1	38.8	20.9	0.54
	2	38.4	42.0	19.6	0.47
	3	38.7	41.5	19.9	0.48
	4	56.8	14.9	28.4	0.52
	5	59.0	14.1	27.6	0.51
	6	58.8	13.8	27.7	0.50
	7	65.4	12.4	22.2	0.56
	8	70.5	10.8	19.0	0.57
	9	73.3	9.8	17.2	0.57

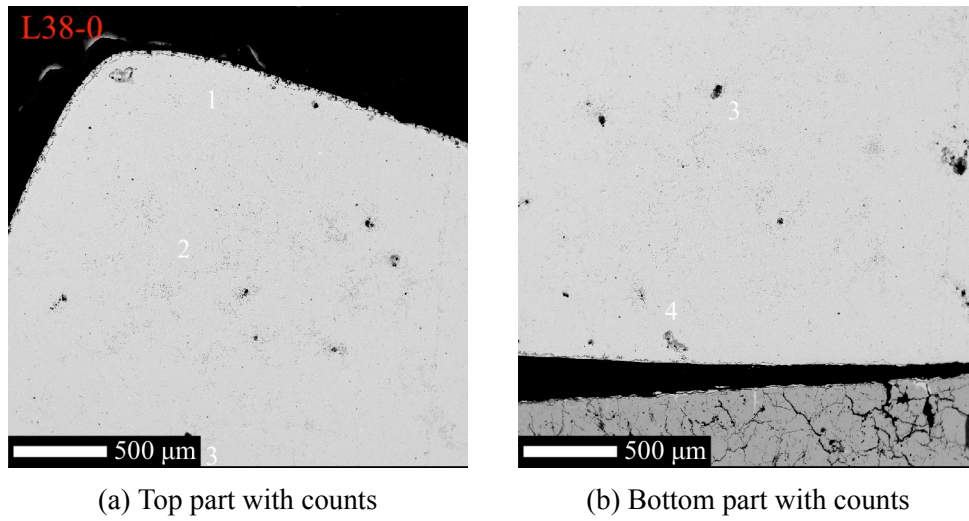
**L38-0: 171.9 mg, 0 min holding time**

Figure 4.14: Images of Sample 38-20-42 (171.9 mg) after 0 min holding time, retrieved from the EPMA analysis with 40x magnification.

Table 4.8: The chemical compositions for Sample 38-20-42 (171.9 mg) after 0 min, retrieved from the chemical analysis in EPMA. Here, each analysis number refers to the points in Figure 4.14.

Wet sample	Analysis	SiO <sub>2</sub>	CaO	Al <sub>2</sub> O <sub>3</sub>	CaO/Al <sub>2</sub> O <sub>3</sub>
		[wt. %]			
L38-0	1	38.6	41.1	19.4	0.47
	2	38.5	40.8	20.3	0.50
	3	37.7	40.7	20.4	0.50
	4	36.3	43.0	19.9	0.46

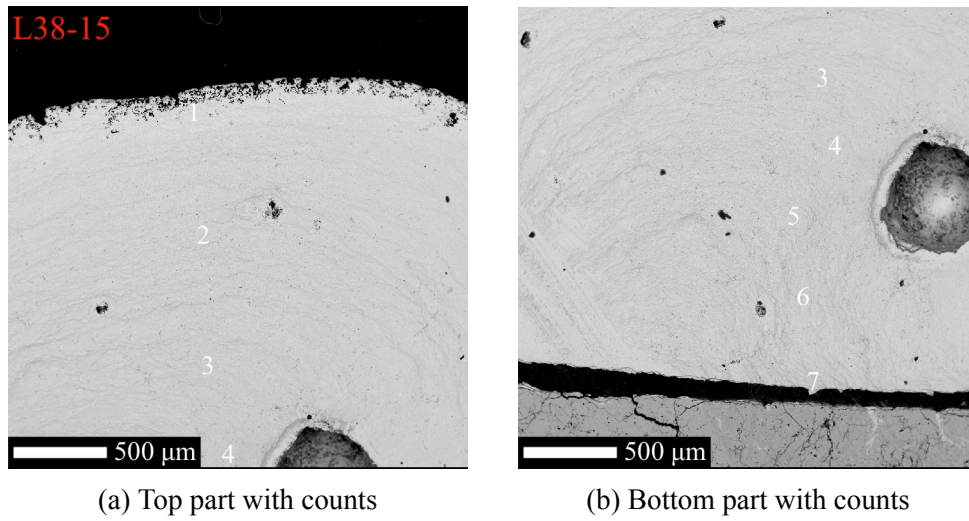
**L38-15: 147.1 mg, 15 min holding time**

Figure 4.15: Images of Sample 38-20-42 (147.1 mg) after 15 min holding time, retrieved from the EPMA analysis with 40x magnification.

Table 4.9: The chemical compositions for Sample 38-20-42 (147.1 mg) after 15 min, retrieved from the chemical analysis in EPMA. Here, each analysis number refers to the points in Figure 4.15.

Wet sample	Analysis	SiO <sub>2</sub>	CaO	Al <sub>2</sub> O <sub>3</sub>	CaO/Al <sub>2</sub> O <sub>3</sub>
		[wt. %]			
L38-15	1	39.2	38.8	21.3	0.55
	2	42.3	40.3	19.4	0.48
	3	37.1	40.1	20.0	0.50
	4	43.3	40.0	18.9	0.47
	5	41.3	39.0	19.0	0.49
	6	41.1	39.7	19.0	0.48
	7	39.8	40.6	19.4	0.48

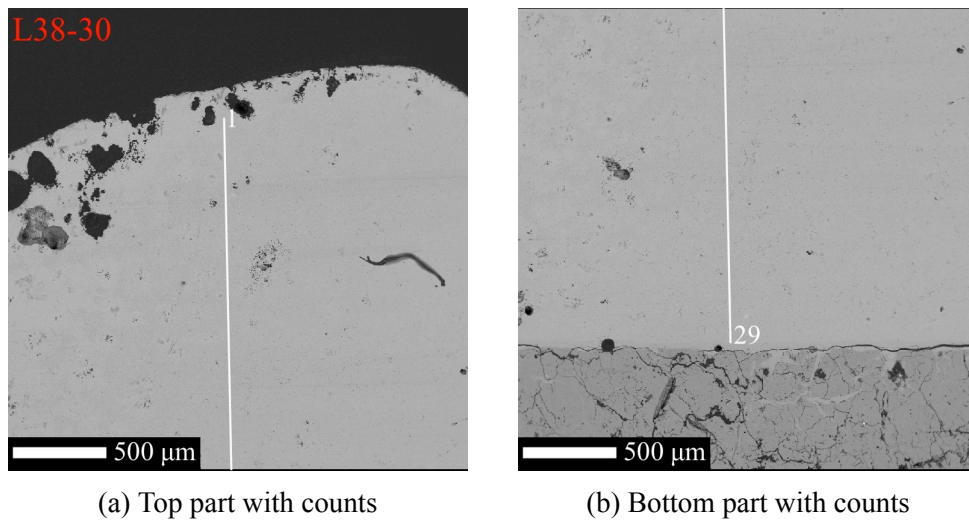
**L38-30: 162.9 mg, 30 min holding time**

Figure 4.16: Images of Sample 38-20-42 (162.9 mg) after 30 min holding time, retrieved from the EPMA analysis with 40x magnification.

Table 4.10: The chemical compositions for Sample 38-20-42 (162.9 mg) after 30 min, retrieved from the chemical analysis in EPMA. Here, each analysis number refers to the points in Figure 4.16.

Wet sample	Analysis	SiO <sub>2</sub>	CaO	Al <sub>2</sub> O <sub>3</sub>	CaO/Al <sub>2</sub> O <sub>3</sub>
		[wt. %]			
L38-30	1	37.4	40.0	22.2	0.55
	2	38.0	39.8	21.5	0.54
	3	37.2	41.4	21.1	0.51
	4	40.0	39.7	20.2	0.51
	5	39.2	40.6	19.8	0.49
	6	38.3	42.6	19.6	0.46
	7	40.0	39.8	20.1	0.51
	8	38.2	40.9	20.9	0.51
	9	36.4	44.0	19.6	0.44
	10	38.3	41.7	19.9	0.48
	11	37.7	41.9	20.2	0.48
	12	39.9	40.1	19.8	0.49
	13	39.1	40.0	20.7	0.52
	14	37.7	41.7	19.8	0.47
	15	38.7	40.7	19.0	0.47
	16	39.0	40.1	19.4	0.48
	17	37.5	42.3	19.5	0.46
	18	37.5	42.2	20.3	0.48
	19	38.6	41.2	19.8	0.48
	20	37.8	40.9	20.3	0.50
	21	37.9	22.3	11.7	0.52
	22	38.3	41.0	20.4	0.50
	23	37.6	43.2	19.3	0.45
	24	38.6	40.3	20.3	0.50
	25	39.2	40.0	19.8	0.50
	26	39.5	41.5	19.1	0.46
	27	40.2	39.9	19.2	0.48
	28	38.4	41.0	20.0	0.49
	29	39.3	41.4	19.6	0.47

It is observed that the slags did not liquefy during heating, as the liquidus temperature for this slag composition is below the experimental temperature of 1500 °C. However, it is seen that the slags did soften by examining the smooth edges around the slag pieces. As seen in the figures, some of the slags detached from the substrates post-heating. No significant difference was observed between small-sized and large-sized slags.

In some of the parallels, a glassy slag structure was observed which is classified with a darker shade of grey compared to the solid slag bulk. Here, the presence of glassy slag

is seen between the bulk slag and quartz substrate, indicating liquefaction around the interface area. This was occurring in Figures 4.12, 4.13 and 4.16.

Some minor cracks were seen in the quartz substrates, but no major cracks were present. In Figures 4.12 and 4.13, it is observed that the cracks have been penetrated with liquid slag.

The chemical analyses performed on the slags showed no significant changes in chemical composition in the slag bulk, meaning the slags had a similar composition to the master slag and no chemical interactions with the quartz were occurring. Little to no difference was observed when comparing the small-sized parallels to the large-sized parallels. In general, the silica content was around  $38 \pm 2$  wt%. However, the slags present in cracks and close to the interface area showed a significant increase compared to the slag bulk. As this slag had a silica content of 20 wt% higher than the bulk, they indicate an increase in  $\text{SiO}_2$  such that chemical reactions have occurred with the substrate.

The  $\text{CaO}/\text{Al}_2\text{O}_3$  ratio was close to constant for all parallels, meaning there were no chemical reactions occurring with alumina during the experiments.

#### 4.2.2 Sample 50 % $\text{SiO}_2$ – 21 % $\text{CaO}$ – 29 % $\text{Al}_2\text{O}_3$

The BSE images and their corresponding tables with chemical analysis are presented in Figures 4.17 to 4.19 and Tables 4.12 to 4.14 for parallels at 0 min, 15 min and 30 min holding time, using a small-sized slag. Figures 4.20 to 4.22 and Tables 4.15 to 4.17 present the parallels using large-sized slag. The numbers and the lines correspond to the line analysis done in the sample. The tables show the chemical composition in each point with their respective  $\text{CaO}/\text{Al}_2\text{O}_3$  ratio. To get an overview, Table 4.11 shows which figure and table belong to the respective sample.

Table 4.11: Overview of the corresponding BSE images and chemical analyses for each parallel performed with Sample 50-21-29.

Sample	Figure	Table
S50-0	4.17	4.12
S50-15	4.18	4.13
S50-30	4.19	4.14
L50-0	4.20	4.15
L50-15	4.21	4.16
L50-30	4.22	4.17

**S50-0: 58.5 mg, 0 min holding time**

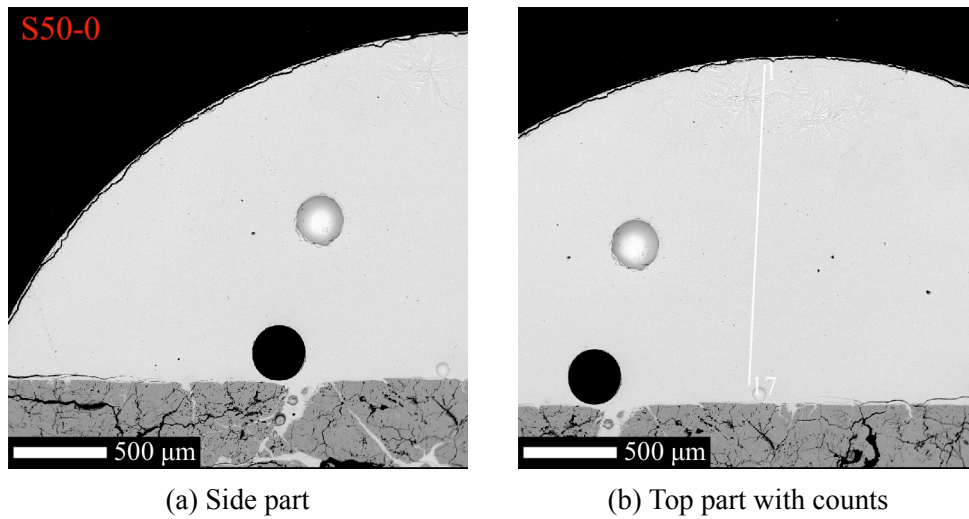


Figure 4.17: Images of Sample 50-21-29 (58.5 mg) after 0 min holding time, retrieved from the EPMA analysis with 40x magnification.

Table 4.12: The chemical compositions for Sample 50-21-29 (58.5 mg) after 0 min, retrieved from the chemical analysis in EPMA. Here, each analysis number refers to the points in Figure 4.17.

Wet sample	Analysis	SiO <sub>2</sub>	CaO	Al <sub>2</sub> O <sub>3</sub>	CaO/Al <sub>2</sub> O <sub>3</sub>
		[wt. %]			
S50-0	1	51.6	26.8	21.9	0.82
	2	50.8	27.7	22.1	0.80
	3	50.5	28.7	21.3	0.74
	4	52.1	25.8	22.7	0.88
	5	51.2	26.5	21.9	0.83
	6	51.9	27.4	21.4	0.78
	7	51.3	26.6	21.9	0.82
	8	51.6	26.7	21.8	0.82
	9	51.6	26.7	22.2	0.83
	10	51.8	26.3	21.7	0.82
	11	51.6	27.2	21.6	0.79
	12	51.8	26.7	21.5	0.80
	13	52.1	27.4	21.4	0.78
	14	51.9	26.3	22.1	0.84
	15	51.5	27.0	21.6	0.80
	16	48.0	23.0	20.8	0.90
	17	52.2	26.4	21.8	0.82

### S50-15: 48.0 mg, 15 min holding time

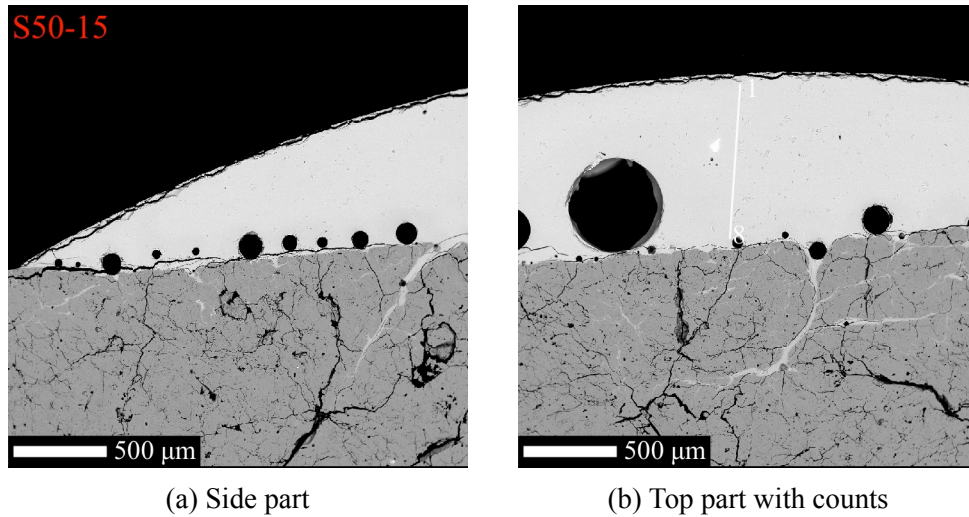


Figure 4.18: Images of Sample 50-21-29 (48.0 mg) after 15 min holding time, retrieved from the EPMA analysis with 40x magnification.

Table 4.13: The chemical compositions for Sample 50-21-29 (48.0 mg) after 15 min, retrieved from the chemical analysis in EPMA. Here, each analysis number refers to the points in Figure 4.18.

Wet sample	Analysis	SiO <sub>2</sub>	CaO	Al <sub>2</sub> O <sub>3</sub>	CaO/Al <sub>2</sub> O <sub>3</sub>
		[wt. %]			
S50-15	1	56.3	23.8	19.9	0.84
	2	56.4	24.0	20.0	0.83
	3	54.9	24.7	20.5	0.83
	4	53.7	25.1	20.1	0.80
	5	54.3	25.1	20.2	0.81
	6	55.6	24.4	20.2	0.83
	7	56.4	24.0	20.0	0.83
	8	59.0	22.1	19.1	0.86

### S50-30: 50.9 mg, 30 min holding time

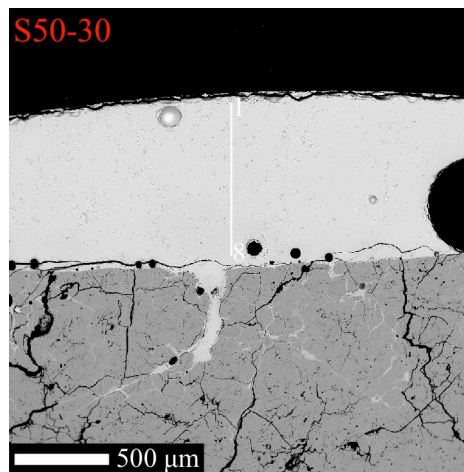


Figure 4.19: Image of Sample 50-21-29 (50.9 mg) after 30 min holding time, retrieved from the EPMA analysis with 40x magnification.

Table 4.14: The chemical compositions for Sample 50-21-29 (50.9 mg) after 30 min, retrieved from the chemical analysis in EPMA. Here, each analysis number refers to the points in Figure 4.19.

Wet sample	Analysis	SiO <sub>2</sub>	CaO	Al <sub>2</sub> O <sub>3</sub>	CaO/Al <sub>2</sub> O <sub>3</sub>
		[wt. %]			
S50-30	1	60.6	22.1	18.5	0.84
	2	60.8	22.0	18.7	0.85
	3	61.1	21.9	18.4	0.84
	4	58.9	23.0	19.0	0.82
	5	59.1	22.9	18.9	0.83
	6	62.9	20.5	17.4	0.85
	7	62.5	20.9	17.6	0.84
	8	62.5	20.9	17.8	0.85

### L50-0: 142.7 mg, 0 min holding time

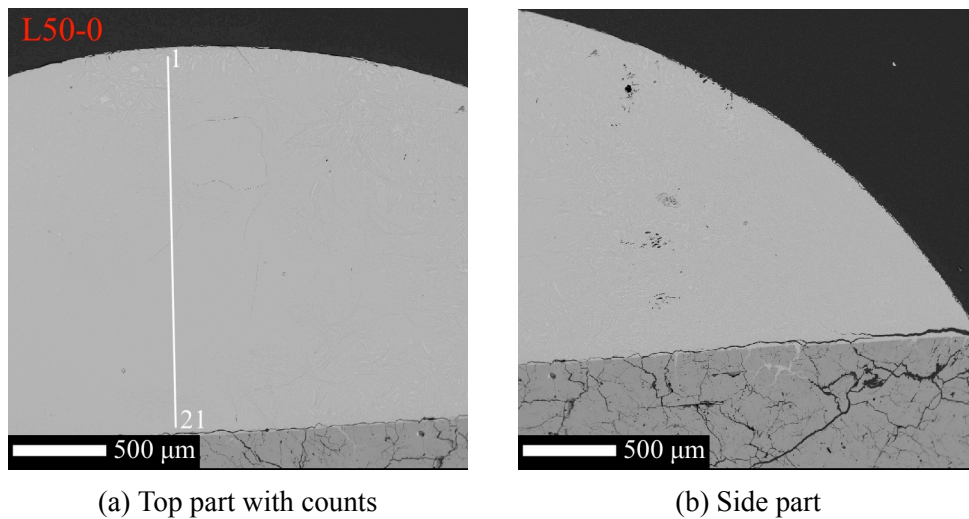


Figure 4.20: Images of Sample 50-21-29 (142.7 mg) after 0 min holding time, retrieved from the EPMA analysis with 40x magnification.

Table 4.15: The chemical compositions for Sample 50-21-29 (142.7 mg) after 0 min, retrieved from the chemical analysis in EPMA. Here, each analysis number refers to the points in Figure 4.20.

Wet sample	Analysis	SiO <sub>2</sub>	CaO	Al <sub>2</sub> O <sub>3</sub>	CaO/Al <sub>2</sub> O <sub>3</sub>
		[wt. %]			
L50-0	1	52.3	25.0	23.2	0.93
	2	51.8	25.6	22.6	0.89
	3	52.0	25.4	23.1	0.91
	4	51.7	27.1	21.8	0.81
	5	51.4	27.1	21.7	0.8
	6	51.6	27.1	22.0	0.81
	7	51.6	27.0	22.1	0.82
	8	50.7	26.3	21.5	0.82
	9	51.5	27.1	21.7	0.8
	10	51.5	26.9	22.0	0.82
	11	51.9	26.6	21.9	0.82
	12	52.0	26.7	21.6	0.81
	13	52.2	26.4	21.7	0.82
	14	52.3	26.5	21.6	0.82
	15	51.8	26.4	21.7	0.82
	16	51.9	26.8	21.8	0.81
	17	51.8	26.7	21.5	0.81
	18	52.1	26.5	21.5	0.81
	19	52.0	27.1	21.4	0.79
	20	52.3	26.9	21.5	0.80
	21	53.0	26.3	21.0	0.80

### L50-15: 161.8 mg, 15 min holding time

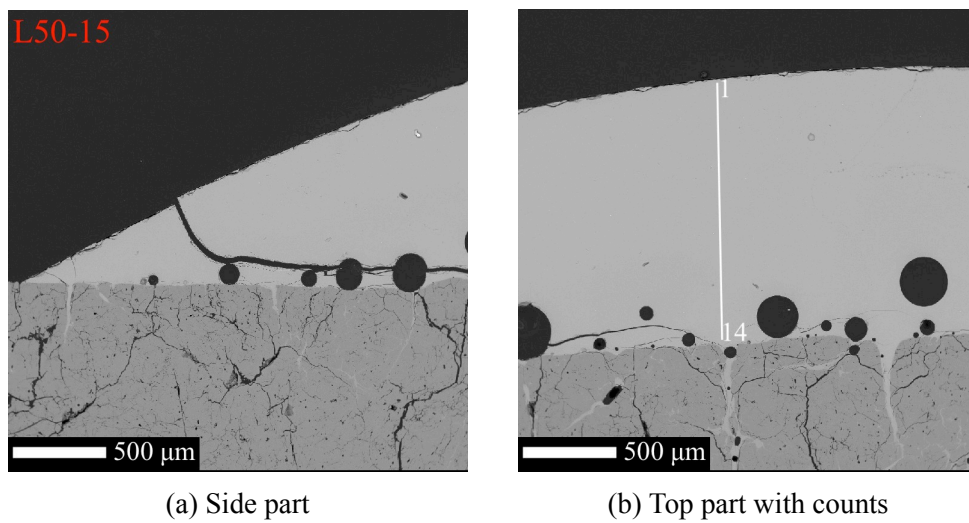


Figure 4.21: Images of Sample 50-21-29 (161.8 mg) after 15 min holding time, retrieved from the EPMA analysis with 40x magnification.

Table 4.16: The chemical compositions for Sample 50-21-29 (161.8 mg) after 15 min, retrieved from the chemical analysis in EPMA. Here, each analysis number refers to the points in Figure 4.21.

Wet sample	Analysis	SiO <sub>2</sub>	CaO	Al <sub>2</sub> O <sub>3</sub>	CaO/Al <sub>2</sub> O <sub>3</sub>
		[wt. %]			
L50-15	1	55.9	23.8	20.3	0.85
	2	55.6	24.1	20.3	0.84
	3	56.3	24.0	20.4	0.85
	4	55.9	23.7	20.3	0.86
	5	55.6	24.6	20.5	0.83
	6	55.4	24.6	20.6	0.84
	7	55.2	24.5	20.5	0.84
	8	55.4	24.4	20.6	0.85
	9	55.2	24.6	20.6	0.84
	10	54.5	25.3	20.7	0.82
	11	54.2	25.3	20.5	0.81
	12	55.9	24.3	20.3	0.83
	13	56.3	24.1	19.7	0.82
	14	56.0	24.1	19.9	0.83

### L50-30: 149.9 mg, 30 min holding time

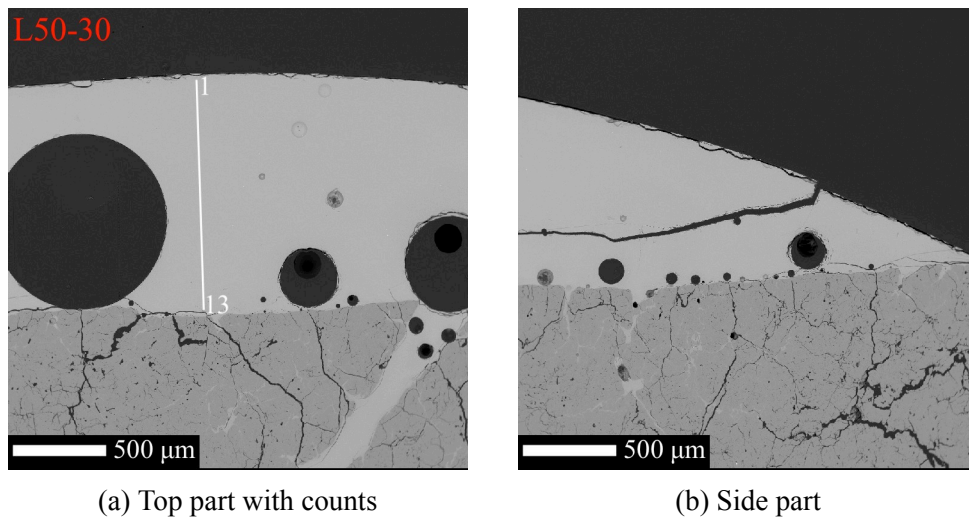


Figure 4.22: Images of Sample 50-21-29 (149.9 mg) after 30 min holding time, retrieved from the EPMA analysis with 40x magnification.

Table 4.17: The chemical compositions for Sample 50-21-29 (149.9 mg) after 30 min, retrieved from the chemical analysis in EPMA. Here, each analysis number refers to the points in Figure 4.22.

Wet sample	Analysis	SiO <sub>2</sub>	CaO	Al <sub>2</sub> O <sub>3</sub>	CaO/Al <sub>2</sub> O <sub>3</sub>
		[wt. %]			
L50-30	1	58.2	22.8	18.5	0.81
	2	58.2	23.1	18.7	0.81
	3	58.1	23.0	18.8	0.82
	4	57.1	23.4	19.6	0.84
	5	56.6	23.7	19.6	0.83
	6	56.8	23.7	19.5	0.82
	7	57.2	23.7	19.2	0.81
	8	57.5	23.3	19.1	0.82
	9	56.7	24.1	19.7	0.82
	10	56.3	24.4	19.3	0.79
	11	56.6	23.8	19.4	0.81
	12	56.6	24.1	19.4	0.80
	13	59.7	22.2	18.0	0.81

Experiments with Sample 50-21-29 resulted in good wetting conditions. It is observed that the slag was liquefied and they were wetting the quartz substrates. Qualitatively, the images show that the slags reached a greater wetting condition with increasing isothermal holding time, meaning the wetting angle was decreased. In addition, no significant difference in wetting was observed between small-sized and large-sized samples. In some of the samples, bubbles were present inside the slag bulk, as seen in Figures 4.17 to 4.19, 4.21 and 4.22. Some large cracks in the slag bulk were seen that originated from the cooling of the furnace after the experiment.

Some microstructure was observed in the top end of the slag for the two parallels with 0 min holding time, seen in Figures 4.17 and 4.20. This indicates that some of the slags was not perhaps completely in liquid phase when reaching 1500 °C. As the liquidus temperature of this slag is 1505 °C, some slag may still be in solid phase as these samples were stopped straight after reaching 1500 °C.

The intensity of crack propagation in the substrates varied, where some did not experience any cracks while other parallels had large cracks present. Minor cracks were observed in Figures 4.17 to 4.19 and 4.21, while some major cracks were found in Figures 4.19

and 4.22. The large cracks will be presented later. In general, the cracks were penetrated with liquid slag.

The chemical analyses performed on the slags showed an increase in  $\text{SiO}_2$  with increasing holding time. The two parallels held for 0 min had a similar chemical composition to the master slag, while parallels with 15 and 30 min experienced a higher silica content. In each parallel, the slag did not show a significant trend of increase in  $\text{SiO}_2$  downwards, meaning the chemical composition in the bulks was close to constant. In Table 4.12, analysis number 16 shows a total chemical composition below 100 wt.%, meaning this point is not completely accurate.

The  $\text{CaO}/\text{Al}_2\text{O}_3$  ratio was close to constant for all parallels, meaning there were no chemical reactions occurring with alumina during the experiments.

### 4.2.3 Sample 62 % $\text{SiO}_2$ – 20 % $\text{CaO}$ – 18 % $\text{Al}_2\text{O}_3$

The BSE images and their corresponding tables with chemical analysis are presented in Figures 4.23 to 4.25 and Tables 4.19 to 4.21 for parallels at 0 min, 15 min and 30 min holding time, using a small-sized slag. Figures 4.26 to 4.28 and Tables 4.22 to 4.24 present the parallels using large-sized slag. The numbers and the lines correspond to the line analysis done in the sample. The tables show the chemical composition in each point with their respective  $\text{CaO}/\text{Al}_2\text{O}_3$  ratio. To get an overview, Table 4.18 shows which figure and table belong to the respective sample.

Table 4.18: Overview of the corresponding BSE images and chemical analyses for each parallel performed with Sample 62-20-18.

Sample	Figure	Table
S62-0	4.23	4.19
S62-15	4.24	4.20
S62-30	4.25	4.21
L62-0	4.26	4.22
L62-15	4.27	4.23
L62-30	4.28	4.24

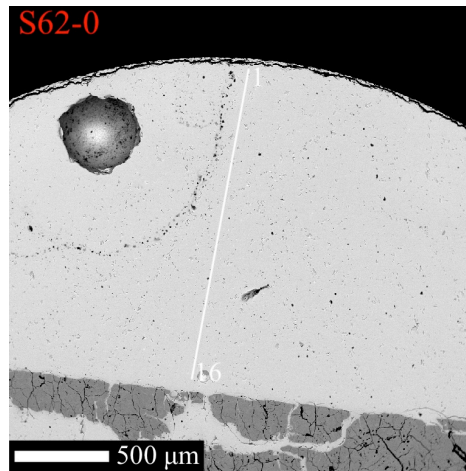
**S62-0: 55.6 mg, 0 min holding time**

Figure 4.23: Image of Sample 62-20-18 (55.6 mg) after 0 min holding time, retrieved from the EPMA analysis with 40x magnification.

Table 4.19: The chemical compositions for Sample 62-20-18 (55.6 mg) after 0 min, retrieved from the chemical analysis in EPMA. Here, each analysis number refers to the points in Figure 4.23.

Wet sample	Analysis	SiO <sub>2</sub>	CaO	Al <sub>2</sub> O <sub>3</sub>	CaO/Al <sub>2</sub> O <sub>3</sub>
		[wt. %]			
S62-0	1	62.9	17.7	19.9	1.12
	2	63.3	17.5	19.6	1.12
	3	63.4	17.7	19.8	1.12
	4	62.9	17.6	19.8	1.12
	5	63.6	17.5	19.6	1.12
	6	63.2	17.7	19.6	1.11
	7	62.4	17.7	19.5	1.10
	8	62.6	17.6	19.9	1.13
	9	63.4	17.4	19.6	1.13
	10	62.1	17.6	19.6	1.11
	11	63.1	17.5	19.6	1.11
	12	62.9	17.5	19.7	1.13
	13	63.2	17.0	19.7	1.16
	14	63.0	17.7	19.9	1.12
	15	63.3	17.5	19.9	1.14
	16	62.9	17.6	20.0	1.14

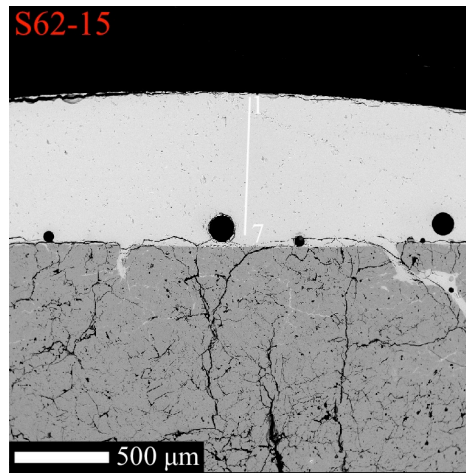
**S62-15: 53.5 mg, 15 min holding time**

Figure 4.24: Image of Sample 62-20-18 (53.5 mg) after 15 min holding time, retrieved from the EPMA analysis with 40x magnification.

Table 4.20: The chemical compositions for Sample 62-20-18 (53.5 mg) after 15 min, retrieved from the chemical analysis in EPMA. Here, each analysis number refers to the points in Figure 4.24.

Wet sample	Analysis	SiO <sub>2</sub>	CaO	Al <sub>2</sub> O <sub>3</sub>	CaO/Al <sub>2</sub> O <sub>3</sub>
		[wt. %]			
S62-15	1	62.8	17.3	19.4	1.12
	2	63.7	17.2	19.5	1.14
	3	63.9	16.9	19.4	1.14
	4	63.3	17.3	19.4	1.12
	5	63.3	17.4	19.5	1.12
	6	63.3	17.5	19.7	1.13
	7	63.2	17.1	19.4	1.14

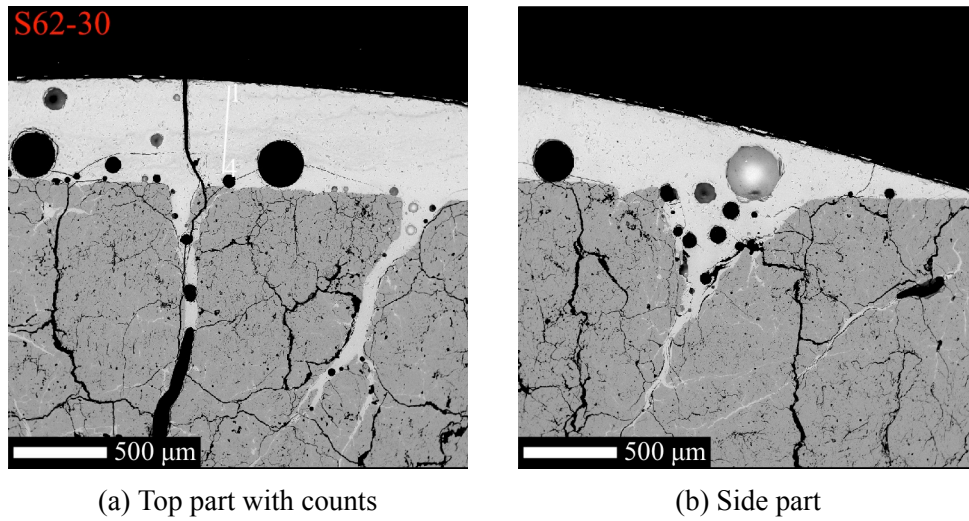
**S62-30: 57.6 mg, 30 min holding time**

Figure 4.25: Images of Sample 62-20-18 (57.6 mg) after 30 min holding time, retrieved from the EPMA analysis with 40x magnification.

Table 4.21: The chemical compositions for Sample 62-20-18 (57.6 mg) after 30 min, retrieved from the chemical analysis in EPMA. Here, each analysis number refers to the points in Figure 4.25.

Wet sample	Analysis	SiO <sub>2</sub>	CaO	Al <sub>2</sub> O <sub>3</sub>	CaO/Al <sub>2</sub> O <sub>3</sub>
		[wt. %]			
S62-30	1	65.0	16.7	19.2	1.15
	2	64.8	15.9	18.9	1.19
	3	65.3	15.6	18.5	1.19
	4	65.2	16.3	18.4	1.13

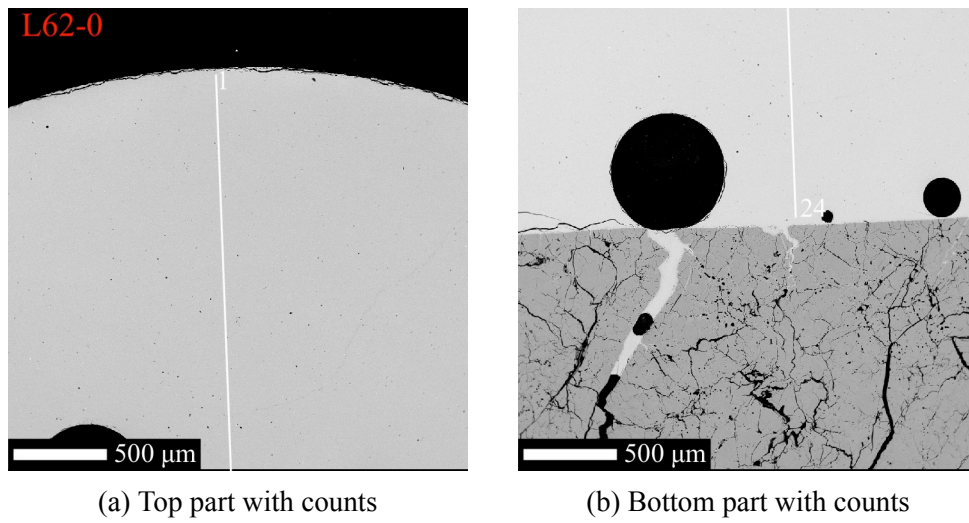
**L62-0: 146.1 mg, 0 min holding time**

Figure 4.26: Images of Sample 62-20-18 (146.1 mg) after 0 min holding time, retrieved from the EPMA analysis with 40x magnification.

Table 4.22: The chemical compositions for Sample 62-20-18 (146.1 mg) after 0 min, retrieved from the chemical analysis in EPMA. Here, each analysis number refers to the points in Figure 4.26.

Wet sample	Analysis	SiO <sub>2</sub>	CaO	Al <sub>2</sub> O <sub>3</sub>	CaO/Al <sub>2</sub> O <sub>3</sub>
		[wt. %]			
	1	60.2	17.2	20.7	1.21
	2	62.1	17.2	20.0	1.17
	3	62.6	17.3	19.6	1.13
	4	62.5	17.3	19.5	1.13
	5	62.2	17.3	19.6	1.13
	6	62.4	17.1	19.5	1.14
	7	62.2	17.2	19.9	1.16
	8	62.7	17.2	19.8	1.15
	9	62.3	17.0	19.4	1.14
	10	62.1	17.4	20.1	1.16
	11	62.4	17.5	19.8	1.14
L62-0	12	62.6	17.4	19.9	1.14
	13	61.7	17.3	20.0	1.16
	14	62.6	17.1	19.7	1.15
	15	62.2	17.3	19.8	1.14
	16	62.2	17.3	19.9	1.15
	17	62.1	17.2	20.1	1.17
	18	62.3	17.1	19.9	1.16
	19	62.3	17.1	19.8	1.16
	20	62.5	17.1	19.8	1.16
	21	62.3	17.2	19.7	1.14
	22	61.9	17.4	19.9	1.14
	23	62.8	16.8	19.5	1.16
	24	61.6	17.2	19.4	1.13

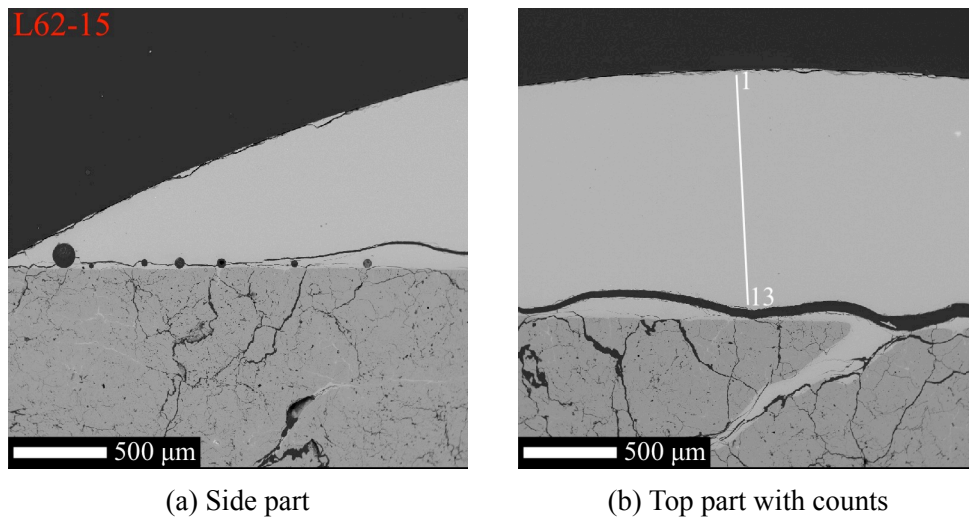
**L62-15: 144.4 mg, 15 min holding time**

Figure 4.27: Images of Sample 62-20-18 (144.4 mg) after 15 min holding time, retrieved from the EPMA analysis with 40x magnification.

Table 4.23: The chemical compositions for Sample 62-20-18 (144.4 mg) after 15 min, retrieved from the chemical analysis in EPMA. Here, each analysis number refers to the points in Figure 4.27.

Wet sample	Analysis	SiO <sub>2</sub>	CaO	Al <sub>2</sub> O <sub>3</sub>	CaO/Al <sub>2</sub> O <sub>3</sub>
		[wt. %]			
L62-15	1	62.1	17.5	19.9	1.14
	2	62.3	17.6	20.0	1.14
	3	62.2	17.6	19.8	1.13
	4	62.2	17.5	20.0	1.14
	5	62.0	17.7	19.9	1.13
	6	62.0	17.7	20.1	1.14
	7	62.3	17.6	20.0	1.14
	8	62.4	17.7	20.3	1.15
	9	61.9	17.6	19.9	1.13
	10	62.1	17.8	20.0	1.12
	11	62.5	17.8	19.6	1.10
	12	62.7	17.6	19.4	1.10
	13	68.2	12.2	14.3	1.17

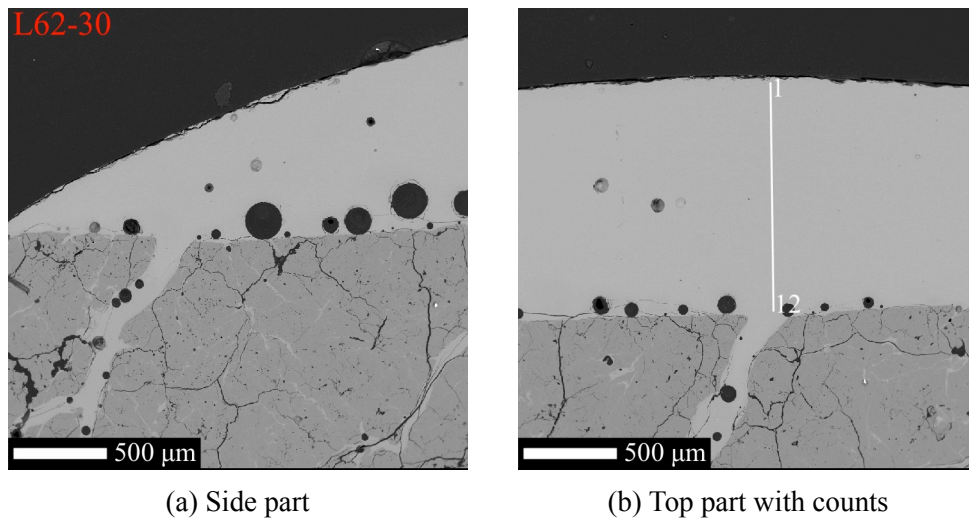
**L62-30: 163.5 mg, 30 min holding time**

Figure 4.28: Images of Sample 62-20-18 (163.5 mg) after 30 min holding time, retrieved from the EPMA analysis with 40x magnification.

Table 4.24: The chemical compositions for Sample 62-20-18 (163.5 mg) after 30 min, retrieved from the chemical analysis in EPMA. Here, each analysis number refers to the points in Figure 4.28.

Wet sample	Analysis	SiO <sub>2</sub>	CaO	Al <sub>2</sub> O <sub>3</sub>	CaO/Al <sub>2</sub> O <sub>3</sub>
		[wt. %]			
L62-30	1	63.0	17.3	19.9	1.15
	2	63.0	17.5	19.8	1.13
	3	63.2	17.3	19.4	1.12
	4	63.2	17.0	19.8	1.16
	5	63.4	17.1	19.8	1.15
	6	63.1	17.1	19.9	1.16
	7	63.2	17.2	19.8	1.15
	8	63.1	17.4	19.7	1.14
	9	62.9	17.2	19.9	1.16
	10	62.9	17.1	19.9	1.16
	11	63.0	17.2	19.9	1.16
	12	63.1	17.4	19.7	1.13

Experiments with Sample 62-20-18 resulted in good wetting conditions. It is observed that the slag was liquefied and they were wetting the quartz substrates. Qualitatively, the images show that the slags reached a greater wetting condition with increasing isothermal holding time, meaning the wetting angle was decreased. In addition, no significant difference in wetting was observed between small-sized and large-sized samples. In all of

the samples, bubbles were present inside the slag bulk. Large cracks in the slag bulk were seen that originated from the cooling of the furnace after the experiment. Some dirt on top of the slag can be seen in Figure 4.23, originating from sample preparation.

The intensity of crack propagation in the substrates varied, where some parallels only experienced minor cracks while other parallels had large cracks present. Minor cracks were observed in Figures 4.23 to 4.28, while some major cracks were found in Figures 4.23 to 4.25, 4.27 and 4.28. The large cracks will be presented later. In general, the cracks were penetrated with liquid slag.

The chemical analyses performed on the slags showed an increase in  $\text{SiO}_2$  with increasing holding time as the samples with 0 min holding time had a lower amount of  $\text{SiO}_2$  than samples with 30 min holding time. The two parallels held for 0 min had a similar chemical composition to the master slag, while parallels with 15 and 30 min experienced a higher silica content. In each parallel, the slag did not show a significant trend of increase in  $\text{SiO}_2$  downwards, meaning the chemical composition in the bulks was close to constant. In Table 4.23, analysis number 13 shows a total chemical composition below 100 wt.% and a higher silica content compared to the rest of the slag, meaning this point is not completely accurate.

The  $\text{CaO}/\text{Al}_2\text{O}_3$  ratio was close to constant for all parallels, meaning there were no chemical reactions occurring with alumina during the experiments.

### **4.3 Chemical analysis of cracks**

Some of the samples in Section 4.2 contained slag that had descended in the substrate cracks. This section presents the chemical analyses of the slags located in cracks. The BSE images and their corresponding tables with chemical analysis are presented in Figures 4.29 and 4.30 and Tables 4.26 and 4.27 for the cracks found in parallels with Sample 50-21-29. Similarly, Figures 4.31 to 4.35 and Tables 4.28 to 4.32 show the BSE images

and the chemical analyses for parallels with Sample 62-20-18. The numbers and the lines correspond to the line analysis done in the sample. The tables show the chemical composition in each point with their respective CaO/Al<sub>2</sub>O<sub>3</sub> ratio. To get an overview, Table 4.25 shows which figure and table belong to the respective sample.

Table 4.25: Overview of the corresponding BSE images and chemical analysis for each parallel with cracks.

Sample	Figure	Table
S50-30	4.29	4.26
L50-30	4.30	4.27
S62-0	4.31	4.28
S62-15	4.34	4.29
LS62-30	4.35	4.30
L62-15	4.34	4.31
L62-30	4.35	4.32

#### S50-30: 50.9 mg, 30 min holding time

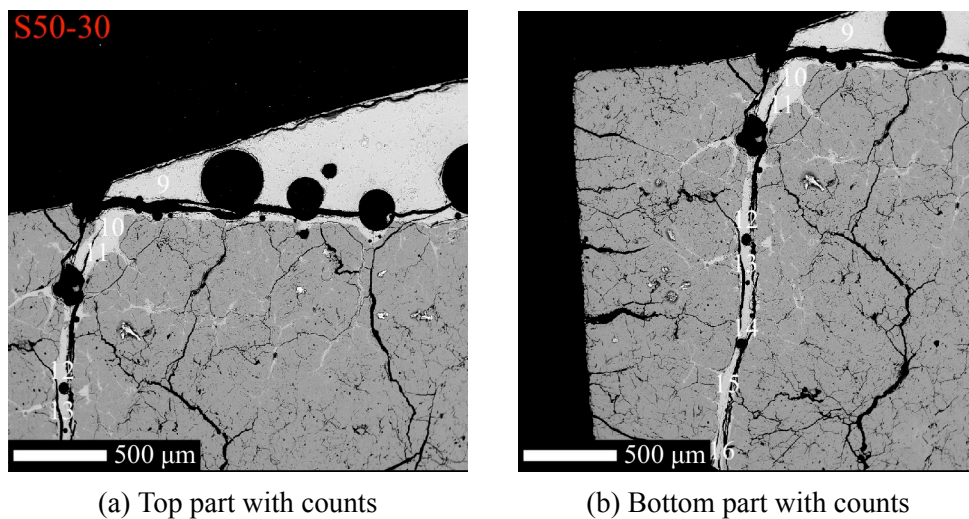


Figure 4.29: Images of a crack in Sample 50-21-29 (50.9 mg) after 30 min holding time, retrieved from the EPMA analysis with 40x magnification.

Table 4.26: Chemical composition of slag present in cracks in Sample 50-21-29 (50.9 mg) after 30 min, retrieved from the chemical analysis in EPMA. Here, each analysis number refers to the points in Figure 4.29.

Wet sample	Analysis	SiO <sub>2</sub>	CaO	Al <sub>2</sub> O <sub>3</sub>	CaO/Al <sub>2</sub> O <sub>3</sub>
		[wt. %]			
S50-30: Crack	9	63.5	17.2	20.9	0.82
	10	62.1	17.5	21.7	0.81
	11	63.6	16.8	20.7	0.81
	12	66.6	15.5	18.9	0.82
	13	68.7	14.4	17.6	0.82
	14	70.6	13.3	16.6	0.80
	15	69.4	13.9	17.6	0.79
	16	70.2	13.8	16.9	0.82

### L50-30: 149.9 mg, 30 min holding time

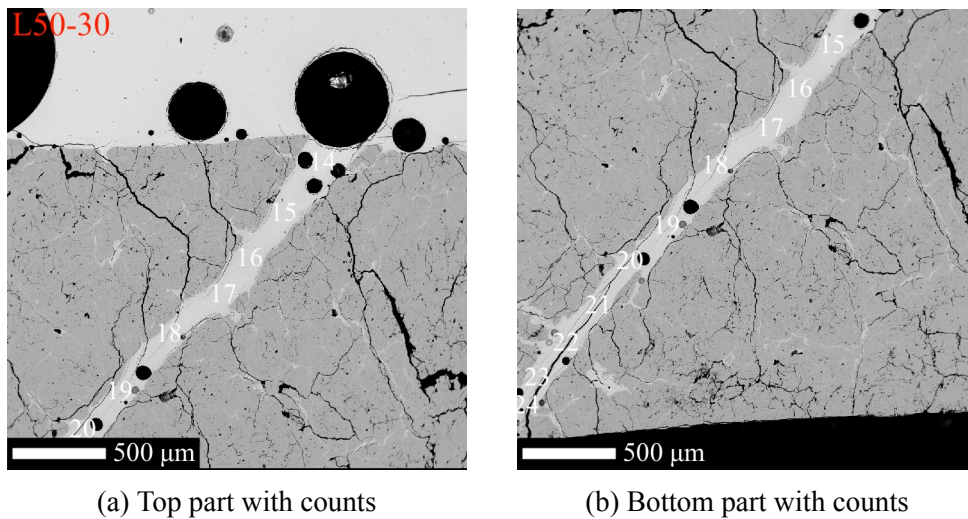


Figure 4.30: Images of a crack in Sample 50-21-29 (149.9 mg) after 30 min holding time, retrieved from the EPMA analysis with 40x magnification.

Table 4.27: Chemical composition of slag present in cracks in Sample 50-21-29 (149.9 mg) after 30 min, retrieved from the chemical analysis in EPMA. Here, each analysis number refers to the points in Figure 4.30.

Wet sample	Analysis	SiO <sub>2</sub>	CaO	Al <sub>2</sub> O <sub>3</sub>	CaO/Al <sub>2</sub> O <sub>3</sub>
		[wt. %]			
L50-30: Crack	14	56.2	18.8	24.5	0.76
	15	61.4	16.9	21.4	0.79
	16	66.5	15.0	18.1	0.83
	17	64.4	15.5	19.6	0.79
	18	66.0	15.2	18.6	0.82
	19	67.4	14.3	17.6	0.81
	20	67.8	14.1	17.7	0.80
	21	68.6	13.9	17.2	0.81
	22	68.9	13.5	16.8	0.80
	23	68.4	13.8	17.5	0.79
	24	67.2	14.1	18.3	0.77

### S62-0: 55.6 mg, 0 min holding time

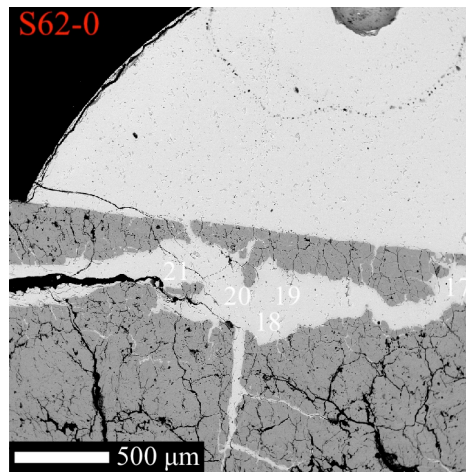


Figure 4.31: Image of a crack in Sample 62-20-18 (55.6 mg) after 0 min holding time, retrieved from the EPMA analysis with 40x magnification.

Table 4.28: Chemical composition of slag present in cracks in Sample 62-10-18 (55.6 mg) after 0 min, retrieved from the chemical analysis in EPMA. Here, each analysis number refers to the points in Figure 4.31.

Wet sample	Analysis	SiO <sub>2</sub>	CaO	Al <sub>2</sub> O <sub>3</sub>	CaO/Al <sub>2</sub> O <sub>3</sub>
		[wt. %]			
S62-0: Crack	17	63.0	19.8	17.6	1.12
	18	63.3	19.9	17.7	1.12
	19	63.4	19.7	17.5	1.13
	20	63.6	19.8	17.3	1.14
	21	63.1	19.6	17.7	1.10

### S62-15: 53.5 mg, 15 min holding time

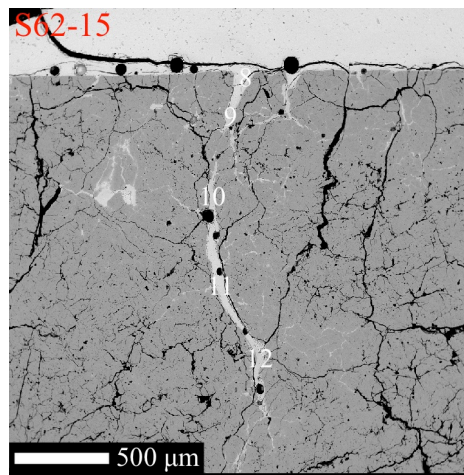


Figure 4.32: Image of a crack in Sample 62-20-18 (53.5 mg) after 15 min holding time, retrieved from the EPMA analysis with 40x magnification.

Table 4.29: Chemical composition of slag present in cracks in Sample 62-10-18 (53.5 mg) after 15 min, retrieved from the chemical analysis in EPMA. Here, each analysis number refers to the points in Figure 4.32.

Wet sample	Analysis	SiO <sub>2</sub>	CaO	Al <sub>2</sub> O <sub>3</sub>	CaO/Al <sub>2</sub> O <sub>3</sub>
		[wt. %]			
S62-15: Crack	8	65.6	18.2	16.2	1.13
	9	72.4	14.7	12.5	1.17
	10	73.4	13.9	12.1	1.15
	11	66.8	17.2	15.4	1.12
	12	72.2	14.5	12.6	1.15

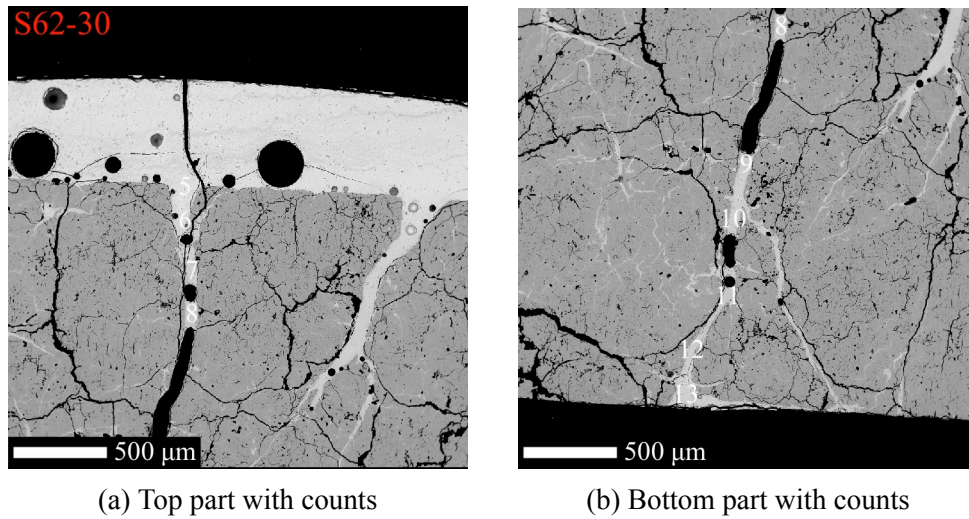
**S62-30: 57.6 mg, 30 min holding time**

Figure 4.33: Images of a crack in Sample 62-20-18 (57.6 mg) after 30 min holding time, retrieved from the EPMA analysis with 40x magnification.

Table 4.30: Chemical composition of slag present in cracks in Sample 62-10-18 (57.6 mg) after 30 min, retrieved from the chemical analysis in EPMA. Here, each analysis number refers to the points in Figure 4.33.

Wet sample	Analysis	SiO <sub>2</sub>	CaO	Al <sub>2</sub> O <sub>3</sub>	CaO/Al <sub>2</sub> O <sub>3</sub>
		[wt. %]			
S62-30: Crack	5	65.2	18.8	16.5	1.14
	6	65.1	18.2	16.7	1.09
	7	74.8	13.5	11.7	1.15
	8	76.0	12.7	11.4	1.11
	9	75.8	12.9	11.4	1.13
	10	75.5	13.1	11.7	1.12
	11	78.3	11.8	10.6	1.11
	12	74.3	13.9	12.5	1.11
	13	72.1	15.2	13.5	1.12

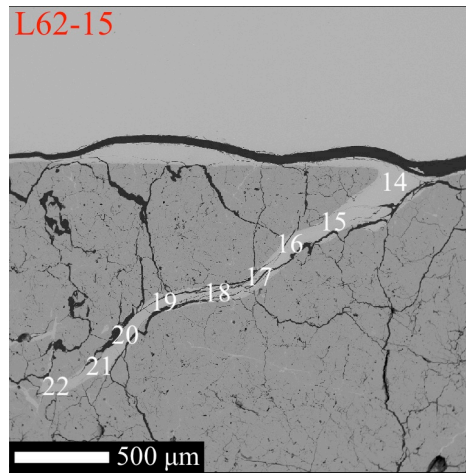
**L62-15: 144.4 mg, 15 min holding time**

Figure 4.34: Image of a crack in Sample 62-20-18 (144.4 mg) after 15 min holding time, retrieved from the EPMA analysis with 40x magnification.

Table 4.31: Chemical composition of slag present in cracks in Sample 62-10-18 (144.4 mg) after 30 min, retrieved from the chemical analysis in EPMA. Here, each analysis number refers to the points in Figure 4.34.

Wet sample	Analysis	SiO <sub>2</sub>	CaO [wt. %]	Al <sub>2</sub> O <sub>3</sub>	CaO/Al <sub>2</sub> O <sub>3</sub>
L62-15: Crack	14	62.8	19.6	17.5	1.12
	15	63.3	18.7	17.1	1.09
	16	63.5	18.7	17.1	1.09
	17	65.5	17.8	16.1	1.10
	18	70.5	15.1	13.5	1.12
	19	68.6	16.3	14.6	1.11
	20	70.6	14.7	13.2	1.12
	21	72.3	14.2	12.7	1.11
	22	74.3	13.1	11.9	1.10

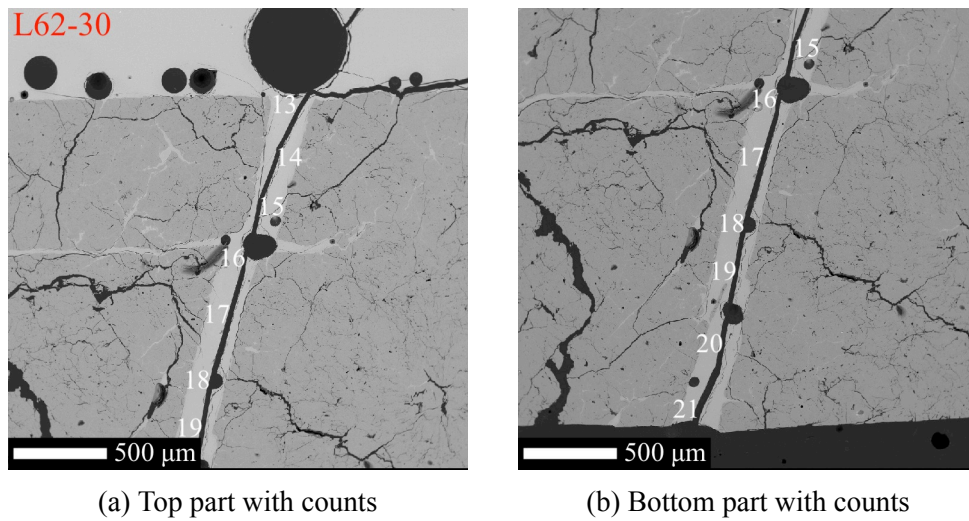
**L62-30: 163.5 mg, 30 min holding time**

Figure 4.35: Images of a crack in Sample 62-20-18 (163.5 mg) after 30 min holding time, retrieved from the EPMA analysis with 40x magnification.

Table 4.32: Chemical composition of slag present in cracks in Sample 62-10-18 (163.5 mg) after 30 min, retrieved from the chemical analysis in EPMA. Here, each analysis number refers to the points in Figure 4.35.

Wet sample	Analysis	SiO <sub>2</sub>	CaO [wt. %]	Al <sub>2</sub> O <sub>3</sub>	CaO/Al <sub>2</sub> O <sub>3</sub>
L62-30: Crack	13	63.4	19.2	17.2	1.12
	14	66.4	17.7	15.6	1.14
	15	68.6	15.6	14.1	1.10
	16	71.8	14.7	13.1	1.12
	17	67.7	16.8	15.1	1.11
	18	72.3	14.7	12.9	1.15
	19	69.6	15.7	14.4	1.10
	20	70.4	15.4	14.1	1.09
	21	71.4	14.7	13.6	1.08

It is observed that the slags have descended in the substrate cracks. The length of the crack varied, where some of the cracks had propagated down to the end of the substrate, as seen in Figures 4.30, 4.33 and 4.35. Shorter cracks was observed in Figures 4.29, 4.32 and 4.34. In Figure 4.31, a major void was seen right below the slag droplet.

The chemical analyses performed on the slags showed a significant increase in SiO<sub>2</sub> compared to the master slag compositions, indicating a higher saturation. Parallels with similar

holding times did not experience any significant differences. In addition, a higher silica content is indicated further down in the crack for each parallel, meaning a silica-rich slag is expected at the bottom. The slag in the large void in Figure 4.31 did not show any difference in the chemical composition in different positions, indicating a constant silica content. Slags in parallels with Sample 62-20-18 indicate a slightly higher increase in  $\text{SiO}_2$  compared to the parallels with Sample 50-21-29.

The  $\text{CaO}/\text{Al}_2\text{O}_3$  ratio was close to constant for all parallels, meaning no chemical reactions were occurring with alumina during the experiments.

# Chapter 5

## Discussion

This chapter addresses the results obtained from the experimental work to further understand the mechanisms and reasons to why certain phenomena occurred. Subsequently, the effect of using different slag compositions, temperatures and holding times will be investigated.

### 5.1 Wetting of slag

All of the recorded softening and liquidus temperatures for each parallel are tabulated in Table 5.1. Subsequently, the table presents the theoretical solidus and liquidus temperatures for each slag. Firstly, softening temperatures are observed to occur below their solidus temperature. As Ringdalen et al. (2016) investigated with their study, softening of the material may occur earlier as it may be influenced by the heating rate[28]. Here, parallels with Sample 50-21-29 and 62-20-18 experienced softening at 100 °C lower than the solidus temperature of 1170 °C. Moreover, Sample 38-20-42 had the highest deviance, experiencing softening at 300 °C lower than the solidus of 1385 °C.

The experimental liquidus temperatures were more similar to the theoretical liquidus temperature. Recorded liquidus for Sample 50-21-29 was only 5 °C lower than the theoretical

temperature of 1505 °C. Consequently, the recorded liquidus for Sample 62-20-18 was found to be even lower. The parallel L62-15 had an experimental temperature of 1279 °C compared to the liquidus of 1320 °C. Because of the high viscosity of Sample 62-20-18, it was difficult to determine when the slag bulk was completely in a liquid phase. One could only observe the surfaces of the bulk, making it harder to estimate the liquidus temperature of the slag compared to Sample 50-21-29 parallels which were less viscous. In addition, inconsistencies in the thermocouple may affect the projection of the internal temperature in the furnace. Nevertheless, the deviance from the theoretical liquidus is considerably small.

Table 5.1: Softening, melting, solidus and liquidus temperatures for each sample.

Sample	Experimental softening [°C]	Experimental liquidus [°C]	Solidus temperature [°C]	Liquidus temperature [°C]
S38-0	1086	-		
S38-15	1072	-		
S38-30	1083	-		
L38-0	1077	-	1385	1530
L38-15	1072	-		
L38-30	1091	-		
S50-0	1085	1499		
S50-15	1088	1498		
S50-30	1124	1489		
L50-0	1091	1500	1170	1505
L50-15	1081	1499		
L50-30	1125	1489		
S62-0	1047	1284		
S62-15	1059	1282		
S62-30	1087	1318		
L62-0	1056	1284	1170	1320
L62-15	1053	1279		
L62-30	1091	1316		

Wetting experiments performed in the sessile drop furnace resulted in similar wetting angles for parallels with the same slag composition. It was observed that wettability occurred rapidly in the beginning when liquefied, followed by a decrease in wettability rate during the holding time. In addition, samples with the high-silica slag, Sample 62-20-18, expe-

rienced a weaker rate of wetting compared to samples with lower silica content.

Parallels performed with Sample 38-20-42 did not wet the substrate as the bulk slags were in their solid phase during heating, as a result of operating below the liquidus temperature of the slag. Here, only a small curvature was observed close to the interface as a result of small amounts of slag that were liquefied.

The wetting experiments with 30 min holding time for Sample 50-21-29 and 62-20-18 are plotted in Figure 5.1. The dotted lines are experiments with large-sized slag and solid lines are with small-sized slag. It is observed that Sample 62-20-18 wet the substrate at a lower temperature due to a lower liquidus temperature. At the liquidus temperature of Sample 50-21-29, around 1500 °C, both of the slags experienced a similar wetting angle. However, parallels with Sample 62-20-18 experienced a lower wetting rate of  $-5.6^\circ/\text{min}$  from 0 min isothermal holding time to 5 min, compared to Sample 50-21-29 with  $-7.1^\circ/\text{min}$ . The rates were decreased after 5 min holding time, indicating saturation of slags.

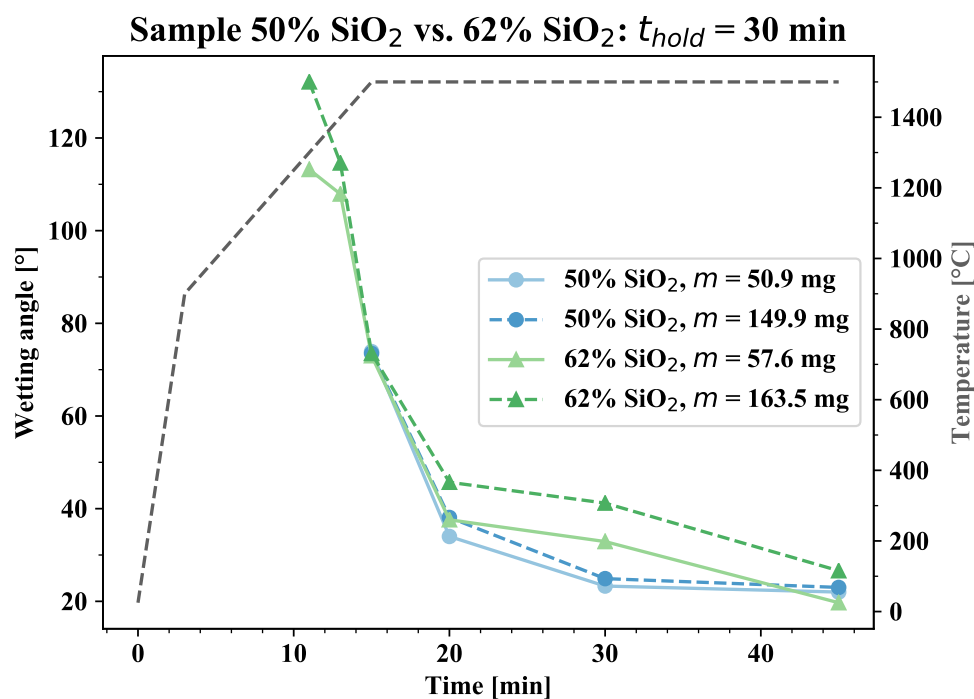


Figure 5.1: Recorded wetting angles of slag samples at 1500 °C with 30 min holding time.

At the end of the holding time, all the parallels had a final wetting angle at around 20°.

This indicates that slags with different silica content may reach similarly good wetting conditions at 1500 °C when held long enough, meaning the interactions between the slag and quartz are considerably strong.

The recorded wetting angles for each experiment were calculated with ImageJ. Some of the slags were quite similar in the wetting angle at different time intervals. Consequently, they showed a large difference in other time intervals, e.g., at 15 min holding time for Sample 62-20-18. The variance in wetting angles may be an uncertainty as calculations in ImageJ indicated a deviation of 5°.

### 5.1.1 The effect of temperature

The wetting angles of the parallels presented in Figure 5.1 are plotted against the same slags tested by Kristiansen (2022) at 1550 °C in Figure 5.2[48]. Here, Sample 38-20-42 wet the substrate at 1550 °C, showing a remarkable wettability once it is liquefied. By comparing the experiments done at 1500 °C against 1550 °C, it is observed a significant difference in wettability at different temperatures. This indicates a greater wettability for slags at 1550 °C compared to 1500 °C, meaning the slags reached even greater wetting conditions at a higher rate when held at 1550 °C. This finding relates to the driving force for wettability in reactive wetting, where wettability is thermodynamically favored at a higher temperature[46].

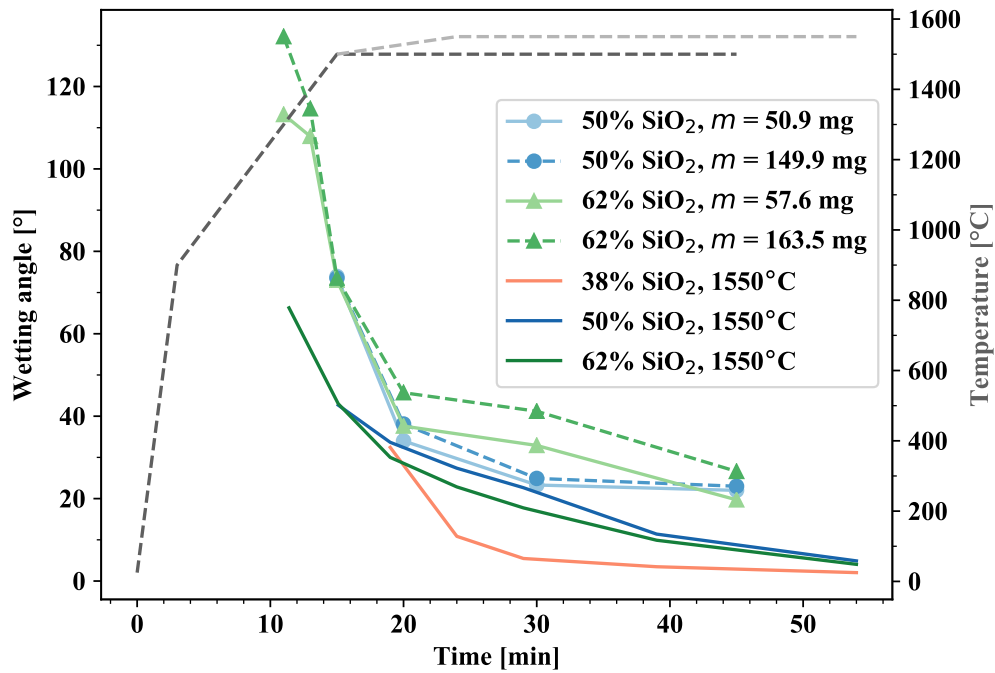


Figure 5.2: Recorded wetting angles of slag samples at 1500 °C and 1550 °C with 30 min holding time. The results at 1550 °C are taken from Kristiansen (2022)[48].

Overall, wetting experiments performed at 1500 °C and 1550 °C correspond well with the results from Seo et al. (2001) and Yoo et al. (2021), where higher experimental temperatures will decrease the wetting angle and a greater wettability for low-silica slag[46, 47]. This reactive system between slag and quartz seems to result in greater wettability with low-silica slag as a result of the driving force toward the equilibrium state. In addition, high-silica slag and a decrease in temperature lead to a higher viscosity[1, 3, 12, 21, 26]. A relation in wetting abilities between the silica content and viscosity may be proposed since they indicate a similar pattern, as a less viscous slag might allow for easier spreading on the surface.

### 5.1.2 The effect of slag size

The wettability of slags was found to be similar between smaller and larger slag samples, questioning if the overall contact area is favoring stronger wettability or not. The surface

area of the quartz substrate and the total contact area between the liquid slag and quartz in each parallel is presented in Table 5.2. Here, it is observed that the contact area was approximately twice as large for large-sized parallels at similar holding times, except for Sample 38-20-42 which did not liquefy. For instance, parallel S50-30 had a contact area of  $0.4778 \text{ cm}^2$  compared to parallel L50-30 with a contact area of  $0.8284 \text{ cm}^2$ . Even though the large-sized parallels had a larger contact area, they did not experience any significantly larger wetting angle, meaning a smaller contact area at the interface may not favor any stronger driving force than a large contact area.

Table 5.2: Contact areas of the different slag samples during wetting experiments, determined from the EPMA images by using ImageJ.

Sample	Figure	Surface area, quartz [ $\text{cm}^2$ ]	Contact area [ $\text{cm}^2$ ]
S38-0	4.11	0.796	0.0363
S38-15	4.12	0.828	0.0423
S38-30	4.13	0.698	0.0585
L38-0	4.14	0.713	0.1795
L38-15	4.15	0.819	0.1716
L38-30	4.16	0.744	0.2316
S50-0	4.17	0.808	0.2011
S50-15	4.18	0.753	0.4049
S50-30	4.19	0.774	0.4778
L50-0	4.20	0.779	0.4083
L50-15	4.21	0.816	0.7605
L50-30	4.22	0.828	0.8284
S62-0	4.23	0.770	0.1901
S62-15	4.24	0.819	0.4255
S62-30	4.25	0.819	0.4657
L62-0	4.26	0.803	0.3739
L62-15	4.27	0.828	0.7466
L62-30	4.28	0.832	0.8316

### 5.1.3 Experimental conditions affecting the wettability

A volume expansion of the substrate was observed for all of the experiments as the quartz undergoes a phase transformation of silica to  $\beta$ -cristobalite through an amorphous phase. As earlier research suggests, quartz can experience a significantly large volume expansion upon heating[28].

Qualitatively, some of the parallels experienced cracking of the substrate. The exact cause behind the cracking is uncertain. However, as the quartz source used in this study was relatively low in impurities, it indicates an expansion induced by the volume expansion causing propagation along the grain boundaries, rather than mineral inclusions around the grain boundaries[37]. Overall, the wettability of the slag will not directly be affected by the volume expansion and cracking, but a roughness on the surface may have been influencing the wetting angle as a result of the expansion[40].

There was not recorded any significant wetting hysteresis for the majority of the samples. In Kristiansen (2022), several samples were experiencing hysteresis as a result of the volume expansion in the quartz substrate[48]. This resulted in differences between the ascending and receding angles. The amount of hysteresis in this study was lower, but some parallels experienced hysteresis, as seen in the wetting images for parallel S50-30 in Figure 4.5. However, the difference between the two angles was not larger than 5°, meaning the difference can be considered to be negligible.

Wetting experiments performed with large-sized slags were found to be covering the whole quartz surface. Thus, it is uncertain if this affected the final wetting angle after 30 min holding time. Further wetting on the quartz may have been hindered as a result of this, meaning the large-sized slags could potentially have a lower wetting angle at the end of the experiment. However, earlier research has suggested that a larger drop volume does not indicate any significant decrease in the wetting angle on surfaces with no hysteresis[58].

## **5.2 SiO<sub>2</sub> in slag droplet**

The apparent change of SiO<sub>2</sub> in the slag droplet was measured for each parallel by using the EPMA. The results showed small variations in silica content, meaning there were no significant changes in SiO<sub>2</sub> when investigating the slag bulk for each slag sample.

The silica content for parallels using slag Sample 38-20-42 is plotted against the distance

from the interface area in Figure 5.3. Here, 0  $\mu\text{m}$  is the interface between the slag and quartz, while positive values indicate the vertical distance from the interface in the slag. They indicate that there is no significant change in the slag bulk, meaning the parallel held for 30 min had a similar silica content as the parallel held for 0 min. In addition, there is no apparent difference between small-sized and large-sized slag samples. A significant increase in  $\text{SiO}_2$  is observed at the interface area due to some liquid phase near the interface, indicating a higher mass transfer in the liquid slag. The silica content near the interface was exceptionally high compared to the slag bulk.

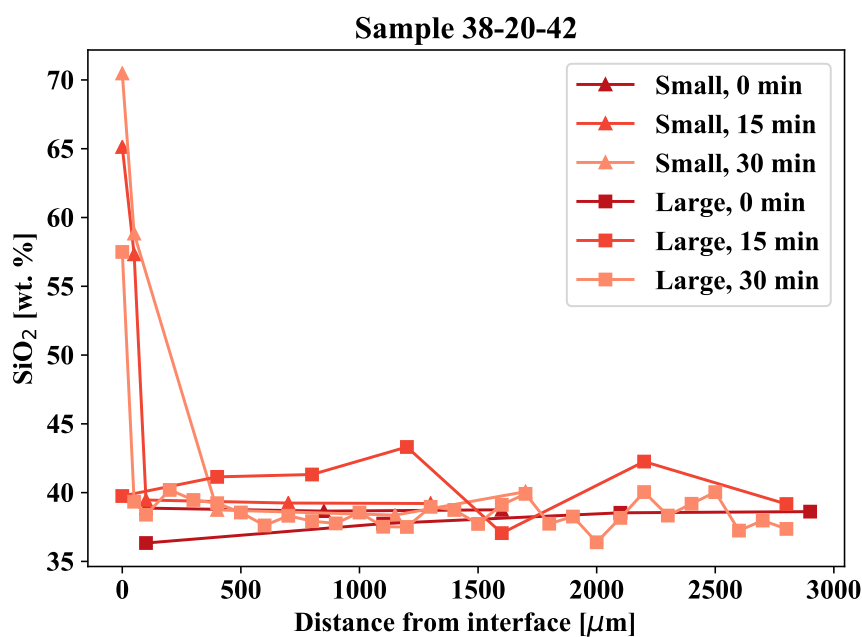


Figure 5.3: Change in the chemical composition of the slag drop on quartz in different parallels with Sample 38-20-42, retrieved from the chemical analysis in EPMA

There were no significant changes in silica content in the bulk across all parallels. The amount of  $\text{SiO}_2$  was close to constant, meaning chemical interactions were not very reactive with solid slag in this reactive system with quartz. Theoretically, a liquid phase should be more reactive than a solid phase as the mobility is higher in a liquid phase.

The change in  $\text{SiO}_2$  for parallels using Sample 50-21-29 is shown in Figure 5.4. Each parallel with 0 min and 15 min holding time experienced similar changes in silica content, i.e., there was no significant trend of an increased amount of silica between small-sized

and large-sized samples. However, there is a notable difference in silica content with 15 min holding time compared to 0 min, where an increase of 5 wt % is seen. This indicates a higher saturation with increasing holding time. The two parallels with 30 min holding time showed an increase in silica content compared to 15 min holding time. In addition, it is observed that the small-sized sample had a higher increase of silica than the large-sized sample.

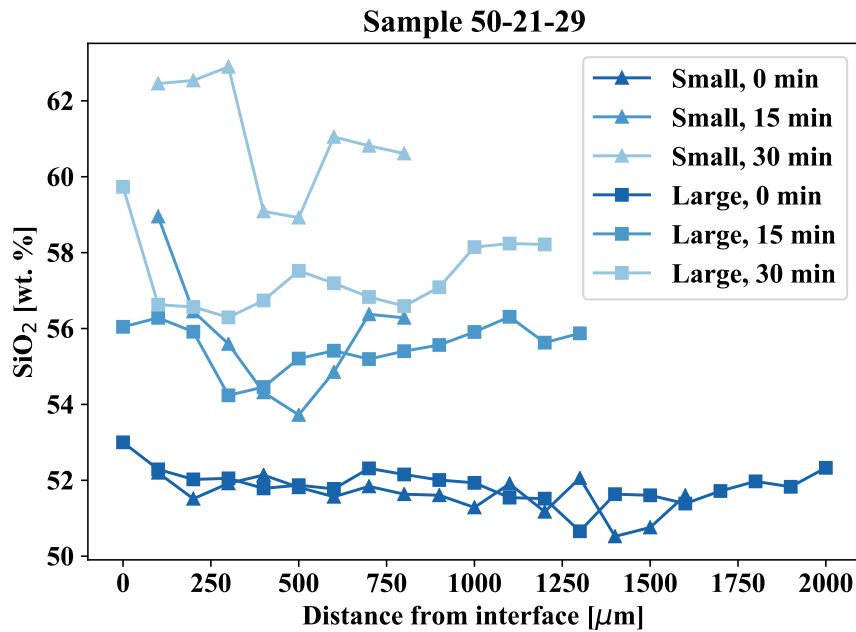


Figure 5.4: Change in the chemical composition of the slag drop on quartz in different parallels with Sample 50-21-29, retrieved from the chemical analysis in EPMA

Figure 5.5 presents the change in  $\text{SiO}_2$  content for parallels using Sample 62-20-18. These parallels followed similar trends with Sample 50-21-29, where a longer holding time increased the silica content, and a higher increase in  $\text{SiO}_2$  was found for the small-sized slag after 30 min. As the small-sized samples will have a smaller amount of slag in contact with the interface area, the saturation is expected to be stronger as there is a smaller amount of slag to be reacted with [3, 50]. Thus, the small-sized samples experiencing a higher increase in silica content can be expected. It is observed that the high-silica slag has a higher silica content, but the composition for parallels with Sample 50-21-29 indicates a greater increase from the master slag composition.

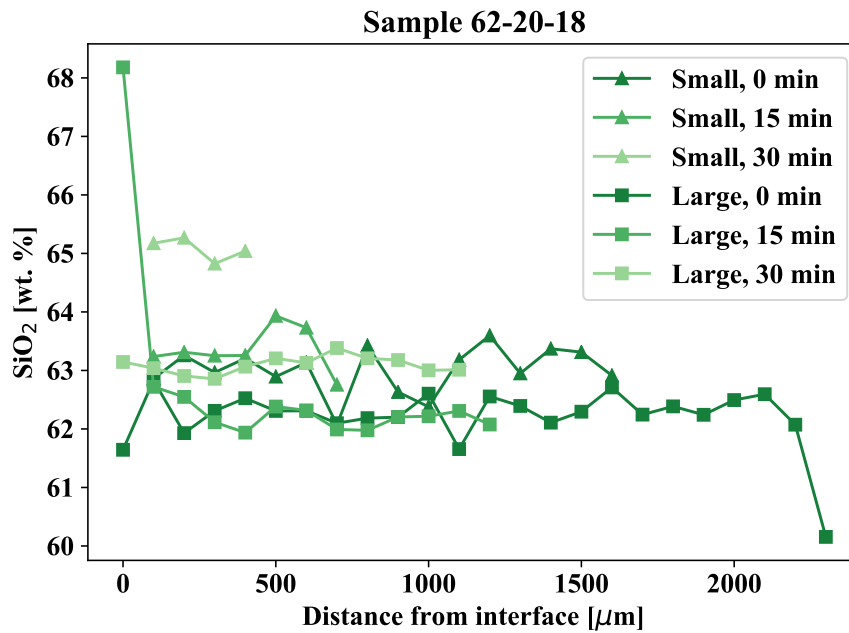


Figure 5.5: Change in the chemical composition of the slag drop on quartz in different parallels with Sample 62-20-18, retrieved from the chemical analysis in EPMA

Compared to Kristiansen (2022)[48], wetting experiments at  $1550\text{ }^{\circ}\text{C}$  showed a greater increase in  $\text{SiO}_2$  by using the same slag samples. A higher saturation is expected for samples at  $1550\text{ }^{\circ}\text{C}$  as the driving force towards the equilibrium state more favored with increasing temperature[10].

During exposure to isothermal heating, parallels with Sample 50-21-29 and 62-20-18 were liquefied, whereas parallels with Sample 38-20-42 were still solid. As mentioned, experiments were operated below the liquidus temperature of this slag, which can be seen in Figure 5.6. Here, the liquidus temperatures for each slag at different silica contents are plotted, showcasing which phases that will exist during the given temperature. As seen, there will be a coexistence of liquid slag and the phase  $\text{CaSi}_2$  at  $1500\text{ }^{\circ}\text{C}$ , which corresponds to the phase  $\text{CaAl}_2\text{Si}_2\text{O}_8$ , explaining why some of the parallels with Sample 38-20-42 had some liquid slag at the interface area. Further, it is seen that the other master slags will be in a liquid phase during the isothermal holding time, as their liquidus temperatures lie below  $1500\text{ }^{\circ}\text{C}$ .

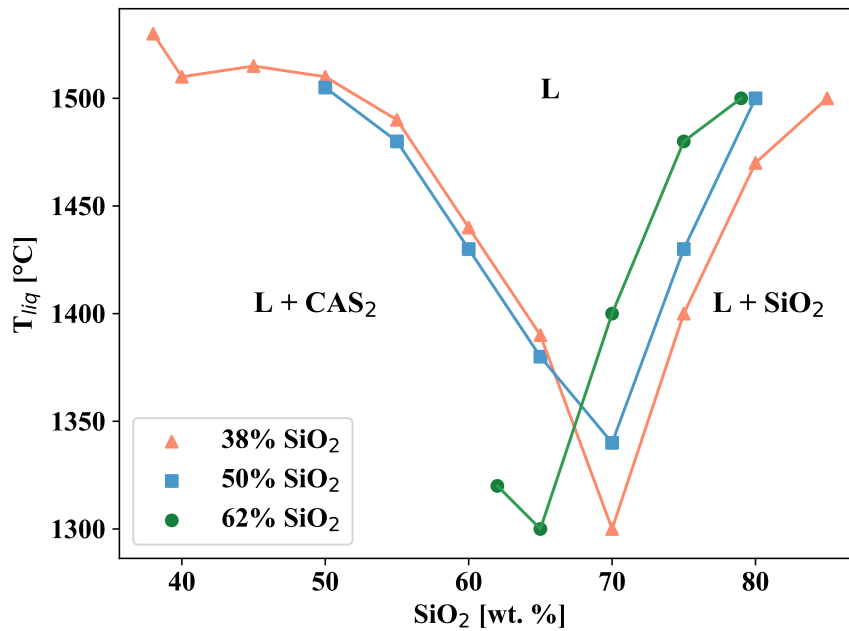


Figure 5.6: Liquidus temperatures at different silica contents for each sample. L = liquid phase and  $\text{CAS}_2 = \text{CaAl}_2\text{Si}_2\text{O}_8$ .

Since all of the samples did not show a significant trend of increasing  $\text{SiO}_2$  further down in the slag droplet, near the interface, it indicates a reaction-controlled mechanism rather than a diffusion-controlled mechanism. In Kristiansen (2022), experiments with Sample 38-20-42 and 50-21-29 were reaction-controlled. However, Sample 62-20-18 showed signs of being diffusion-controlled as an apparent increase in  $\text{SiO}_2$  was found closer to the interface.

### 5.2.1 Internal convection

The mass transfer of the slags may be influenced by convection. In metallurgical processes, Marangoni convection, flow along surface and interface, is often present as interfacial tension is induced by either a temperature gradient or a concentration gradient[59]. The flow in the liquid drop tends to go towards places with a high surface tension[60].

Figure 5.7 shows an illustration of how a Marangoni convection may influence the flow of the liquid slag, where the interfacial tensions at the bottom are lower than at the top of

the droplet. This effect creates a circulation, resulting in an even distributed saturation in the liquid.

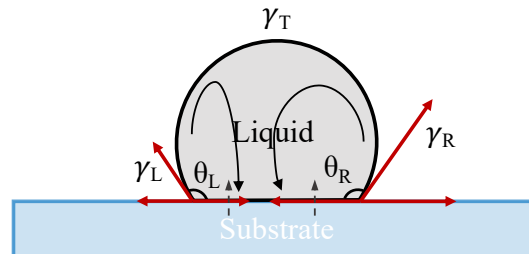


Figure 5.7: Schematic illustration of how the Marangoni convection in a liquid drop can influence the dissolution mechanisms. The arrows in the liquid represent the potential flow of mass.

In molten slags, the effect of Marangoni convection has been recorded in research, as a result of a temperature gradient[61]. It is thus a possibility that the slag samples may have experienced Marangoni convection when considering similar silica contents in the slag bulks were found. Circulation in the slag drops was observed during sessile drop experiments, as particles on the surface were moving around from the bottom to the top of the slag.

### 5.2.2 Basicity

The calculated mean basicity ratio with their respective error bars for each parallel is shown in Figure 5.8. Here, the master slag is the slag basicity before wetting experiments. The basicity ratios were calculated from the chemical analysis in EPMA. The bar plots indicate a small difference in the basicity ratio for each sample when compared to their master slag ratio before wetting experiments. This means that there were no significant changes in the basicity, meaning it is not expected that any major reactions were occurring with alumina during the experiments. Kristiansen (2022) recorded similar results with constant basicity ratios.

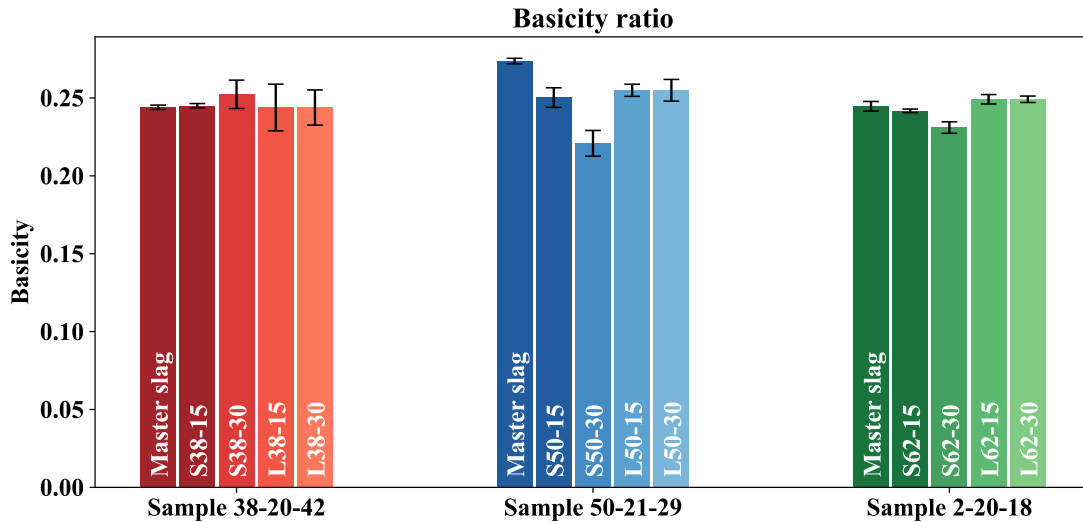


Figure 5.8: Average basicity ratio for each sample with their respective error. The master slag is the basicity ratio before wetting experiments.

The error bars appear to be larger for some samples. Here, the number of analyses done in each parallel varied, as some of them had fewer analyses performed. Generally, the parallels with the broadest error bars had the most analyses performed. Thus, it is expected that the parallels containing more analyses portray a more accurate deviation. Nevertheless, each parallel is quite similar to the master slag basicity.

### 5.3 Modeling of dissolution rate

The change in  $\text{SiO}_2$  presented in Figures 5.3 to 5.5 was used to model the estimated trends in dissolution rate of  $\text{SiO}_2$  for the different slags. The experimental work indicated a reaction-controlled mechanism rather than a diffusion-controlled mechanism as the silica content in slags was found to be similar throughout the liquid drops. This suggests that the dissolution mechanism may be considered to be the limiting factor for the reaction rate.

To model the dissolution rate, Equation (2.13) was implemented as the basis of the mechanism, where the rate constant,  $k$ , silica content at the equilibrium state,  $\% \text{SiO}_2(\text{eq})$ , and the experimental silica content at a given time,  $\% \text{SiO}_2(\text{t})$ , were taken in consideration. The

equation is presented in Equation (5.1). Note that the potential internal convection in the slag was not considered in this model.

$$\Delta\%SiO_2 = \Delta t \cdot k [\%SiO_2(eq) - \%SiO_2(t)] \quad (5.1)$$

As the dissolution mechanisms were reaction-controlled, an average of the experimental silica content was calculated at 0 min and 30 min to base the model on, presented in Table 5.3. The apparent change in silica per minute for each parallel can be found in Appendix A.

Table 5.3: The average silica content in the slag droplet for each modeled sample, at 0 min and 30 min.

Sample	%SiO <sub>2</sub> [wt. %]	
	$t_{hold} = 0$ min	$t_{hold} = 30$ min
S50-30	51.6	61.1
L50-30	51.9	57.4
S62-30	63.0	65.1
L62-30	62.2	63.1

The estimated dissolution rate of SiO<sub>2</sub> for Sample 50-21-29 is shown in Figure 5.9. Here, the parallel run with 50.9 mg (S50-30) slag is presented in dark blue and the parallel with 149.9 mg (L50-30) in light blue, where the average experimental silica content from Table 5.3 is marked with a triangle. The model indicates that the dissolution rate for S50-30 is faster compared to L50-30, which corresponds to the small-sized sample being more saturated with silica after 30 min than the large-sized sample.

The estimated trend for the dissolution of SiO<sub>2</sub> is plotted with dotted lines, illustrating how one would expect the saturation to be after a longer holding time. Both samples are close to the equilibrium state after 7 hours, meaning it would take a considerably long time before complete saturation of 80 wt %.

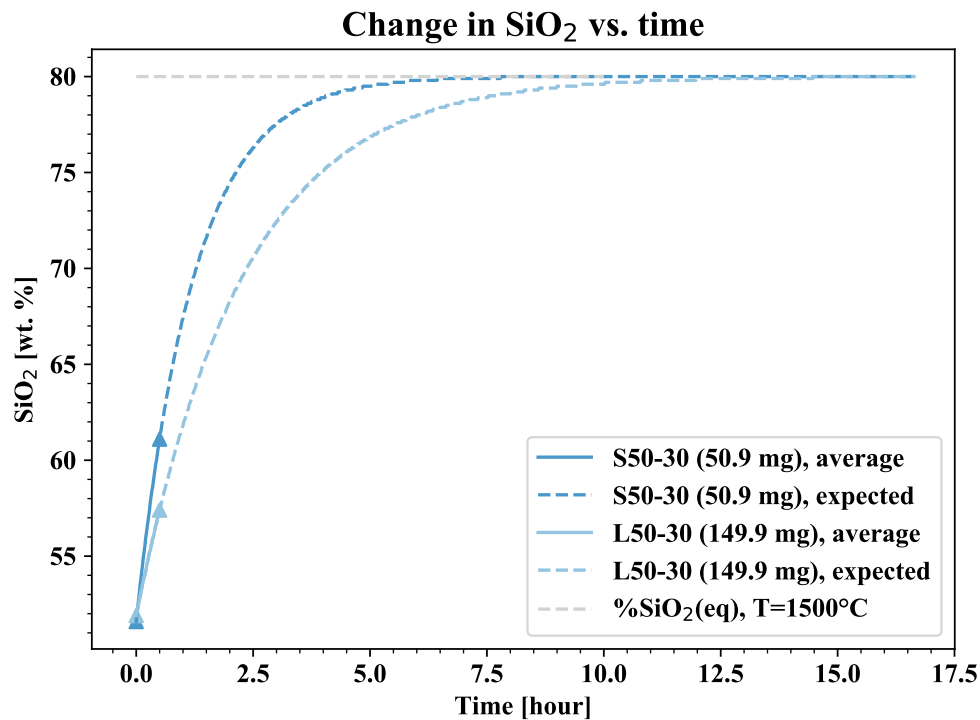


Figure 5.9: Plotted dissolution rate for parallels with Sample 50-21-29. The light blue is the small-sized sample S50-30, the dark blue is the large-sized sample L50-30 and the grey is the silica content at equilibrium state.

Dissolution rates for parallels with Sample 62-20-18 is presented in Figure 5.10, where the parallel with 57.6 mg (S62-30) is shown in dark green and 163.5 mg (L62-30) in light green. Similarly to Sample 50-21-29, the small-sized slag experienced a faster dissolution rate compared to the large-sized slag. However, it is seen that it takes a significantly longer time before they will reach the equilibrium state of 79 wt%. Parallel S62-30 is close to complete saturation after 15 hours, while the parallel L62-30 is still not completely saturated after 25 hours. Thus, the dissolution rate of SiO<sub>2</sub> is expected to be faster for the low-silica slags, indicating a stronger driving force during wetting.

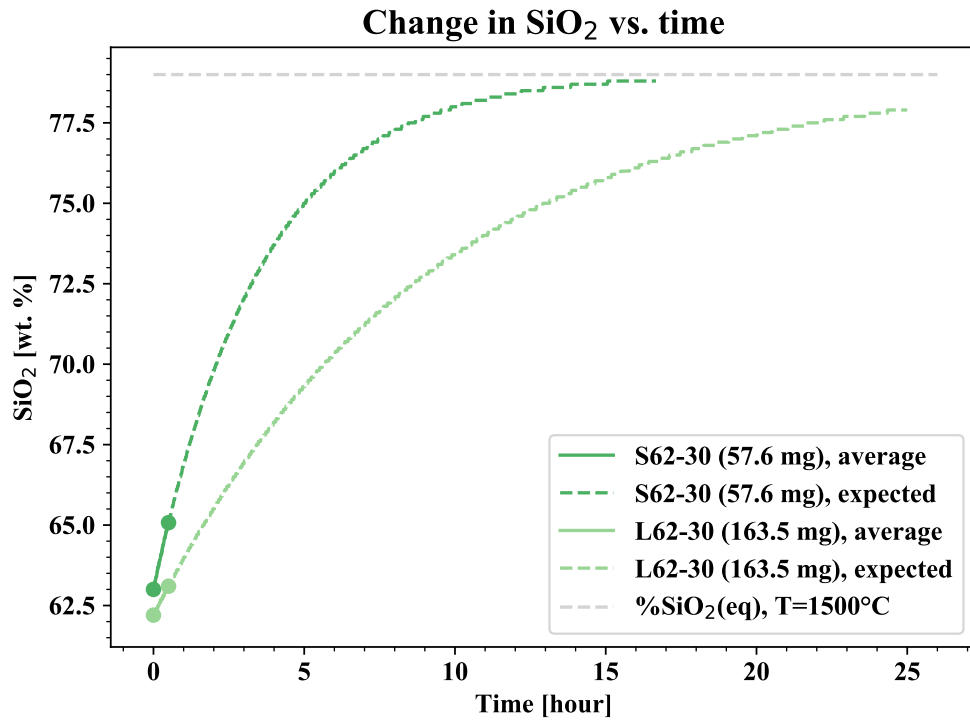


Figure 5.10: Plotted dissolution rate for parallels with Sample 62-20-18. The light green is the small-sized sample S62-30, the dark green is the large-sized sample L62-30 and the grey is the silica content at equilibrium state.

Estimated rate constants from the modeling are tabulated in Table 5.4. Here, the low-silica slags have a higher rate constant than the high-silica slags, proposing a strong driving force towards the equilibrium state for low-silica slags with similar experimental conditions.

Table 5.4: Estimated rate constant,  $k$ , from the modeling in Figures 5.9 and 5.10.

Sample	$k$ [ $\text{g s}^{-1}$ ]
S50-30	$2.25 \cdot 10^{-4}$
L50-30	$1.21 \cdot 10^{-4}$
S62-30	$7.66 \cdot 10^{-5}$
L62-30	$3.06 \cdot 10^{-5}$

### 5.3.1 The effect of temperature

In Figures 5.11 and 5.12, the estimated dissolution rates for Sample 50-21-29 and 62-20-18 are plotted against the dissolution rates estimated at 1550 °C from Kristiansen (2022)[48].

It is observed that the rate portrays a high similarity for Sample 50-21-29 at 1500 °C and 1550 °C. However, the final silica content at 1550 °C appears to be higher due to a higher saturation level at the equilibrium state. Experiments at both temperatures indicate a saturated slag after a long enough holding time.

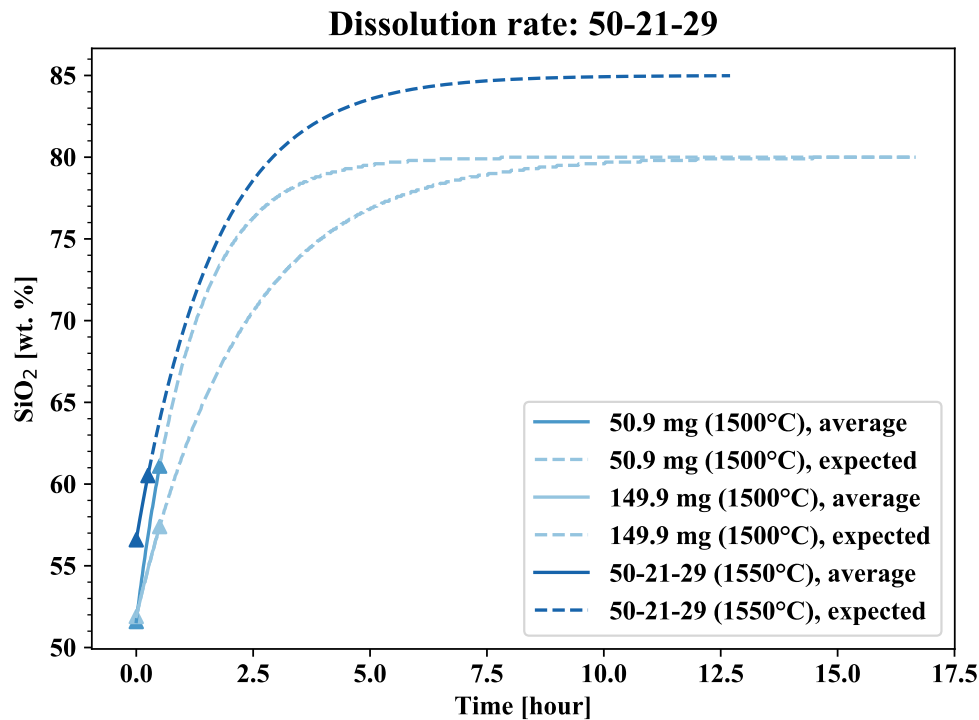


Figure 5.11: Plotted dissolution rate for parallels with Sample 50-21-29 at 1500 °C and 1550 °C. The light blue is the small-sized sample S50-30, the darker blue is the large-sized sample L50-30, the darkest blue is the sample at 1550 °C and the grey is the silica content at equilibrium state.

However, for Sample 62-20-18, the experiments at 1500 °C experience a faster dissolution of SiO<sub>2</sub> compared to experiments at 1550 °C. Note that the model from Kristiansen (2022) indicates a deviation of 5 wt %. It is seen that the silica content is higher at the beginning of isothermal heating for the slag held at 1550 °C, while the amount of SiO<sub>2</sub> is higher after 200 min. These models indicate a reaction-controlled mechanism in the beginning before a diffusion-controlled mechanism dominates after 200 min. Thus, the effect of viscosity may influence the driving forces in this system, as the viscosity of the slag decreases with increasing temperature.

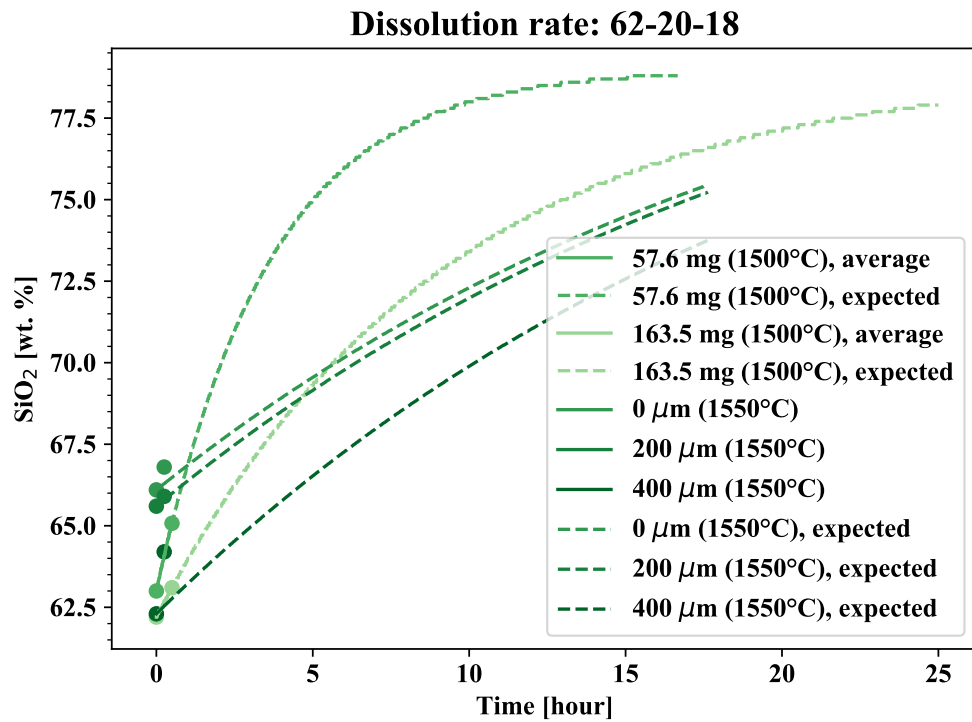


Figure 5.12: Plotted dissolution rate for parallels with Sample 62-20-18 at 1500 °C and 1550 °C. The light green is the small-sized sample S62-30, the darker green is the large-sized sample L62-30, the three darkest greens are the sample at 1550 °C in different positions and the grey is the silica content at equilibrium state.

By using the estimated rate constants for each experiment, a linear trend of the rate constant was estimated with the Arrhenius equation, as seen in Figure 5.13. Here, the inverse temperature,  $1/T$ , is plotted against the logarithm of the rate constant to determine the activation energy,  $E_a$ . An increase in the rate constants was found with increasing temperature for both samples. From the Arrhenius equation in Equation (2.12), it is expected that the rate constant should increase exponentially with increasing temperature.

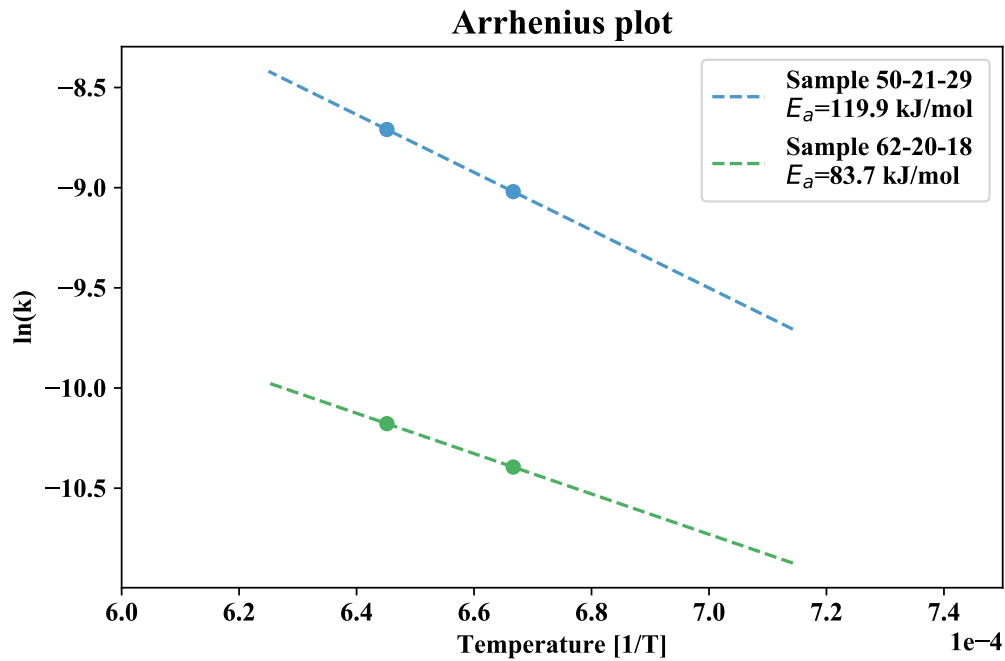


Figure 5.13: Estimated rate constants from an Arrhenius plot. The rate constants are taken from the modeling at 1500 °C and 1550 °C. For Sample 62-20-18, the rate constant estimated by Maroufi et al. (2015) was used at 1550 °C.

The activation energy is presented in Table 5.5 for each sample. This indicates higher activation energy for Sample 62-20-18 compared to Sample 50-21-29. This is contradictory to the results from Maroufi et al. (2015), where the activation energy for the diffusion of silica was lower for the master slag with an addition of 10 wt% CaO, i.e., for a low-silica slag[52]. Theoretically, the activation energy should be higher for a reaction with a lower rate constant[10]. This unexpected trend may be a result of the estimated rates in Figure 5.12.

Table 5.5: The estimated activation energy,  $E_a$ , retrieved from the Arrhenius equation model based on the estimated rate constants from modeling.

Sample	$E_a$ [kJ mol <sup>-1</sup> ]
50-21-29	119.9
62-20-18	83.7

The results on the dissolution rate of SiO<sub>2</sub> correlate with similar research. Maroufi et al. (2015) found that the dissolution rate was increased with decreasing amount of silica

and alumina, and with an increasing amount of calcia[52]. This is further justified by the findings in this study, as Sample 50-21-29, with a lower amount of silica, had a higher dissolution rate than the high-silica slag, Sample 62-20-18, at 1500 °C and 1550 °C. Additionally, the low-silica experiment with Sample 38-20-42 at 1550 °C experienced the highest dissolution rate. Maroufi et al. (2015) did also record a trend of increasing rate concerning an increase in temperature. This was found for Sample 50-21-29. Contradictory, the rate was decreased concerning increasing temperature for Sample 62-20-18, as a result of the model used for the sample at 1550 °C.

Further, Feichtinger et al. (2014)[53] showed an increase in viscosity leading to a decrease in the dissolution rate, which is also indicated in this study. Sample 62-20-18 has a higher viscosity compared to Sample 38-20-42 and 50-21-29 at 1500 °C and 1550 °C, showing that the viscosity of the melt influences the dissolution rates of SiO<sub>2</sub>. In addition, experiments with Sample 62-20-18 indicate that the viscosity of the slag may play a significant role in the dissolution rate.

As the results indicate slower reaction kinetics and smaller changes in SiO<sub>2</sub> at lower temperatures, investigating higher temperatures could potentially benefit the research on this topic. Temperatures below 1500 °C are often recorded at the top of the furnace, suggesting a rather inactive zone around the feeding area[1]. However, the materials will be more reactive at the bottom of the furnace, meaning the interactions between slag and quartz should be investigated above 1600 °C.

## 5.4 Slag in cracks

Some of the samples experienced cracking where liquid slag descended into the substrate. This resulted in an increase in  $\text{SiO}_2$  in the slag present in cracks, which correlates to the results from Kristiansen (2022)[48]. The recorded silica content at different positions in the cracks is presented in Figure 5.14. Here,  $0 \mu\text{m}$  denotes the interface between the slag and the quartz, negative values denote the distance from the interface in the slag droplet and positive values denote the distance from the interface in the crack. It is observed that most of the cracks experienced an increase in  $\text{SiO}_2$  compared to the silica content in their respective slag droplet. Theoretically, it is expected that the slag in the cracks will be more saturated compared to the slag droplet as the tiny volume of slag in the cracks will be saturated while in contact with a larger surface area of quartz[3, 50].

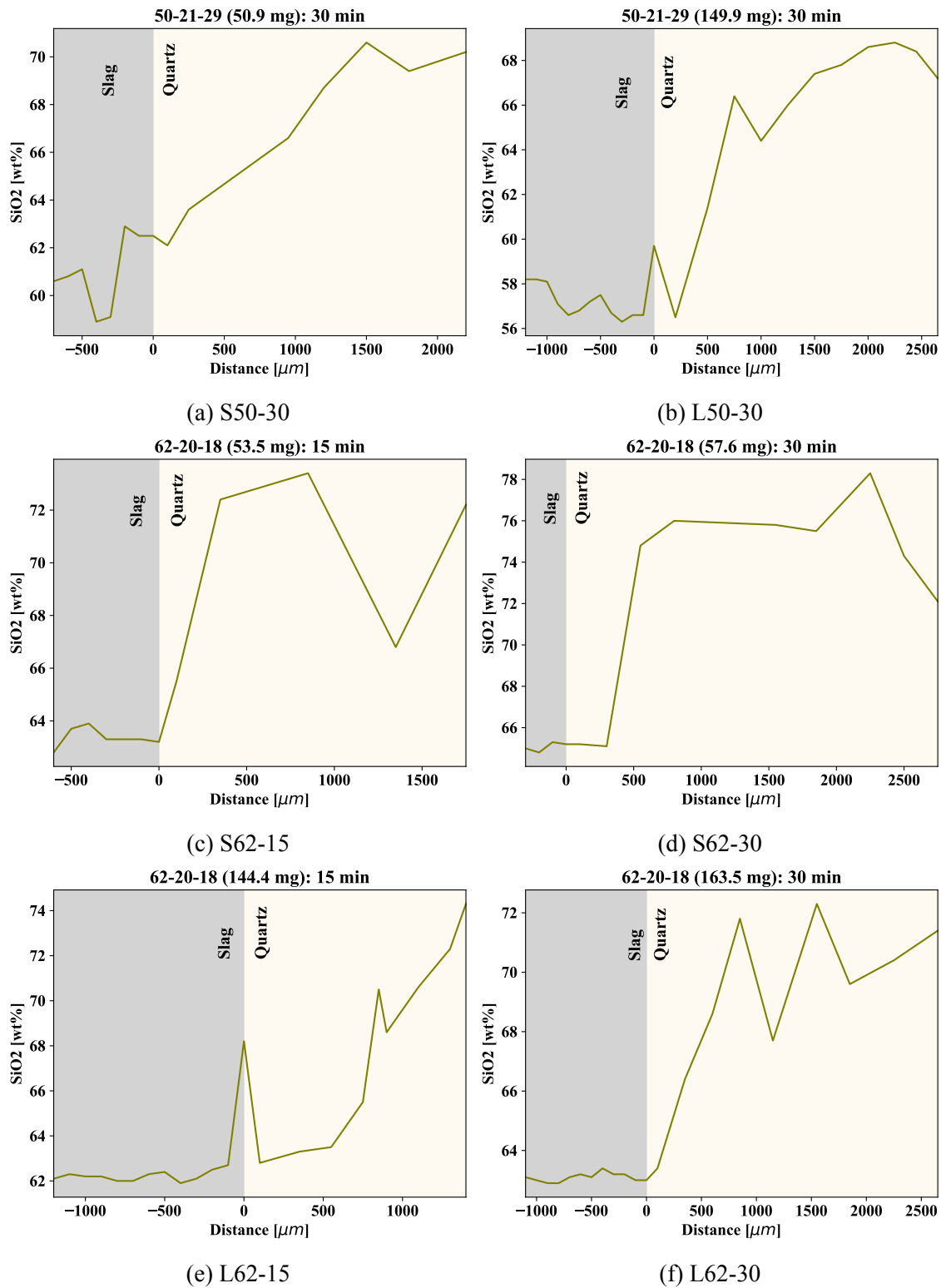


Figure 5.14: Cross-sectional view of the silica content in samples with slag in cracks. 0  $\mu\text{m}$  denotes the interface area between the slag and the quartz.

This can be related to Table 5.6 which presents the overall crack length and the area of slag present in the crack for each sample.

Table 5.6: Contact areas of the slag present in quartz cracks during wetting experiments, determined from the EPMA images by using ImageJ.

Sample	Figure	Contact length [mm]	Total slag in crack [mm <sup>2</sup> ]
S50-30 Crack	4.29b	5.218	0.248
L50-30 Crack	4.30a, 4.30b	7.914	0.541
S62-0 Crack	4.31	10.114	0.757
S62-15 Crack	4.32	3.993	0.082
S62-30 Crack	4.33a, 4.33b	6.005	0.210
L62-15 Crack	4.34	4.839	0.244
L62-30 Crack	4.35a, 4.35b	5.493	0.516

The size of the contact area between the slag and the quartz varied by the cracking of the substrate. More cracking may result in larger cracks, allowing more slag to penetrate them. By comparing the contact area to the total silica content in the slag between parallels with the same slag and holding time, it indicates that less slag in a larger crack may result in higher silica content. The only exception found is between S62-15 and L62-15, where L62-15 had a higher silica content, even though S62-15 had less slag in the crack. This may be caused by the duration of time present in the crack during heating. If the crack propagates later in the experiment, the slag will thus spend a shorter amount of time in the crack to be saturated.

In addition, slag further down in the crack is expected to be the most saturated over time as the slag has been descended in the crack for longer compared to the slag near the interface area. This is seen in most of the parallels. Some of them show a decrease at the end, which can be related to the reliability of the chemical analysis.

The relative trend of the increase in SiO<sub>2</sub> for each crack is further studied in Figure 5.15. A linear fit was estimated for each of the slags in cracks, as the points from the chemical analysis show an indication of a linear trend. Since the number of data points in each plot is considered to be small, they are assumed to follow a normal distribution. A 90% confidence interval and prediction limit were calculated to determine the probability and the predictability of the measured data points.

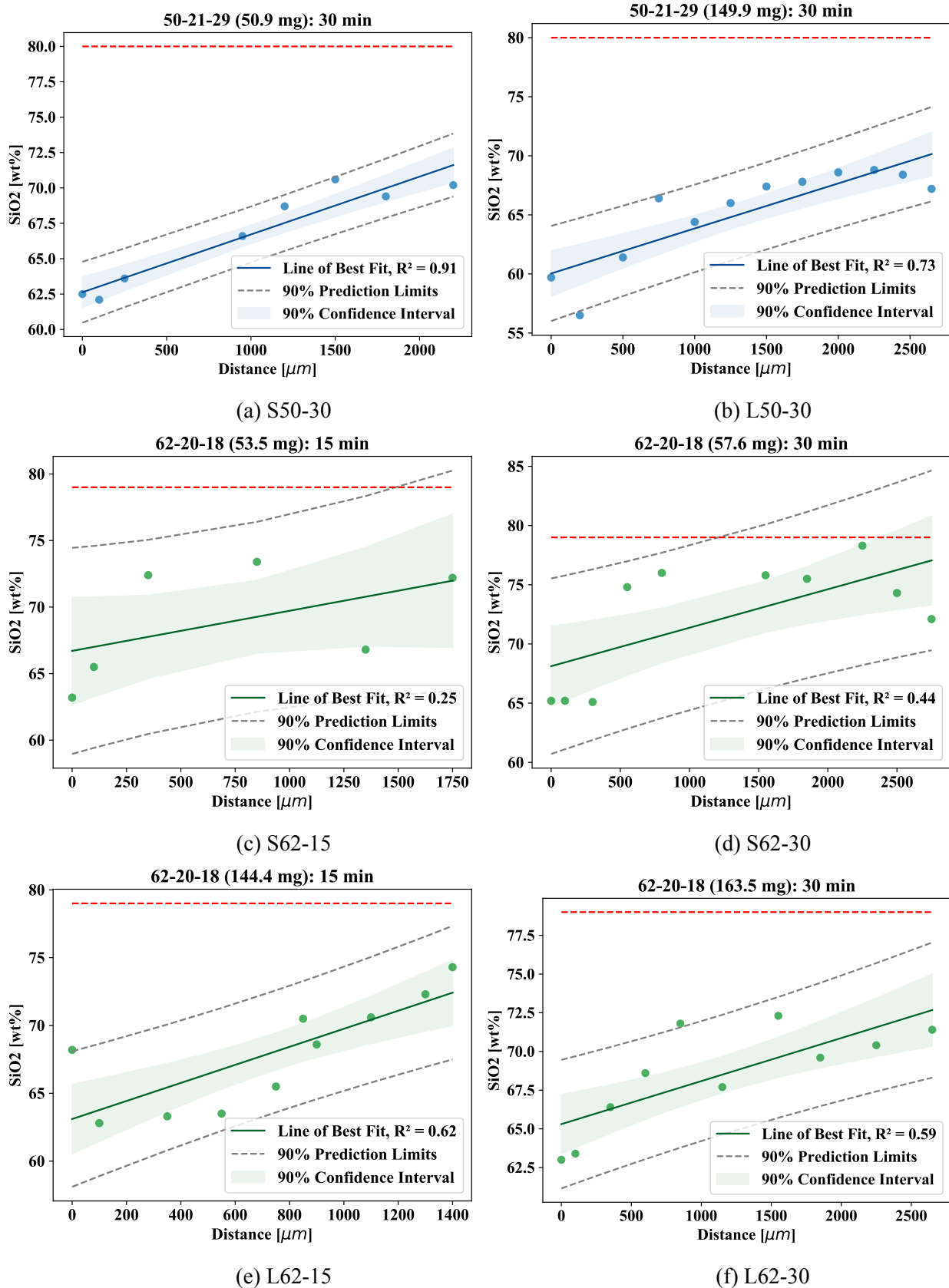


Figure 5.15: Estimated linear fit of the silica content in slag present in cracks. The colored area is the 90% confidence interval and the grey dotted lines are the 90% prediction limits. The red dotted lines represent the silica content at the equilibrium state, 80 wt % for Sample 50-21-29 79 wt % for Sample 62-20-18.

The estimated trends vary in reliability and probability. Here, the parallels S50-30 and L50-30 show a linear fit in the upper limit, where  $0.73 < R^2 < 0.91$ . Parallels L62-15 and L62-30 show a moderate fit of  $R^2 = 0.62$  and  $R^2 = 0.59$ . However, parallel S62-15 and S62-30 indicate a weaker trend with  $R^2 = 0.25$  and  $R^2 = 0.44$ . The prediction limits discover only one outlier in the measured points, but in general, most of the data points lie in between the limits. The poor trend in S62-15 may indicate a fast dissolution in the beginning which declines further down in the crack.

There is only one parallel that indicates it has been almost fully saturated, which was S62-30. At over 2000  $\mu\text{m}$ , it is close to the equilibrium state of 80 wt %, showing a high saturation. Regarding the other parallels, they were yet to be fully saturated.

The trends found in the cracks may be a result of the precision of the chemical analysis. The chemical compositions estimated are not normalized, meaning that the composition may not be at 100%. In addition, the small amount of slag located in the cracks may portray a higher silica content than reality. When analyzed, disturbance from the quartz substrate that lies below the slag in the crack can influence the analysis, resulting in an irrational increase. Thus, wide prediction limits of almost 5 wt. % indicate uncertainty in the chemical analysis. However, the estimated trends show that there is an increase in  $\text{SiO}_2$  in substrate cracks, qualitatively.

# Chapter 6

## Conclusion

Improvements in silicon and ferrosilicon production are needed to improve the well established production process. The build-up of slag in the furnace has proven to address several challenges which can hinder the mass flow of charge materials and may clog the tap holes. Understanding the wettability and reaction kinetics between slag and quartz is crucial for optimizing silicon and ferrosilicon production. By improving the understanding of these interactions, it becomes possible to enhance the mass flow of charge materials, leading to increased production efficiency and reduced energy consumption in industrial furnaces.

Wetting experiments were performed in a sessile drop furnace with different silicon slags on a quartz substrate to investigate the wettability at 1500 °C. Slags with a composition of 38 % SiO<sub>2</sub>–20 % CaO–42 % Al<sub>2</sub>O<sub>3</sub> did not wet the quartz surface at all due to its solid phase, while slags with 50 % SiO<sub>2</sub>–21 % CaO–29 % Al<sub>2</sub>O<sub>3</sub> and 62 % SiO<sub>2</sub>–20 % CaO–18 % Al<sub>2</sub>O<sub>3</sub> reached good wetting conditions after 30 min isothermal holding time. The high-silica slag experienced a slower wetting rate but eventually reached a similar wetting angle to the other slags, showing that the wettability of silicon slag is exceptionally good on industrial quartz. The wetting angle showed no significant change with increasing contact area between the liquid drop and substrate. Comparisons with previous research indicate that the wettability is weaker at 1500 °C compared to higher temperatures. Ad-

ditionally, the observed dependence on silica content and drop volume aligns with the expected trends, further supporting the findings of this study.

By analyzing samples using EPMA, an increase in silica content was observed in the liquefied slags with increasing isothermal holding time and with smaller slag size. However, analyses showed no trend of an increase in  $\text{SiO}_2$  in the slag bulk. Internal convection was suggested as a potential influencing factor of the similar composition in the droplets. Consequently, the solid slag of 38 %  $\text{SiO}_2$ –20 %  $\text{CaO}$ –42 %  $\text{Al}_2\text{O}_3$  showed no significant reactions with the substrate as the compositions were similar to the master slag. Only the liquefied slag near the interface experienced an increase, indicating faster reaction kinetics with the liquid slag.

To estimate the dissolution rate of  $\text{SiO}_2$  in the slags, a model was developed to investigate the change in chemical composition during high-temperature heating. The results indicated a correlation between the driving force for different slags and the dissolution rate. The rate constant was estimated to be  $2.25 \cdot 10^{-4} \text{g s}^{-1}$  and  $1.21 \cdot 10^{-4} \text{g s}^{-1}$  for 50.9 mg and 149.9 mg samples of 50 %  $\text{SiO}_2$ –21 %  $\text{CaO}$ –29 %  $\text{Al}_2\text{O}_3$ . For samples with 62 %  $\text{SiO}_2$ –20 %  $\text{CaO}$ –18 %  $\text{Al}_2\text{O}_3$ , the rate constant was  $7.66 \cdot 10^{-5} \text{g s}^{-1}$  and  $3.06 \cdot 10^{-5} \text{g s}^{-1}$  for 57.6 mg and 163.5 mg, indicating a faster reaction rate for low-silica slags and smaller samples. A correlation with earlier research shows that more basic slags experience faster saturation to the equilibrium state in a reactive system with quartz. In conclusion, the dissolution of  $\text{SiO}_2$  is determined to be driven by the basicity of the slag, isothermal holding time and the interface area of the liquid slag, demonstrating the influence of temperature on the reaction kinetics.

Cracks were propagating in some of the substrates due to a volume expansion of quartz into the  $\beta$ -cristobalite phase, which allowed descended slag to penetrate the cracks. A trend of increase in  $\text{SiO}_2$  was found further down in the cracks, indicating a higher content of silica compared to the slag bulk. However, further investigations should be conducted to evaluate the discovered trends.

## 6.1 Further work

This study has provided valuable insights into the wetting properties and reaction kinetics between silicon slags and quartz. However, further research is encouraged to deepen the understanding in different areas. First, additional investigations on wetting properties and reaction kinetics are recommended, particularly at temperatures closer to the operating and tapping temperatures in industrial furnaces, would offer more insights. Second, exploring new slag compositions with varying basicity ratios and viscosity found in earlier excavations would contribute to a more comprehensive understanding of the system. These directions may contribute to enhancing silicon and ferrosilicon production processes.

# Bibliography

- [1] A. Schei, J. K. Tuset, and H. Tveit. *Production of High Silicon Alloys*. Tapir Forlag, 1998. ISBN: 8251913179.
- [2] M. Tangstad. *Metal Production in Norway*. Akademika Forlag, 2013. ISBN: 9788232102419.
- [3] M. Tangstad, E. Ringdalen, and M. T. Ksiazek. *Silicon for the Chemical and Solar Industry XIII: Five furnaces five different stories*. NTNU, 2016, pp. 33–42.
- [4] M. Tangstad and M. B. Folstad. “SiO<sub>2</sub>-CaO-Al<sub>2</sub>O<sub>3</sub> slags in Si/FeSi furnaces”. In: *Proceedings of the 16th International Ferro-Alloys Congress (INFACON XVI)* (2021). DOI: <http://dx.doi.org/10.2139/ssrn.3922187>.
- [5] G. Tranell et al. “Reaction Zones in a FeSi<sub>75</sub> Furnace – Results from an Industrial Excavation”. In: *INFACON XII 2010, Proceedings of The twelfth international ferroalloys congress. Sustainable Future. Volume I + II* (2010).
- [6] K. F. Jusnes. “Phase transformations and thermal degradation in industrial quartz”. PhD thesis. NTNU, 2020.
- [7] M. Tangstad, M. B. Folstad, and M. T. Ksiazek. *Silicon for the Chemical and Solar Industry XV: Slag in the Tapping Area in a Si Furnace*. NTNU, 2020, pp. 119–127. ISBN: 9788299735797.
- [8] E. H. Myrhaug. “Non-fossil reduction materials in the silicon process - properties and behaviour”. PhD thesis. NTNU, July 2003. ISBN: 8247156199.

- [9] E. H. Myrhaug and H. Tveit. “Material balances of trace elements in the ferrosilicon and silicon processes”. In: *58 th Electric Furnace Conference and 17 th Process Technology Conference*. 2000, pp. 591–604.
- [10] T. Rosenqvist. *Principles of Extractive Metallurgy*. NTNU, 2004. ISBN: 8251919223.
- [11] K. Mills et al. “The Structure and Properties of Silicate Slags”. In: *Treatise on Process Metallurgy* 1 (Nov. 2013), pp. 149–286. DOI: <https://doi.org/10.1016/B978-0-08-096986-2.00008-4>.
- [12] J. Götze and R. Möckel. “Classification, Mineralogy and Industrial Potential for SiO<sub>2</sub> Minerals and Rocks”. In: *Quartz: deposits, mineralogy and analytics, Berlin ; New York* (2012).
- [13] Y. Waseda and J. M. Toguri. *The Structure and Properties of Oxide Melts: Application of Basic Science to Metallurgical Processing*. World Scientific, 1998. ISBN: 9789810233174.
- [14] J. F. Stebbins, I. Farnan, and X. Xue. “The structure and dynamics of alkali silicate liquids: A view from NMR spectroscopy”. In: *Chemical Geology* 96.3 (1992), pp. 371–385. ISSN: 0009-2541. DOI: [https://doi.org/10.1016/0009-2541\(92\)90066-E](https://doi.org/10.1016/0009-2541(92)90066-E).
- [15] P. Kozakevitch. “Viscosité et éléments structuraux des aluminosilicates fondus: laitiers CaO-Al<sub>2</sub>O<sub>3</sub>-SiO<sub>2</sub> entre 1 600 et 2 100° C”. In: *Revue de métallurgie* 57.2 (1960), pp. 149–160.
- [16] T. Saito and Y. Kawai. “On the viscosities of CaO–SiO–Al, O, slags: Tohoku Univ”. In: *Research Inst. Sci. Repts., ser. A* 3 (1951), pp. 491–501.
- [17] E. T. Turkdogan and P. M. Bills. “A critical review of viscosity of CaO-MgO-Al<sub>2</sub>O<sub>3</sub>-SiO<sub>2</sub> melts”. In: *British ceramic bulletin* 39.11 (1960), pp. 682–687.
- [18] H. G. Lee. *Chemical Thermodynamics for Metals and Materials*. Imperial College Press, 1999. ISBN: 9781860941771.

- [19] VDEh. *Slag atlas*. Verlag Stahleisen GmbH, 1981. ISBN: 9783514004573.
- [20] Y. S. Lee et al. “Influence of basicity and FeO content on viscosity of blast furnace type slags containing FeO”. In: *ISIJ international* 44.8 (2004), pp. 1283–1290.
- [21] D. Sifarakas et al. “Measurement of viscosity of SiO<sub>2</sub>-CaO-Al<sub>2</sub>O<sub>3</sub> slag in wide temperature range by aerodynamic levitation and rotating bob methods and sources of systematic error”. In: *International Journal of Microgravity Science and Application* 35.2 (2018), p. 350204.
- [22] L. Řeháčková et al. “Influence of CaO content on viscosity of molten CaO-Al<sub>2</sub>O<sub>3</sub>-SiO<sub>2</sub> system”. In: *Archives of Materials Science* 62 (2013), p. 62.
- [23] T. Werner. “As-tapped Liquid Silicon Temperature Measurements in an Industrial Furnace”. MA thesis. NTNU, 2019.
- [24] Guo-Hua Zhang and Kuo-Chih Chou. “Influence of Al<sub>2</sub>O<sub>3</sub>/SiO<sub>2</sub> ratio on viscosities of CaO-Al<sub>2</sub>O<sub>3</sub>-SiO<sub>2</sub> melt”. In: *ISIJ international* 53.1 (2013), pp. 177–180.
- [25] D. Sifarakas et al. “Viscosity of SiO<sub>2</sub>-CaO-Al<sub>2</sub>O<sub>3</sub> Slag with Low Silica – Influence of CaO/Al<sub>2</sub>O<sub>3</sub>, SiO<sub>2</sub>/Al<sub>2</sub>O<sub>3</sub> Ratio”. In: *ISIJ International* 58.12 (2018), pp. 2180–2185. DOI: <https://doi.org/10.2355/isijinternational>. ISIJINT-2018-381.
- [26] S. Haghdani, M. Tangstad, and K. E. Einarsrud. “An investigation on the relationship between structure and viscosity of silicate slags”. In: *Proceedings of the 16th International Ferro-Alloys Congress (INFACON XVI)*. 2021.
- [27] T. D. H. McGrath, J. F. White, and J. P. Downey. “Experimental determination of density in molten lime silicate slags as a function of temperature and composition”. In: *Mineral Processing and Extractive Metallurgy* 123.3 (2014), pp. 178–183. DOI: <https://doi.org/10.1179/1743285514Y.0000000060>.
- [28] E. Ringdalen and M. Tangstad. “Softening and Melting of SiO<sub>2</sub>, an Important Parameter for Reactions with Quartz in Si Production”. In: *Advances in Molten Slags, Fluxes, and Salts: Proceedings of the 10th International Conference on Molten*

- Slags, Fluxes and Salts 2016*. Ed. by Ramana G. Reddy et al. Cham: Springer International Publishing, 2016, pp. 43–51. ISBN: 978-3-319-48769-4.
- [29] E. Ringdalen. “Changes in Quartz During Heating and the Possible Effects on Si Production”. In: *JOM* 67 (2015), pp. 484–492. DOI: <https://doi.org/10.1007/s11837-014-1149-y>.
- [30] V. Andersen. *Investigation of thermal properties of quartz for the silicon industry under reducing atmosphere*. Master thesis. NTNU. 2009.
- [31] W. Pabst and E. Gregorova. “Elastic Properties of Silica Polymorphs - A Review”. In: *Ceramics - Silikaty* 57 (Sept. 2013), pp. 167–184.
- [32] A. C. D. Chaklader. “Effect of Trace Al<sub>2</sub>O<sub>3</sub> on Transformation of Quartz to Cristobalite”. In: *Journal of the American Ceramic Society* 44.4 (1961), pp. 175–180.
- [33] E. Ringdalen. “Quartz properties in the silicon production”. In: *Silicon for the Chemical and Solar Industry XII* (2014).
- [34] A. C. D. Chaklader and A. L. Roberts. “Transformation of quartz to cristobalite”. In: *Journal of the American Ceramic Society* 44.1 (1961), pp. 35–41.
- [35] P. J. Heaney, C. T. Prewitt, and G. V. Gibbs. “Silica - physical behavior, geochemistry and materials applications”. In: 29 (1994).
- [36] S. J. Stevens, R. J. Hand, and J. H. Sharp. “Polymorphism of silica”. In: *Journal of Materials Science* 32 (1997), pp. 2929–2935.
- [37] E. D. Martello. “Impurity distribution and reduction behaviour of quartz in the production of high purity silicon”. PhD thesis. NTNU, Sept. 2012. ISBN: 978-82-471-3658-4.
- [38] K. Aasly. “Properties and behavior of quartz for the silicon process,” PhD thesis. NTNU, Aug. 2008. ISBN: 978-82-471-1163-5.
- [39] S. Bao. “Filtration of aluminium-experiments, wetting and modelling”. PhD thesis. NTNU, Jan. 2011, 204 s. ISBN: 9788247131756.

- [40] N. Eustathopoulos, M.G. Nicholas, and B. Drevet. *Wettability at high temperatures*. Pergamon, 1999, p. 420. ISBN: 9780198811923.
- [41] R. N. Wenzel. “Resistance of solid surfaces to wetting by water”. In: *Industrial & Engineering Chemistry* 28.8 (1936), pp. 988–994.
- [42] H. J. Butt et al. “Contact angle hysteresis”. In: *Current Opinion in Colloid & Interface Science* 59 (2022), p. 101574. ISSN: 1359-0294. DOI: <https://doi.org/10.1016/j.cocis.2022.101574>.
- [43] S. Cham. “Investigating factors that Influence carbon dissolution from coke into molten Iron”. PhD thesis. School of Materials Science and Engineering, The university of new south wales, Australia, 2007.
- [44] M. Dekker. “Wettability (Surfactant Science Series)”. In: *New York, TD Blake* (1993).
- [45] K. Landry and N. Eustathopoulos. “Dynamics of wetting in reactive metal/ceramic systems: linear spreading”. In: *Acta Materialia* 44.10 (1996), pp. 3923–3932. ISSN: 1359-6454. DOI: [https://doi.org/10.1016/S1359-6454\(96\)00052-3](https://doi.org/10.1016/S1359-6454(96)00052-3).
- [46] S. M. Seo, D. S. Kim, and Y. H. Paik. “Wetting characteristics of CaO- SiO<sub>2</sub>- Al<sub>2</sub>O<sub>3</sub> ternary slag on refractory oxides, Al<sub>2</sub>O<sub>3</sub>, SiO<sub>2</sub> and TiO<sub>2</sub>”. In: *Metals and Materials International* 7.5 (2001), pp. 479–483.
- [47] C. Yoo, J. Myung, and Y. Chung. “Wetting and Spreading Kinetics between Liquid CaO–SiO<sub>2</sub> Slags and a Solid SiO<sub>2</sub>”. In: *ISIJ International* 61.12 (2021), pp. 2923–2928.
- [48] S. Kristiansen. *Dissolution rate and wettability of SiO<sub>2</sub> –CaO–Al<sub>2</sub>O<sub>3</sub> slag on quartz*. Specialization project. NTNU. 2022.
- [49] M. Tangstad et al. “Slag Properties in the Primary Production Process of Mn-Ferroalloys”. In: *Metallurgical and Materials Transactions B* 52.6 (2021), pp. 3688–3707.

- [50] J. Y. Choi, H. G. Lee, and J. S. Kim. “Dissolution rate of Al<sub>2</sub>O<sub>3</sub> into molten CaO-SiO<sub>2</sub>-Al<sub>2</sub>O<sub>3</sub> slags”. In: *ISIJ international* 42.8 (2002), pp. 852–860.
- [51] A. Kvithyld, G. K. Sigworth, and T. A. Engh. *Principles of Metal Refining and Recycling*. Oxford University Press, 2021. ISBN: 9780198811923.
- [52] S. Maroufi et al. “Dissolution Rate and Diffusivity of Silica in SiMn Slag”. In: *Metallurgical and Materials Transactions B-process and Materials Processing Science* 46.1 (Feb. 2015), pp. 101–108. ISSN: 1073-5615. DOI: <https://doi.org/10.1007/s11663-014-0215-8>.
- [53] S. Feichtinger et al. “In Situ Observation of the Dissolution of SiO<sub>2</sub> Particles in CaO–Al<sub>2</sub>O<sub>3</sub>–SiO<sub>2</sub> Slags and Mathematical Analysis of its Dissolution Pattern”. In: *Journal of the American Ceramic Society* 97.1 (2014), pp. 316–325. DOI: <https://doi.org/10.1111/jace.12665>.
- [54] C. Sindland and M. Tangstad. “Production rate of SiO gas from industrial quartz and silicon”. In: *Metallurgical and Materials Transactions B* 52.3 (2021), pp. 1755–1771.
- [55] S. Bao et al. “Investigation of Two Immiscible Liquids Wetting at Elevated Temperature: Interaction Between Liquid FeMn Alloy and Liquid Slag”. In: *Metall Mater Trans B* 52 (2021), pp. 2847–2858. DOI: <https://doi.org/10.1007/s11663-021-02222-6>.
- [56] *JEOL JXA-8500F Electron Probe Micro analyzer (EPMA)*. JEOL AB. 2009. URL: <https://www.material.ntnu.no/lab/material/equipment/ProdInfoEPMA.pdf>.
- [57] J. Hjelen. *Skanning elektron-mikroskopi*. Nasjonalbiblioteket, 1989.
- [58] J. Drelich. “The Effect of Drop (Bubble) Size on Contact Angle at Solid Surfaces”. In: *The Journal of Adhesion* 63.1-3 (1997), pp. 31–51. DOI: <https://doi.org/10.1080/00218469708015212>.

- [59] T. Matsushita et al. “Interfacial phenomena between molten iron and molten slag—Effect of nitrogen on the Marangoni convection”. In: *Journal of Materials Science* 56 (2021), pp. 7811–7822.
- [60] A. L. Ljung and T. S. Lundström. “Evaporation of a sessile water droplet subjected to forced convection in humid environment”. In: *Drying Technology* 37.1 (2019), pp. 129–138. DOI: <https://doi.org/10.1080/07373937.2018.1441866>.
- [61] K. Mukai. “Wetting and Marangoni effect in iron and steelmaking processes”. In: *ISIJ international* 32.1 (1992), pp. 19–25.

# **Appendix A**

## **Modeling of dissolution rate**

Table A.1: The estimated change in SiO<sub>2</sub> for S50-30 after 30 min, used in the modeling of dissolution rate.

Time [min]	SiO <sub>2</sub> (eq) [%]	ΔSiO <sub>2</sub> (avg) [%]	SiO <sub>2</sub> (avg) [%]
0		-	<b>51.6</b>
1		0.3832	52.0
2		0.3780	52.4
3		0.3729	52.7
4		0.3679	53.1
5		0.3629	53.5
6		0.3580	53.8
7		0.3532	54.2
8		0.3484	54.5
9		0.3437	54.9
10		0.3391	55.2
11		0.3345	55.5
12		0.3300	55.9
13		0.3255	56.2
14	80	0.3212	56.5
15		0.3186	56.8
16		0.3125	57.1
17		0.3083	57.4
18		0.3042	57.8
19		0.3001	58.1
20		0.2960	58.4
21		0.2920	58.6
22		0.2881	58.9
23		0.2842	59.2
24		0.2804	59.5
25		0.2766	59.8
26		0.2729	60.0
27		0.2692	60.3
28		0.2655	60.6
29		0.2620	60.8
30		0.2584	61.1
			<b>61.1</b>
			$R^2 = 0.9971$

Table A.2: The estimated change in SiO<sub>2</sub> for L50-30 after 30 min, used in the modeling of dissolution rate.

Time [min]	SiO <sub>2</sub> (eq) [%]	ΔSiO <sub>2</sub> (avg) [%]	SiO <sub>2</sub> (avg) [%]
0		-	<b>51.9</b>
1		0.2042	52.1
2		0.2028	52.3
3		0.2013	52.5
4		0.1998	52.7
5		0.1984	52.9
6		0.1969	53.1
7		0.1955	53.3
8		0.1941	53.5
9		0.1927	53.7
10		0.1913	53.9
11		0.1899	54.0
12		0.1885	54.2
13		0.1871	54.4
14	80	0.1858	54.6
15		0.1844	54.8
16		0.1831	55.0
17		0.1818	55.2
18		0.1804	55.3
19		0.1791	55.5
20		0.1778	55.7
21		0.1650	55.9
22		0.1753	56.0
23		0.1740	56.2
24		0.1727	56.4
25		0.1715	56.6
26		0.1702	56.7
27		0.1690	56.9
28		0.1678	57.1
29		0.1665	57.2
30		0.1653	57.4
			<b>57.4</b>
			$R^2 = 0.9992$

Table A.3: The estimated change in SiO<sub>2</sub> for S62-30 after 30 min, used in the modeling of dissolution rate.

Time [min]	SiO <sub>2</sub> (eq) [%]	ΔSiO <sub>2</sub> (avg) [%]	SiO <sub>2</sub> (avg) [%]
0		-	<b>63.0</b>
1		0.0734	63.1
2		0.0731	63.2
3		0.0728	63.2
4		0.0724	63.3
5		0.0721	63.4
6		0.0718	63.4
7		0.0714	63.5
8		0.0711	63.6
9		0.0708	63.7
10		0.0705	63.7
11		0.0701	63.8
12		0.0698	63.9
13		0.0695	63.9
14	79	0.0692	64.0
15		0.0689	64.1
16		0.0689	64.1
17		0.0685	64.2
18		0.0679	64.3
19		0.0676	64.4
20		0.0673	64.4
21		0.0670	64.5
22		0.0667	64.6
23		0.0664	64.6
24		0.0661	64.7
25	0.0658	64.8	
26	0.0655	64.8	
27	0.0652	64.9	
28	0.0649	64.9	
29	0.0646	65.0	
30	0.0643	65.1	
			<b>65.1</b>
			$R^2 = 0.9971$

Table A.4: The estimated change in SiO<sub>2</sub> for L62-30 after 30 min, used in the modeling of dissolution rate.

Time [min]	SiO <sub>2</sub> (eq) [%]	ΔSiO <sub>2</sub> (avg) [%]	SiO <sub>2</sub> (avg) [%]
0		-	<b>62.2</b>
1		0.0308	62.2
2		0.0308	62.3
3		0.0307	62.3
4		0.0307	62.3
5		0.0306	62.4
6		0.0305	62.4
7		0.0305	62.4
8		0.0304	62.4
9		0.0304	62.5
10		0.0303	62.5
11		0.0303	62.5
12		0.0302	62.6
13		0.0301	62.6
14	79	0.0301	62.6
15		0.0300	62.7
16		0.0300	62.7
17		0.0299	62.7
18		0.0299	62.7
19		0.0298	62.8
20		0.0298	62.8
21		0.0297	62.8
22		0.0297	62.9
23		0.0296	62.9
24		0.0295	62.9
25		0.0295	63.0
26		0.0294	63.0
27		0.0294	63.0
28		0.0293	63.0
29		0.0293	63.1
30		0.0292	63.1
			<b>63.1</b>
			$R^2 = 0.9971$

